Tesis Doctoral

Estudio del Transporte y Absorción de Luz en Redes Periódicas de Puntos Cuánticos de Semiconductor

Autor:

Erik Sebastian Skibinsky Gitlin

Director:

Francisco Manuel Gómez Campos

Programa de Doctorado en Física y Ciencias del Espacio

Dept. Electrónica y Tecnología de Computadores

Universidad de Granada

2021

A Thesis for the Degree of Doctor of philosophy

A Study on the Transport and Light Absortion on Quantum Dot Periodical Lattices

Author:

Erik Sebastian Skibinsky Gitlin

Supervisors:

Francisco Manuel Gómez Campos

Doctorate program on Physics and Space Science

Dept. Electrónica y Tecnología de Computadores

University of Granada

2021

Editor: Universidad de Granada. Tesis Doctorales
Autor: Erik Sebastian Skibinsky Gitlin
ISBN: 978-84-1306-848-0
URI: http://hdl.handle.net/10481/68189

The research was partially supported within the framework of a scholarship supported financially by Ministerio de Educación y Ciencia under research Grant *Garantía juvenil enero 2018* and ENE2016_80944_R funded by the Spanish Ministerio de Economia, Industria y Competitividad.

Acknowledgements

This thesis has been possible thanks to the support of the University of Granada, its doctoral school, and the Physics and Space Science doctoral programme.

At a personal level I would like to thank my research team who had patiently shown me the way of science. Specially I would like to thank doctor Francisco Manuel Gómez Campos and professor Salvador Rodríguez Bolívar, not only for the formal education that they have provided but more importantly, for all the other things that I had to learn in order to consider myself a freethinking, man of science.

I am also very grateful to my family who had supported me during all this not always rosy road that leads to the conclusion of this thesis. And lastly, I would like to mention María Bauzà, a high school teacher who asked me a simple question that tipped the balance of my immature decision making which eventually drove me into depositing a doctoral thesis.

Abstract

In this work we present a study on the features of electron transport and photon absorption in quantum dot arrays. We developed theoretical models and implemented a simulator to assess the viability of semiconductor colloidal quantum dot arrays as solar cell active components. To this end, we have focused our study on the calculation of the miniband structure, carrier mobility and photon absorption coefficient.

In this thesis we investigated carrier transport in quantum dot superlattices, a kind of highly ordered systems. Transport in these systems have been widely studied using hopping models. These approaches seem to be adequate for disordered and diluted systems, where quantum dot eigenstates overlap weakly and with no periodicity with other neighboring quantum dot. As the state of the art continues to advance towards higher quality, better ordered quantum dot arrays, experimental results report data evidencing band-like transport features. In this thesis we propose a novel picture helping to understand carrier transport in these systems, combining impurity scattering effects with the carrier ensemble thermalization through phonon scattering contribution.

Regarding photon absorption, we mainly focused on studying the influence of quantum dot material, size and interdot distance in the absorption in two-dimensional arrays. We carried out a deep analysis on the influence of light polarization, Fermi level position and temperature in the system. We developed this study with the aim of proposing several strategies focused on finding applications on intermediate band solar cells. Finally a set of unpublished results are presented

on this topic for finite systems.

Resumen

En este trabajo se presenta un estudio de las propiedades del transporte electrónico y la absorción de fotones en redes de puntos cuánticos. Hemos desarrollado modelos teóricos e implementado un simulador para evaluar la viabilidad de puntos cuánticos de semicondictor como componentes para células solares. Para ello, se ha enfocado este estudio en el cálculo de las propiedades de la estructura de minibandas, movilidad electrónica y coeficiente de absorción de fotones.

En esta tesis se ha investigado el transporte de electrones en superredes de puntos cuánticos, un tipo de sistemas altamente ordenados. El transporte en este tipo de sistemas ha sido estudiado comúnmente mediante modelos de *hopping*. Estos modelos han demostrado su eficacia en sistemas desordenados y disoluciones, en los cuales los autoestados cuánticos tienen un solapamiento débil y en los cuales no hay periodicidad. A medida que la tecnología progresa, cada vez se fabrican dispositivos de mayor calidad, en los cuales los puntos cuánticos están más ordenados. En estos dispositivos los datos experimentales evidencian un mecanismo de transporte de electrones con características propias de la conducción a través de bandas de energía. En esta tesis proponemos un nuevo modelo para ayudar a entender el transporte en estos sistemas en el cual se combina la dispersión de electrones por la presencia de impurezas con la termalización mediante dispersión electrón-fonón.

En cuanto a absorción de fotones, nos hemos centrado en el estudio de la dependencia de la absorción con el material del que está compuesto el punto

cuántico, su tamaño, y la distancia entre puntos cuánticos en redes bidimensionales. Hemos llevado a cabo un análisis en profundidad sobre la dependencia de la absorción con la dirección de polarización de la luz, temperatura y nivel de Fermi. Este estudio se ha desarrollado con el objetivo de proponer estrategias focalizadas en encontrar aplicaciones para células solares de banda intermedia. Por último, se presentarán resultados aún no publicados sobre este tema en redes de dimensiones finitas.

Contents

1

Introduction and background

1.1. Motivation

Solar cells are an emerging technology in our hyper industrialized society whose high dependency on non-renewable energy sources has driven our species to a point in which decisive action has to be taken in order to avoid an ecological disaster with no return. To that end, this thesis is a comprehensive investigation of one of the many solar cell technologies under the spotlight, quantum dot solar cells. Quantum dots are one of the technologies that has risen the fastest in terms of energy conversion in the last years[1].

In this research we propose the use of colloidal quantum dots, a form of quantum dots (QDs) that exhibit low size dispersion and good passivation[2–4]. There are already several proposals of QDs as an active element in solar cells which will be discussed later. In the case of this work it is proposed that with the ever improving device fabrication quality, QDs can be arranged in a periodical fashion, used to create a periodic lattice of quantum dots, in which we can adapt the formalism and principles used in atomic crystals to understand the dynamics of these types of systems.

The final goal of this work is to serve as a toolkit or guide to orient the experimental work on colloidal quantum dots for optoelectronic applications, easing the process of selection of the various properties of the desired device, such as QD size, composition, operation temperature, etc.

1.2. Objectives and methodology

The aim of this work is to understand the underlying dynamics of electronic carriers in QD periodic arrangements, proposing two models. One to describe electrons under an external electric field and another one to describe light interaction (photon absorption). To this end, there are two physical quantities we have been able to calculate and compare to real data: electronic mobility and photon absorption. These two quantities are essential to any solar cell operation,

and are linked to other properties such as diffusion length and carrier lifetime.

During this work we used the following steps to obtain our results:

- An atomistic approach, the semiempirical pseudopotential, is used to model the isolated quantum dot, obtaining its eigenstates and calculating the potential energy.
- The tight binding model is used to calculate the electronic structure for periodic and finite QD ensembles.
- For the mobility calculations, we proposed a model based on the Markov chain, significantly reducing computational time in simulations compared to other computational approaches like, for example, Monte Carlo-based calculations
- Lastly, for the absorption calculations we used the semiclassical approximation to calculate the electron-photon interaction.

In all steps of the calculations we have done a thorough exploration of the different variables that have an effect on the final device, namely QD chemical composition, morphology, stoichiometry, and QD size; and for the device configuration, such as periodical lattice constant, temperature and Fermi level. We have programmed a simulator to perform the calculations and compared them to real data whenever available.

1.3. Overview

Quantum dots are structures whose dimensions are in the nanometer range. As usual with this kind of systems, its dynamics are heavily affected by quantum effects. In these systems, quantum confinement leads to a discrete energy spectrum (in contrast with other nanoscopic systems such as quantum wires or wells, or even bulk crystals). This discrete spectrum could inspire someone to treat them as artificial atoms[5–7].

Electronic properties depend importantly upon QD size. This is a key feature of QDs. Quantities such as band gap can be tuned by changing the QD size for a given material, and new quantum effects arise that are not observed in bulk form (e.g. multiexcitonic effects[8] or indirect to direct band gap variations[9]). Because of this, materials that are not interesting for optoelectronic applications in their bulk form can be revisited for these purposes when synthesized in QD form.

This poses the QD as a very promising field of research in material physics [10–13]. Quantum dots present multiple potential uses, ranging from biomedical approaches using their particular photoluminescense and biocompatibility [14–19], new computing paradigms as quantum computing [20–22], lasers [13, 23–25], and, the focus of this research, solar cells [26–33]

QD solar cell is one of the solar technologies whose efficiency has advanced the quickest in recent years[1], achieving a 16.6 % efficiency[34]. We have developed a simulator to calculate the band structure, electron mobility and photon absorption coefficient to be able to assess the viability of QD candidates for this technology.

On the QD synthesis level, there are mainly two approaches: top-down and bottom-up[14]. This research accounts only for colloidal quantum dots, which are a subcategory inside the bottom-up fabrication process. Colloidal quantum dots are easily mass-synthesised while being possible to achieve a low size dispersion and good passivation [2–4] i.e. the quantum dots have less probability of having surface dangling bonds producing electron traps which would hinder electron transport and device regularity[35, 36].

1.4. Quantum Dot Physics

The quantum dot has unique properties that are not only dependent on its chemical species, but also on its size. This can be roughly explained by the

"particle in a box" model. When the box is big enough the energy spectrum can be assumed to be continuum. In the opposite case, when the box is sufficiently small, we have discrete energy levels, and the position of these is heavily dependent on the box dimensions. This simplified picture is the schema behind the QDs radius-dependent properties.

The wave vector **k** labels each eigenstate in the "particle in a box" picture (no spin is considered). The allowed wave vectors are determined by the box size, and the eigenergies can be computed from the following relation.

$$E_{\mathbf{k}} = \frac{\hbar^2}{2m}\left(k_x^2 + k_y^2 + k_z^2\right) \tag{1.1}$$

$$k_i = \frac{n_i \pi}{L} \tag{1.2}$$

where m is in this case the rest electron mass, L_x, L_y, L_z are the edge lengths of the box and n_i is a natural number to calculate **k** along the *i-th* direction. As we can see, the lower the size along a particular direction, the more sparse the energy levels are. This means that on any transition between eigenstates, the electron energy changes a greater amount. As equation 1.1 shows, the energy level separation grows as the size decreases. Thus when dealing with quantum dots, little size differences have great impact on their properties such as luminescence[14].

This can be seen in the density of states (DOS), which represents how many quantum states per unit energy and volume the electron may occupy in a crystal as a function of energy. As shown in figure 1.1, assuming a parabolic band (the same as the "particle in a box") this density behaves very distinctly depending on the system's dimensions. It can be observed that when the system is 3D i.e. all dimensions are in the macroscopic scale, the DOS is proportional to the square root of energy. When the system is 2D i.e. there is one dimension in the nanoscopic scale, the density behaves like a step function. When the system is 1D the density is a set of inverse square roots of energy and when the system is

0D i.e. all dimensions in the nanoscopic scale, the density of states becomes a Dirac delta sequence.

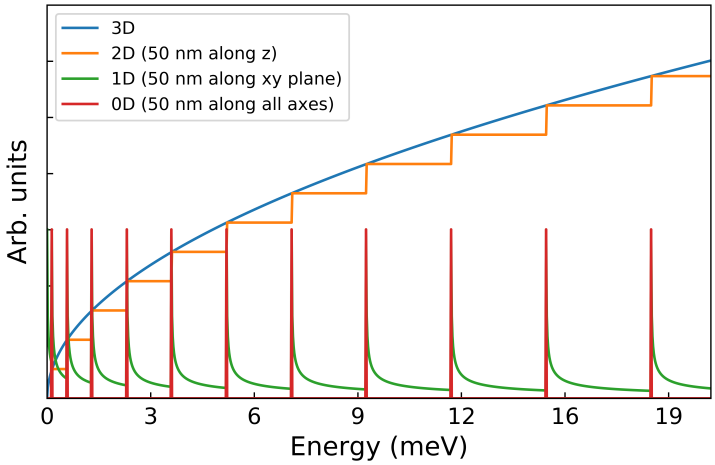

Figure 1.1: Density of States (DOS) for different number of dimensions .

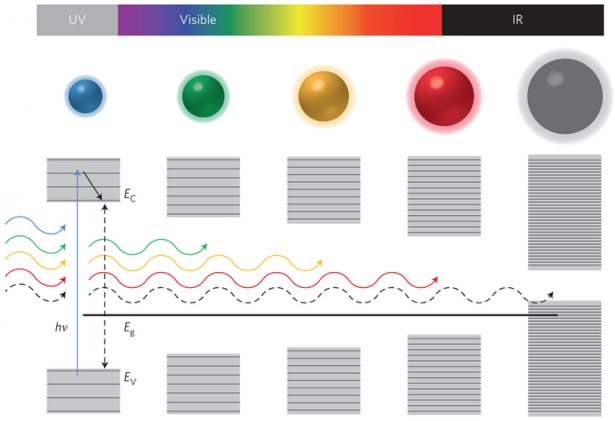

Figure 1.2: Schematic representation of the dependence on energy levels with size [32].

This simplistic model gives a first insight into the QD physics/properties.

Nevertheless the complexity of the QD physics grows when the atomic structure is taken into account. Atoms at the surface present dangling bonds which produce unoccupied, localised energy levels. This would make the surface of the quantum dot highly reactive, which usually is something to be avoided [14]. In order to avoid these dangling bonds, these are contacted with surfactants. These surfactants can also be used to help in the carrier transport process, since the absence of surface traps results in extended wavefunctions with more overlap between QDs.

Figure 1.2, showcases the general dependency of gap size with QD size. This is one of the most important properties of quantum dots.

1.5. The semiempirical pseudopotential method

The pseudopotential method is an approach for solving Hamiltonians that can be used to atomically model a system. In particular, when trying to solve the valence electron eigenstates for an atom, the core electrons have to be taken into account, at least for orthogonality reasons. As the electronic valence wavefunctions are not really far away from the core electrons, these wavefunctions overlap in the inner parts of the atom, which does not allow to solve them separately. On top of this problem it must be added the fact that the strong attractive potential of the nucleus makes the core electrons' wavefunctions very oscillating. This causes the valence states' wavefunctions to have high frequency components, which can increase the difficulty of finding the solution.

This poses a problem when trying to express the valence wavefunctions $\phi(\mathbf{r})$ as a set of plane waves as follows:

$$\phi_i(\mathbf{r}) = \sum_n c_i(\mathbf{G}_n) e^{i\mathbf{G}_n \mathbf{r}} \tag{1.3}$$

Equation 1.3 is the proposed ansatz for solving a Hamiltonian with plane waves, where $\mathbf{G}_n$ are the reciprocal lattice vectors, c_i are the plane wave

expansion coefficients and $\phi_i(\mathbf{r})$ is the solution of the Hamiltonian. In order to correctly describe the wavefunction, a very large set of plane waves needs to be considered because of their high frequency components.

To solve this problem one can redefine the valence wavefunction as the core electrons' wavefunctions, $\chi(\mathbf{r})$ plus another term, which we denote $\varphi(\mathbf{r})$:

$$|\phi\rangle = |\varphi\rangle + \sum_n a_n |\chi_n\rangle \tag{1.4}$$

where $|\chi_n\rangle$ is the *n-th* core wavefunction, a_n is the *n-th* expansion coefficient and $|\varphi\rangle$ will be called the pseudowavefunction.

It is important to notice how this can be interpreted. At relatively long distances from the atom the core electrons' wavefunctions vanish, and the pseudowavefunction $|\varphi\rangle$ tends to be identical to the valence wavefunction we are looking for. However, at the regions where the $|\chi_n\rangle$ summation is not negligible, $|\phi\rangle$ and $|\varphi\rangle$ are different. Anyway, when we solve the valence state wavefunction, we are usually interested in the outermost regions.

If we left-multiply equation 1.4 by a particular core wavefunction we obtain the following

$$\begin{aligned} \langle\chi_m|\,\phi\rangle &= \langle\chi_m|\,\varphi\rangle + \sum_n a_n \langle\chi_m|\,\chi_n\rangle = \\ &= \langle\chi_m|\,\varphi\rangle + a_m \langle\chi_m|\,\chi_m\rangle = 0 \\ &\rightarrow a_m = -\langle\chi_m|\,\varphi\rangle \\ |\phi\rangle &= |\varphi\rangle - \sum_n |\chi_n\rangle \langle\chi_n|\,\varphi\rangle \end{aligned} \tag{1.5}$$

We now apply the Hamiltonian to equation 1.5

$$
\begin{aligned}
H\left|\phi\right\rangle &= H\left|\varphi\right\rangle - \sum_n H\left|\chi_n\right\rangle\left\langle\chi_n\right|\left.\varphi\right\rangle \\
E\left|\phi\right\rangle &= H\left|\varphi\right\rangle - \sum_n E_n\left|\chi_n\right\rangle\left\langle\chi_n\right|\left.\varphi\right\rangle
\end{aligned} \tag{1.6}
$$

Where E is the valence wavefunction energy and E_n is the *n-th* core electron wavefunction energy. From equation 1.5 we can also write down the following relation

$$
\begin{aligned}
E\left|\phi\right\rangle &= E\left|\varphi\right\rangle - \sum_n E\left|\chi_n\right\rangle\left\langle\chi_n\right|\left.\varphi\right\rangle \\
\rightarrow H\left|\varphi\right\rangle &+ \sum_n (E - E_n)\left|\chi_n\right\rangle\left\langle\chi_n\right|\left.\varphi\right\rangle = E\left|\varphi\right\rangle;
\end{aligned} \tag{1.7}
$$

Combining 1.6 and 1.7 we obtain

$$
E\left|\varphi\right\rangle = T\left|\varphi\right\rangle + \left\{ V(\mathbf{r}) + \sum_n (E - E_n)\left|\chi_n\right\rangle\left\langle\chi_n\right| \right\}\left|\varphi\right\rangle \tag{1.8}
$$

H is the atomic Hamiltonian, T the kinetic energy operator, $V(\mathbf{r})$ the atomic potential, E the valence state wavefunction energy and E_n is the *n-th* core electron eigenenergy. The term in curly brackets is called the pseudopotential. Since $E > E_n$, we have that the pseudopotential is less confining than the attractive atomic potential, which is always negative due to its attractiveness nature. Thus the pseudowavefunction is less oscillating in the core region than the original wavefunction[37].

The pseudopotential in equation 1.8 is known as the Philips-Keinman pseudopotential [37] and it is not the only one[38–42]. We recall here that the pseudopotential method tries to find a pseudowavefunction that will be as close as possible to the valence state wavefunction in the outer region of the atom but will be smoother in its inner regions.

There are two approaches when using the pseudopotential methods, the empirical and semiempirical. In the empirical method, the pseudopotential is obtained by adjusting parameters in the reciprocal space, assuming that the potential can be expressed as a sum of atomic centered potentials and a spin orbit interaction term. In the semiempirical case, a non-locality is introduced making the potential dependent on the electronic angular momentum [37].

In this work the single quantum dot eigenstates were computed within the semiempirical pseudopotential framework at the University of Leeds (United Kingdom) using the Pescan code [43, 44] . As an example, in figure 1.3 we show the potential and wavefunctions isosurfaces for a particular case, a 1.2nm radius InAs quantum dot. For the potential, the isosurface corresponds to -0.025 Hartree and in the case of the wavefunctions, the isosurfaces corresponds to 1.5×10^{-5} bohr^{-3} probability density value. For further references on the method used, the reader can find more information at [37, 45, 46].

1.6. Systems considered in this work

In this work we calculate the properties of periodic systems made of quantum dots. There are a lot of factors or variables that configure such periodic systems (e.g. unit cell size, the primitive cell type, etc.), and we have developed a simulator that offers a great amount of possibilities to study. In order to narrow them down to a point where we can have a thorough and ordered discussion, we restrict ourselves to five types of systems. We are going to classify the systems according to their periodicity along each direction in space.

- QD molecule: Any arrangement of QDs that is finite in all directions is considered a QD molecule. It can be a particular number of quantum dots stacked along a line or forming different geometries. Through this work we restricted ourselves to model QD molecules as QDs stacks along a straight line in the z-axis. We called that particular form of QD molecule a QD stack to distinguish it from other spacial arrangements.

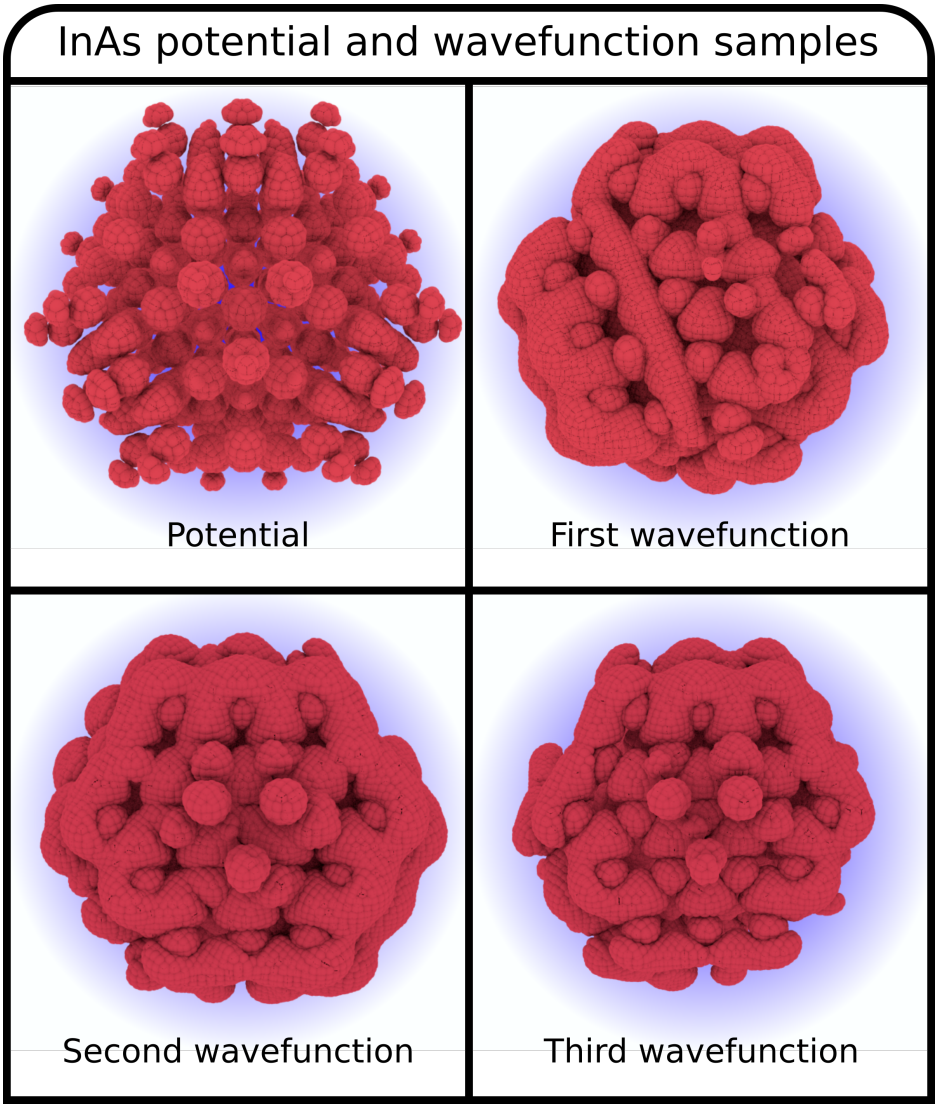

Figure 1.3: For illustration purposes only, this figure shows the isopotential surface for -0.025 Hartree and isoprobability surfaces corresponding to 1.5×10^{-5} bohr^{-3} for the three lowest energy conduction band states in a InAs 1.2 nm radius quantum dot. The wavefunctions corresponds to the lowest energy states (from the first to the third states) in the conduction band of the QD.

- 1D periodic superlattice: A periodic structure that extends in only one dimension. We modeled this systems along the z-axis for better comparison with QD stacks.
- 2D periodic superlattice: A periodic structure that extends in two dimensions. These are always the x and y-axis.
- 2D periodic stack: This system configuration is periodic in two directions (usually the xy plane) but instead of having one QD per unit cell, it has a QD stack in the direction perpendicular to the periodic plane. The system may be also considered as a 2D periodic superlattice stack.
- 3D periodic superlattice: A periodic structure with one QD per unit cell periodically extended in three dimensions.

These systems are examples of the so-called superlattices. In the same manner that crystal lattices have a crystal basis of one or a group of atoms, superlattices have a crystalline basis of a large set of atoms, that could be atomic layers, quantum dots, etc. [47]

These systems are illustrated in figure 1.4

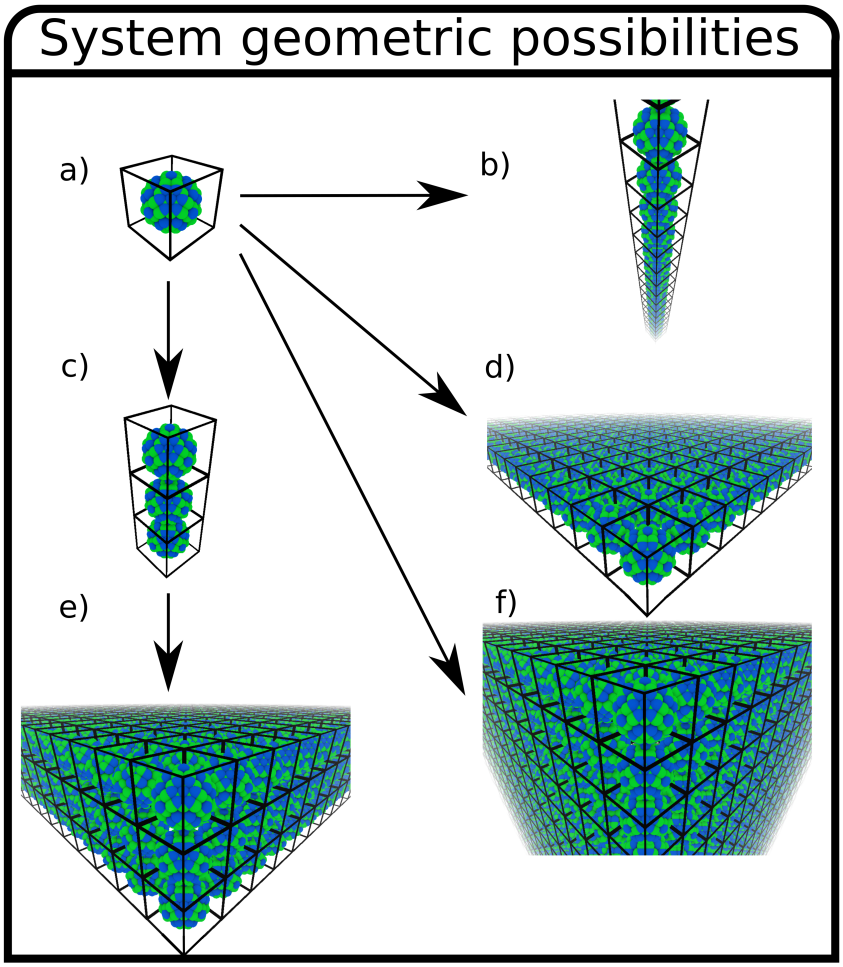

Figure 1.4: Schematic representation of the type of systems used throughout this work. a) isolated quantum dot, b) 1D periodic system, c) QD stack (the number of QD stacked is a parameter) d) 2D periodic system e) 2D periodic stack and f) 3D periodic system systems.

2

Tight Binding Method

2.1. Theoretical introduction to the tight binding model

The objective of this research is to study the collective behavior of a quantum dot array and to that end we proposed a tight binding model. Tight binding is widely applied for infinite and finite systems where the electrons are tightly bound to the ions, such as semiconductors, insulators, and molecules [48–50]. In this work we have used this approach to study both infinite and finite systems, in 1D, 2D and 3D arrangements. In the present work we have prioritized the 2D periodic system, for which we have computed electronic structure, electron transport and photon absorption.

The tight binding model is an approximation in which the wavefunction basis of the system under study is proposed as a linear combination of the isolated systems' wavefunctions (ϕ)[51]. These isolated systems may be a single atom, a molecule or, as in this research, a quantum dot, or a quantum dot molecule. This is an acceptable approximation when the isolated wavefunctions of the system have small overlaps between them (figure 2.1). When this is the case, the system Hamiltonian can be seen as a perturbation over the isolated system, which allows the use of the same wavefunctions to solve the new problem[52].

System eigenfunctions are highly dependent on the distance between systems or, in the case of crystals, the lattice constant. In the case of infinite systems, as the lattice constant grows, energy bands tend to flatten around the QD eigenenergies. In the case of finite systems, their discrete energy levels tend to approach.

2.1.1. Tight binding model overview

In this section we introduce the formalism followed along this work. For simplicity the equations correspond to infinite systems having a single quantum dot or quantum dot stack basis. The mathematical formalism used to deal with finite systems or superlattices whose basis is a QD stack is an adaptation of it. Let us

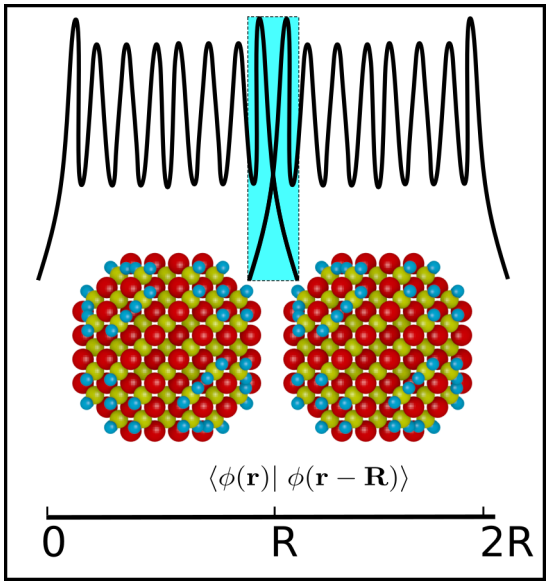

Figure 2.1: Tight binding illustrative figure. The black curves represent a simplified version of an arbitrary QD wavefunction, the cyan area represents the overlapping region integral.

start by using the set of superlattice point vectors $\mathbf{R}_v$. The sum of the isolated QD potentials creates the periodic potential with which the electron interacts. The Hamiltonian of such a system can be expressed as follows:

$$\begin{aligned} H_{tb} &= \frac{\mathbf{p^2}}{2m_e} + \sum_{\mathbf{R}_v} V(\mathbf{r}-\mathbf{R}_v) = \\ &= \frac{\mathbf{p^2}}{2m_e} + V(\mathbf{r}) + \sum_{\mathbf{R}_v \neq 0} V(\mathbf{r}-\mathbf{R}_v) = \\ &= H_{at} + \sum_{\mathbf{R}_v \neq 0} V(\mathbf{r}-\mathbf{R}_v) \end{aligned} \tag{2.1}$$

where H_{tb} is the system Hamiltonian, H_{at} the isolated QD or QD stack Hamiltonian, m_e is the rest electron mass, and $V(\mathbf{r}-\mathbf{R}_v)$ is the quantum dot potential at position $\mathbf{R}_v$. H_{at} fulfills the relation shown in equation 2.2

$$H_{at}\left|\phi_n\right\rangle = E_n\left|\phi_n\right\rangle \tag{2.2}$$

where E_n and ϕ_n are the isolated quantum dot eigenstates' energy and wavefunction, obtained by the semiempirical pseudopotential method explained in section 1.5.

In equation 2.1 it is shown that the system Hamiltonian can be written as a sum of an isolated quantum dot Hamiltonian H_{at} plus an extra term containing all the neighboring quantum dot potentials forming the superlattice. If the sum of neighboring QD potentials is small, the perturbative theory[53] allows the use of the isolated QD wavefunctions to solve the system Hamiltonian. This happens when the wavefunction strongly decays at any distance $\mathbf{R}_v$. Provided this condition, the proposed solution is written as

$$\psi_m(\mathbf{r}) = \sum_{n,\mathbf{R}_s} b_{m,n}(\mathbf{R}_s)\phi_n(\mathbf{r}-\mathbf{R}_s) \tag{2.3}$$

Here, the subscript m indicates the *m-th* solution to the Hamiltonian, $b_{m,n}(\mathbf{R}_s)$ are the expansion coefficients for the *m-th* solution, at position $\mathbf{R}_s$ and ϕ_n is the *n-th* wavefunction of the quantum dot.

Applying the Hamiltonian on this ansatz we obtain the equation to solve

$$\left[H_{at} + \sum_{\mathbf{R}_v\neq 0} V(\mathbf{r}-\mathbf{R}_v)\right]\left[\sum_{n,\mathbf{R}_s} b_{m,n}(\mathbf{R}_s)\phi_n(\mathbf{r}-\mathbf{R}_s)\right] = E_m\left[\sum_{n,\mathbf{R}_s} b_{m,n}(\mathbf{R}_s)\phi_n(\mathbf{r}-\mathbf{R}_s)\right] \tag{2.4}$$

where E_m is the corresponding energy of the system's ψ_m wavefunction.

At this point the theoretical development for periodic and non-periodic systems have their particular considerations.

2.1.2. Tight binding of a periodic system

Because of the periodicity of the system, the proposed wavefunction must satisfy the Bloch theorem

$$\psi_m(\mathbf{r}+\mathbf{R}_v) = \psi_m(\mathbf{r})e^{i\mathbf{q}\mathbf{R}_v} \tag{2.5}$$

which allows to write the wavefunctions as

$$\psi_m(\mathbf{r}) = \frac{1}{\sqrt{N}}U_{m,\mathbf{q}}(\mathbf{r})e^{i\mathbf{q}\mathbf{r}} \tag{2.6}$$

where $\mathbf{q}$ is a vector of the first Brillouin zone of the superlattice reciprocal space, N is the number of unit cells and $U_{m,\mathbf{q}}(\mathbf{R})$ is a function that has the periodicity of the lattice.

Applying the Bloch theorem to equation 2.3 we obtain

$$\begin{aligned}
\psi_m(\mathbf{r}+\mathbf{R}_m) &= \sum_{n,\mathbf{R}_s} b_{m,n}(\mathbf{R}_s)\phi_n(\mathbf{r}-\mathbf{R}_s+\mathbf{R}_m) \\
\text{defining} \quad \mathbf{R}_p &\equiv \mathbf{R}_s - \mathbf{R}_m \\
&\sum_{n,\mathbf{R}_p} b_{m,n}(\mathbf{R}_m+\mathbf{R}_p)\phi_n(\mathbf{r}-\mathbf{R}_p) = \\
&= \sum_{n,\mathbf{R}_p} b_{m,n}(\mathbf{R}_p)\phi_n(\mathbf{r}-\mathbf{R}_p)e^{i\mathbf{q}\mathbf{R}_m}
\end{aligned}$$

where the last equivalence is a consequence of $\sum_{n,\mathbf{R}_p} b_{m,n}(\mathbf{R}_p)\phi_n(\mathbf{r}-\mathbf{R}_p)$ being the proposed Bloch function of equation 2.3 and in consequence it must satisfy the Bloch's condition. From here it is deduced that the expansion coefficients can be rewritten as a function of the coefficient at $\mathbf{R}_p = 0$

$$b_{m,\mathbf{q},n}(\mathbf{R}_p) = b_{m,\mathbf{q},n}(0)e^{i\mathbf{q}\mathbf{R}_p} \tag{2.7}$$

The wavefunction also depends on $\mathbf{q}$ and thus, for the sake of clarity, this subscript $\mathbf{q}$ is also included in the wavefunction notation. This subscript changes between wavefunctions,

$$\psi_{m,\mathbf{q}}(\mathbf{r}) = \sum_{n,\mathbf{R}_s} b_{m,\mathbf{q},n} e^{i\mathbf{q}\mathbf{R}_s} \phi_n(\mathbf{r} - \mathbf{R}_s) \tag{2.8}$$

where the 0 has been omitted for notation clarity.

Applying the Hamiltonian operator (eq. 2.4) we obtain[1]

$$\begin{aligned} H_{tb} \left|\psi_{m,\mathbf{q}}(\mathbf{r})\right\rangle &= \sum_{n,\mathbf{R}_s} b_{m,\mathbf{q},n} e^{i\mathbf{q}\mathbf{R}_s} \left\{ \frac{\mathbf{p}^2}{2m_e} + \sum_{\mathbf{R}_v} V(\mathbf{r} - \mathbf{R}_v) \right\} \left|\phi_n(\mathbf{r} - \mathbf{R}_s)\right\rangle = \\ &= E_{m,\mathbf{q}} \sum_{n,\mathbf{R}_s} b_{m,\mathbf{q},n} e^{i\mathbf{q}\mathbf{R}_s} \left|\phi_n(\mathbf{r} - \mathbf{R}_s)\right\rangle \end{aligned} \tag{2.9}$$

In order to obtain the expansion coefficients and the eigenenergies, we left-multiply equation 2.9 by $\langle\phi_t(\mathbf{r})|$ and we obtain

$$\begin{aligned} \left\langle\phi_t(\mathbf{r})\right| H_{tb} \left|\psi_{m,\mathbf{q}}(\mathbf{r})\right\rangle &= \sum_{n,\mathbf{R}_s} b_{m,\mathbf{q},n} e^{iq\mathbf{R}_s} \left\langle\phi_t(\mathbf{r})\right| \left\{ \frac{\mathbf{p}^2}{2m} + \sum_{\mathbf{R}_v} V(\mathbf{r} - \mathbf{R}_v) \right\} \left|\phi_n(\mathbf{r} - \mathbf{R}_s)\right\rangle = \\ &= E_{m,\mathbf{q}} \sum_{n,\mathbf{R}_s} b_{m,\mathbf{q},n} e^{i\mathbf{q}\mathbf{R}_s} \left\langle\phi_t(\mathbf{r})\right| \phi_n(\mathbf{r} - \mathbf{R}_s)\right\rangle ; \\ & A_q \mathbf{b}_{m,\mathbf{q}} = E_{m,\mathbf{q}} B_{\mathbf{q}} \mathbf{b}_{m,\mathbf{q}} \end{aligned} \tag{2.10}$$

Equation 2.10 represents a diagonalization problem. We also show its matrix representation, where A_q and B_q matrices are $M \times M$ dimensional. For a particular $\mathbf{q}$ the diagonalization process yields M orthogonal wavefunctions. As stated before, a change in $\mathbf{q}$ modifies the system of equations, resulting in a different set of eigenenergies. A sweep in $\mathbf{q}$ yields the energy bands of the periodic system.

There is another approximation to be made, that is to use only the nearest neighbours in the calculation, thus making finite the summations over $\mathbf{R}_v$ and $\mathbf{R}_s$. This approximation is in accordance with the tight binding model, in which

[1] In the following the notation of bras and kets includes $\mathbf{r}$ (not displaced function) and $\mathbf{R}$ (indicating a particular superlattice position).

the potential is strongly confining around each lattice point, and the overlapping between QDs wavefunctions are small.

As a last step, the norm has to be calculated. Returning to equation 2.8 we calculate the following overlap.

$$\begin{aligned}\langle\psi_{m,\mathbf{q}}(\mathbf{r})|\psi_{m,\mathbf{q}}(\mathbf{r})\rangle &= \sum_{n,\mathbf{R}_s}\sum_{n',\mathbf{R}'_s} b^*_{m,\mathbf{q},n}b_{m,\mathbf{q},n'}e^{i\mathbf{q}(\mathbf{R}_s-\mathbf{R}'_s)}\,\langle\phi_n(\mathbf{r}-\mathbf{R}_s)|\phi_{n'}(\mathbf{r}-\mathbf{R}'_s)\rangle = \\ &\quad \mathbf{R}_p \equiv \mathbf{R}_s - \mathbf{R}'_s \rightarrow \mathbf{R}'_s = \mathbf{R}_s - \mathbf{R}_p \\ &= \sum_{n,\mathbf{R}_s}\sum_{n',\mathbf{R}_p} b^*_{m,\mathbf{q},n}b_{m,\mathbf{q},n'}e^{i\mathbf{q}\mathbf{R}_p}\,\langle\phi_n(\mathbf{r}-\mathbf{R}_s)|\phi_{n'}(\mathbf{r}+\mathbf{R}_p-\mathbf{R}_s)\rangle = \\ &= N\sum_{n}\sum_{n',\mathbf{R}_p} b^*_{m,\mathbf{q},n}b_{m,\mathbf{q},n'}e^{i\mathbf{q}\mathbf{R}_p}\,\langle\phi_n(\mathbf{r})|\phi_{n'}(\mathbf{r}+\mathbf{R}_p)\rangle = NK_{m,\mathbf{q}} = 1\end{aligned}$$

Where N is the number of unit cells and $K_{m,\mathbf{q}}$ is:

$$\begin{aligned}K_{m,\mathbf{q}} &\equiv \sum_{n}\sum_{n',\mathbf{R}_p} b^*_{m,\mathbf{q},n}b_{m,\mathbf{q},n'}e^{i\mathbf{q}\mathbf{R}_p}\,\langle\phi_n(\mathbf{r})|\phi_{n'}(\mathbf{r}+\mathbf{R}_p)\rangle \\ \psi(\mathbf{r})_{m,\mathbf{q}} &= \frac{1}{\sqrt{NK_{m,\mathbf{q}}}}\sum_{n,\mathbf{R}_s} b_{m,\mathbf{q},n}e^{i\mathbf{q}\mathbf{R}_s}\phi_n(\mathbf{r}-\mathbf{R}_s)\end{aligned} \tag{2.11}$$

$K_{m,\mathbf{q}}$ is the wavefunction norm. The only quantities affected by normalisation are the tight binding expansion coefficients obtained from diagonalization. Henceforth, $\psi_{m,\mathbf{q}}(\mathbf{r})$ is the normalized previously presented wavefunction. For the sake of simplicity, we used the same notation.

2.1.3. Tight binding of a non-periodic system

In this case we are not able to use the Bloch function as an ansatz but anyway, like in the periodic case, we start by applying the Hamiltonian (equation 2.1) to

the wavefunction (equation 2.3) and left-multiplying it by $\langle\phi_t(\mathbf{r}-\mathbf{R}'_s)|$.

$$\begin{aligned}\langle\phi_t(\mathbf{r}-\mathbf{R}'_s)|\,H_{tb}\,|\psi_m\rangle &= \sum_{\mathbf{R}_s,n}\epsilon_n b_{m,n}\,\langle\phi_t(\mathbf{r}-\mathbf{R}'_s)|\;\phi_n(\mathbf{r}-\mathbf{R}_s)\rangle \\ &+ \sum_{R_s,n} b_{m,n}\,\langle\phi_t(\mathbf{r}-\mathbf{R}'_s)|\sum_{\mathbf{R}_v\neq\mathbf{R}_s} V(\mathbf{r}-\mathbf{R}_v)\,|\phi_n(\mathbf{r}-\mathbf{R}_s)\rangle \\ &= E_m\sum_{\mathbf{R}_s,n} b_{m,n}\,\langle\phi_t(\mathbf{r}-\mathbf{R}'_s)|\;\phi_n(\mathbf{r}-\mathbf{R}_s)\rangle \qquad (2.12)\\ &= A\mathbf{b_m} = E_m B\mathbf{b_m}\end{aligned}$$

In this case we do not have a reciprocal vector $\mathbf{q}$ to sweep through because there is no reciprocal space properly defined. We have a single matrix diagonalization problem. The numerical difference, however, is in the wavefunction which is shown again below.

$$\psi_m(\mathbf{r}) = \sum_{n,\mathbf{R}_s} b_{m,n}(\mathbf{R}_s)\phi_n(\mathbf{r}-\mathbf{R}_s) \qquad (2.13)$$

In the periodic case, we have a subscript $\mathbf{q}$ that changes for each vector in the first Brillouin zone. In the non-periodic case we have one diagonalization problem for the whole system. In the periodic case the length of the set of coefficients used in the expansion $b_{m,\mathbf{q},n}$ is M, i.e. the number of isolated QD eigenstates. In the non-periodic case, it is equal to the total number of wavefunctions $M \times N$, i.e. equal to the number of isolated QD eigenstates times the number of QDs in the system. The Bloch theorem (equation 2.7) does not apply and therefore the subsequent relations among the $b_{m,n}(\mathbf{R}_s)$ coefficients does not hold.

The normalisation is very similar to the periodic one and comes from the same mathematical procedures. The normalized wavefunction is shown below.

$$\psi_m(\mathbf{r}) = \frac{1}{\sqrt{K_m}}\sum_{n,\mathbf{R}_s} b_{m,n}(\mathbf{R}_s)\phi_n(\mathbf{r}-\mathbf{R}_s) \qquad (2.14)$$

$$K_m = \sum_{t,\mathbf{R}'_s}\sum_{n,\mathbf{R}_s} b^*_{m,t}b_{m,n}\,\langle\phi_t(\mathbf{r}-\mathbf{R}'_s)|\phi_n(\mathbf{r}-\mathbf{R}_s)\rangle \qquad (2.15)$$

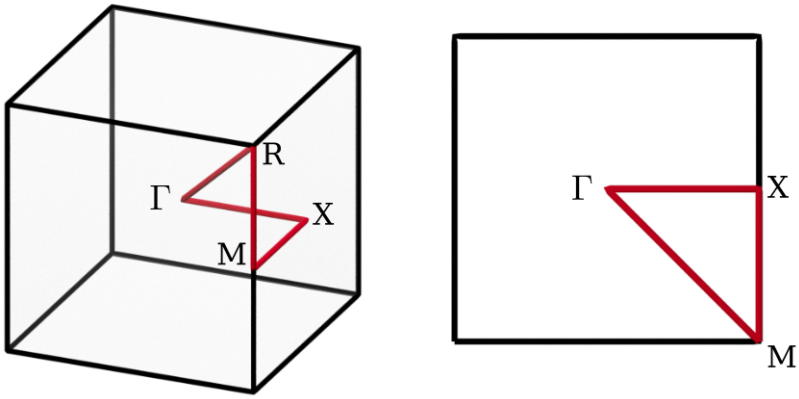

Figure 2.2: Representation of the path along the selected symmetry points in which the energy bands are represented.

2.2. Application to periodic quantum dot arrays

Quantum dots are nanometer sized crystals. By means of its periodic repetition in space we can create a second kind of lattices, the so-called "superlattices". The mathematical formalism resembles the one for regular crystals. A band electronic structure arises because of the quantum dot wavefunction overlaps, as it happens in atomic crystals. These overlaps are not as strong as in atomic crystals, and as a consequence the electronic structure is formed by a set of narrower energy bands, called "minibands", having widths in the order of hundreds of meV.

In figure 2.2 the first Brillouin zone for the studied 3D and 2D systems is shown, alongside with the energy representation path for the minibands that will be used throughout this work.

Figure 2.3 shows the energy levels obtained from the semiconductor conduction band of an InAs R=12 Å quantum dot compared to the eigenstates energies of a QD molecule of two InAs QDs vertically stacked (two QD stack). We can see how energy levels that were degenerated split under the interaction between

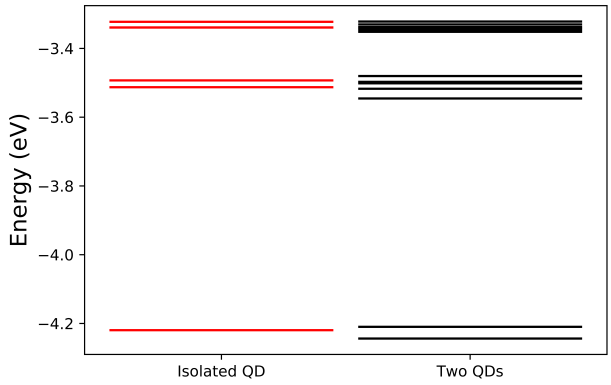

Figure 2.3: Energy level comparison between the isolated InAs R=12 Å QD and two stacked QDs of the same type.

QDs. Figure 2.4 shows the energy minibands when the InAs quantum dot is repeated periodically along XY plane (2D periodic superlattice) with the minimum superlattice constant (in this case it is said that quantum dots are one bond length apart). Figure 2.5 shows the same periodical arrangement but using the two-stacked quantum dots as the unit cell. Lastly, figure 2.6 shows a periodic 3D arrangement (3D superlattice) in which the single QD is forming a simple cubic supperlattice.

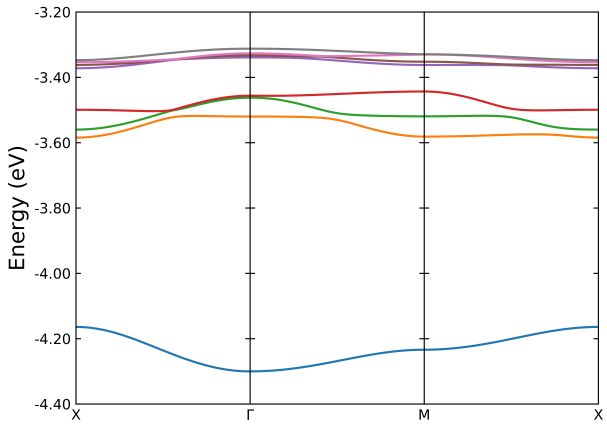

Figure 2.4: Miniband structure of the InAs R=12 Å 2D periodic system.

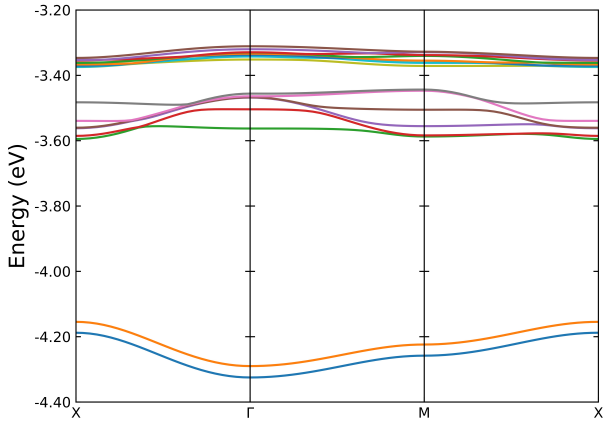

Figure 2.5: Miniband structure of the 2D periodic stack with unit cell composed by two stacked InAs R=12 Å QDs. The observed energy splitting is due to interaction between the QD layers, equivalently to the observed splitting in figure 2.3 due to QD interaction.

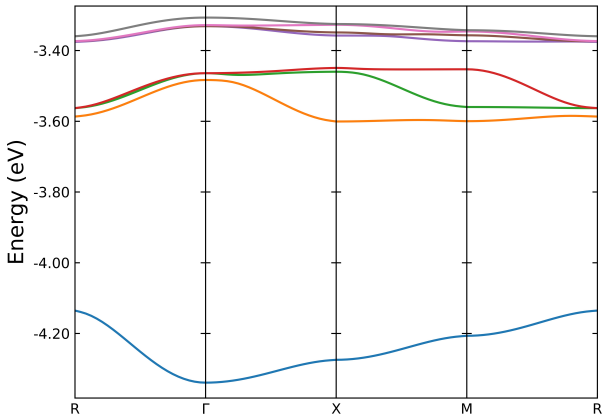

Figure 2.6: Miniband structure for the InAs R=12 Å periodic 3D array. Here quantum dots are repeated periodically along the three axes.

There is an important note in the computational side of the applicability of this theory. Periodical systems are infinite. Its reciprocal space has a continuum range of available values of **q**. In order to solve the miniband structure we sampled the first Brillouin zone using a particular number of vectors, Q_s. In this study this sampling varies from 51 to 501 points per direction, depending on the calculation.

There is another important aspect regarding the number of minibands considered within a particular calculation. For computational purposes we selected a suitable set of QD states as the basis for the tight binding calculation. Computational complexity scale approximately as M^2, thus being important to restrict ourselves only to a set of significant isolated QD eigenstates.

3

Quantum dot array electron mobility model

3.1. General Overview

In this chapter a model to calculate ohmic mobility is presented. There are two important proposed mechanisms used to approach electron transport in the literature of quantum dots arrays: hopping transport and band-like transport.

In the first one, as quantum dots have different energy level values due to size dispersion, the electron gains or loses energy in order to change its position from a quantum dot to another[54–56]. To do this, the electron interacts with phonons, gaining or loosing the energy difference between the states, (figure 3.1). Thus, this model has a particular feature: mobility generally increases with temperature, since the higher the temperature, the more electron-phonon scattering occurs [57, 58]. The energetic difference between neighbouring QDs changes from point to point in the system but it is useful to define a macroscopic quantity, called the activation energy (E_a) which is, on average, the energy that the electron needs to "hop" from a QD to the next. Higher activation energies are characteristic of more disordered systems. There are many hopping models, depending on which mechanism is responsible for the electron hopping [59–63] but as an example we use the one in [64], defined by equation 3.1, which models the electronic mobility as:

$$\mu = \frac{ed^2 E_a}{3hkT} \mathcal{T} e^{-E_a/kT} \tag{3.1}$$

where e is the fundamental charge, d is the distance between QDs' centers, $\mathcal{T}$ is the coherence between initial and final states the electron is hopping, h is the Planck constant and k is the Boltzmann constant. Figure 3.2 shows how the mobility slope changes with temperature and activation energy for this particular model.

On the other hand, in the miniband transport model the electron mobility is calculated in an infinite periodic superlattice, in which a portion of QDs with a different size, referred to as "impurities", are responsible for electron scattering. We modeled these impurities as QDs that have a smaller radius than the periodic

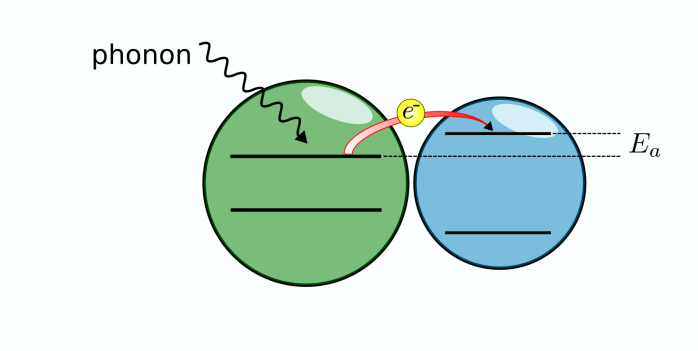

Figure 3.1: Illustration of the hopping effect. QDs have a size-dependent gap and other circumstantial properties (e.g. ligands, pasivation), that change the probability for the electron to *hop* from one QD to the other.

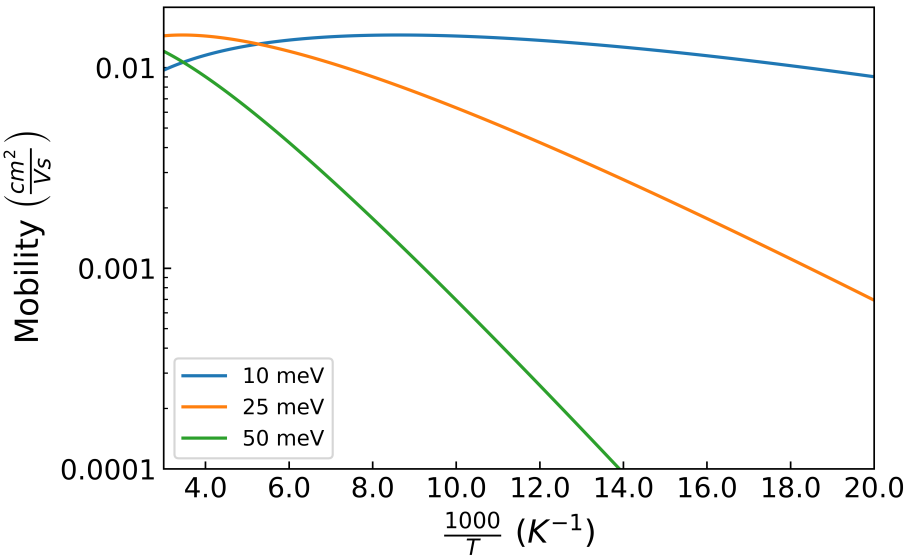

Figure 3.2: Electron mobility plots of equation 3.1 for different activation energies, as a function of temperature.

ones. In contrast with the hopping model, the electric carrier energetic states does not depend on the carrier real space location. The dispersion relation shown in equation 2.10 relates the electron energy, E, with the carrier's reciprocal vector, $\mathbf{q}$.

Each electron state in the superlattice has a velocity in the real space, which is related to the energy gradient in the reciprocal space as:

$$\mathbf{v}(\mathbf{q}_f)_m = \frac{1}{\hbar}\nabla_q E_m(\mathbf{q})\Big|_{q_f} \tag{3.2}$$

where $\mathbf{v}$ is the electron velocity, $\mathbf{q}_f$ the reciprocal space vector and the subscript m is the miniband where the electron is is located.

One of the most clear procedures to deduce about what transport mechanism is dominating is to measure the mobility as a function of temperature[65]. Generally in band-like transport carrier mobility decreases with increasing temperatures[66], while hopping transport behaves oppositely as it has previously pointed out and illustrated in figure 3.2.

The hopping model applies well on disordered systems, which are usually the case in QD films and other macroscopic QD systems [56, 67, 68]. But, as improvements are made in device fabrication, these can achieve better ordering (periodicity) making it necessary to search for other models to explain the features that arise in these novel systems [2–4]. That is why the mobility calculations carried out in this investigation are based on a band-like transport approach. We developed a simulator to improve our understanding on carrier dynamics and to give an insight into which systems and conditions are good candidates for achieving high electron mobility QD superlattices for experimentalists.

To summarize, when mobility of macroscopic systems based on quantum dots is considered, two main models emerge: the hopping transport model and the band-like transport model. Each departs from different assumptions in terms of quantum dots ordering quality. One way for the experimental researcher to know which transport mechanism dominates in a particular device is to measure

the mobility dependence with temperature[65].

3.2. Scattering Mechanism

As it will be shown later, in the band-like transport model there are scattering mechanisms interrupting the carrier movement and making it to start the process of acceleration all over again. The elapsed time between two consecutive scattering events is called *time of flight* (TOF) and the average TOF is the inverse of the average scattering rate.

Following the previous work of Shabaev et al. [69] we studied band-like transport in QD superlattices focusing on lattice impurities as the main scattering mechanism to investigate electron transport in the system. Impurities in this work are modeled as different sized (smaller) QDs that break periodicity. Other authors claim deep states [3, 70] or charge donors [71] may be as relevant as size variation scattering mechanisms when studying carrier transport in these systems but, as shown in [69], these mechanisms may be less relevant. Taking into consideration that impurity scattering has a prominent role in carrier transport, and the fact that this mechanism is elastic (the carrier energy does not change after a scattering event) and temperature independent, there is an open question to be asked: how temperature affects this transport model? Phonon scattering, which is a temperature dependent scattering mechanism, is not considered to be relevant in the description of carrier transport. Authors consider that the phonon scattering rates are several orders of magnitude smaller than impurity scattering rates [69]. This could be acceptable due to the phonon bottleneck in nanostructures[72]. Phonon dispersion relation has not been properly computed in QD arrays to the author's knowledge, although some efforts have been made [73, 74]. Nevertheless phonons are crucial when thermalising the system. The presented model includes them indirectly, not as a scattering mechanism limiting the TOF but as the thermalising mechanism that populates the minibands following a close-to-equilibrium occupation distribution.

In the case of this work, it has been considered that the only scattering mechanism to limit the TOF are impurities in the superlattice in the form of differently sized QDs. The presence of different sized QDs in the periodic lattice is almost inevitable during QD synthesis. We define the impurity concentration as the fraction of impurity quantum dots in the periodic system, ν. Impurity concentration is a fundamental property to evaluate the quality of the device. In a general case, there would be a size distribution $g_\nu(R_{QD})$ containing the system information about the number of quantum dots per unit length, area or volume having a particular radius R_{QD}. If $g_\nu(R_{QD})$ is too wide (great size dispersion) the periodicity assumption is not true and thus the formalism developed in chapter 2 does not hold. If $g_\nu(R_{QD})$ is too narrow (close to perfect periodicity), the effects of size dispersion will not be the dominant scattering phenomena limiting charge mobility and this model will predict higher mobilities than the measurements (phonon scattering would be relevant in that situation). There is no exact quantitative point were it can be assured that a model applies or not. Nevertheless, we limited the systems at study to a scenario in which there is a negligible probability of correlation between impurities (this limits the maximum concentration) but also the impurity concentration has to be sufficiently high to pose our proposed scattering mechanism as the dominant one. Thus, in this work we considered the plausible range for impurity concentration to be $\nu \in [0.001, 0.01]$.

As the different sized quantum dots are of the same material and are considered to be close in radius to the periodic ones, their wavefunction energies will be close to their periodic counterparts . This allows us to treat the problem of the different sized QDs as a perturbation over the periodic lattice. As we are only interested in the first order approximation of the systems, we use the Fermi's Golden Rule. The scattering rate is obtained from the superlattice eigenstates, $|\psi_{\mathbf{q}}(\mathbf{r})\rangle$ and the difference between the non-periodic QD potential, $V_d(\mathbf{r})$, and the periodic one, $\Delta V(\mathbf{r}) = V_d(\mathbf{r}) - V(\mathbf{r})$. The Fermi's Golden Rule in a general case is

$$\Gamma_{i,f} = \frac{2\pi}{\hbar} \left| \langle \psi_{c,q_f} | \, \Delta V \, | \psi_{c,q_i} \rangle \right|^2 \rho(E_f) \tag{3.3}$$

Where ρ is the superlattice density of states and $\Gamma_{i,f}$ is the scattering rate

for transitions from the *i-th* to the *f-th* state.

A problem when implementing eq. 3.3 is that is meant to be used in systems with a continuous energy occupation. However, at the simulation level a finite discretization of the reciprocal space is used, Q_s, in order to make the algorithm feasible.

In fact, for a finite discretization, the density of states changes from a continuous form to a series of Dirac deltas, $\rho(E) \rightarrow \sum_{E_f} \delta(E - E_f)$. To calculate the transport model we chose to approximate this delta to a window function of ΔE width (we call this window the *energy conservation window*) and the miniband is subdivided in N different energy levels, each of them having an amplitude of ΔE. These levels are called *energetic intervals* and all the states that are contained in each of them are mutually accessible via size dispersion scattering processes as if they had the exact same energy.

In order to do this, equation 3.3 has to be rewritten to account for both the fact that this simulated system has been sampled in the reciprocal space and the energy conservation window. Equation 3.4 is the Fermi's Golden Rule, as used in this investigation. The wavefunction is written as the coefficient expansion, with the normalization factors from section 2.1.2.

$$\begin{aligned}
\Gamma_{i,f} &= N_i \frac{N}{Q_s} \frac{2\pi}{\hbar} \frac{1}{\Delta E} \left| \langle \psi_{cq_f} | \Delta V | \psi_{cq_i} \rangle \right|^2 \\
&= N_i \frac{N}{Q_s} \frac{2\pi}{\hbar} \frac{1}{\Delta E} \frac{1}{N^2 K_{c,q_i} K_{c,q_f}} \left| \sum_{m,s} b^*_{cmq_f} b_{csq_i} \int \phi^*_m(\mathbf{r}) \Delta V(\mathbf{r}) \phi_s(\mathbf{r}) d\mathbf{r} \right|^2 \\
&= \frac{\nu}{Q_s} \frac{2\pi}{\hbar} \frac{1}{\Delta E} \frac{1}{K_{c,q_i} K_{c,q_f}} \left| \sum_{m,s} b^*_{cmq_f} b_{csq_i} \int \phi^*_m(\mathbf{r}) \Delta V(\mathbf{r}) \phi_s(\mathbf{r}) d\mathbf{r} \right|^2 \qquad (3.4)
\end{aligned}$$

There are four new terms added to the Fermi's Golden Rule.

- N_i is the total number of impurity quantum dots in the lattice, since the Fermi's Golden Rule is for one scattering centre with no correlation between impurities.

- $\nu = \frac{N_i}{N}$ is the impurity concentration in the superlattice.

- $\frac{N}{Q_s}$ is due to the fact that each point in our discretization of the reciprocal space represents a group of physical $\mathbf{q}$ reciprocal space vectors. This number is equal to the total quantum dots in the lattice, divided by the selected discretization space.

- $\frac{1}{\Delta E}$ is a normalisation factor, due to the fact that $\delta(E - E_f)$ has been modeled as a window function, $\Theta(E - E_i) - \Theta(E - E_f)$, where E_i and E_f are the minimum and maximum energies respectively of the *i-th* energetic interval and $\Theta(E)$ is the step function.

In this work, we have implemented the model to study electron transport in the lowest conduction energy miniband. As it is shown in figure 2.4, the lowest energy miniband is placed away from the next one. This behaviour has been observed in all the studied systems in this work because of the particular atomic orbital configuration of the considered semiconductors [65, 75, 76]. This miniband is assumed to be the one having a higher occupation in normal conditions within the presented miniband set. Therefore carrier transport would be only relevant in it. Very high doping or other extreme conditions may lead to Fermi levels surpassing the conduction band edge, but in normal conditions the Fermi level would be below it and, in consequence, minibands over the lowest one can be expected to be unoccupied.

3.3. The Markov Chain

At this point, there is a known scattering rate $\Gamma_{i,f}$ between all states in the miniband. Due to the elasticity of this scattering mechanism, all the scattering rates between crystal eigenstates from different energy intervals are 0 and can be discarded because of energy conservation. Focusing on a particular energetic

interval, the scattering rates can be expressed as a matrix of non-zero elements

$$\Gamma = \begin{pmatrix} \Gamma_{0,0} & \Gamma_{0,1} & \cdots & \Gamma_{0,n-1} \\ \Gamma_{1,0} & \Gamma_{1,1} & \cdots & \Gamma_{1,n-1} \\ \vdots & \vdots & \vdots & \vdots \\ \Gamma_{n-1,0} & \Gamma_{n-1,1} & \cdots & \Gamma_{n-1,n-1} \end{pmatrix}$$

where n is the number of states of the energy interval, which may vary from interval to interval. From this matrix it can be defined the probability matrix $\mathbf{P}$. This would represent the probability to end the flight in a state f from a starting state i.

$$P_{i,f} = \frac{\Gamma_{i,f}}{\sum_{f'} \Gamma_{i,f'}} \tag{3.5}$$

Using the probability matrix it is possible to compute the probability of the electron being in each state within the energy interval as follows. Let us define the occupation state vector as:

$$\mathbf{S} = \begin{pmatrix} S_0 \\ S_1 \\ \vdots \\ S_{n-1} \end{pmatrix} \tag{3.6}$$

where S_i is the probability that the electron occupies the *i-th* state. With this formalism it is possible to find the occupation probability after a scattering event by multiplying $\mathbf{P} \cdot \mathbf{S}$. In this manner, the occupation state after t scattering events is $\mathbf{S}_t = \mathbf{M}^t \cdot \mathbf{S_0}$. In this manner it is possible to represent the occupation probability for each state after any number of scattering events. This is known as the Markov chain[77], and it represents a huge improvement on calculation efficiency when compared to Monte Carlo algorithms. A thermalised state would be, as always, one in which the occupation state $\mathbf{S}$ would not depend on the initial state. In the Markov chain this is done by multiplication of the probability matrix until the terms $P_{i,f}$ converge. As these equilibrium values do not depend on the initial state occupation, the terms $P_{i,f}$ do not change with the column index f, and therefore the carrier equilibrium probability information is contained in the

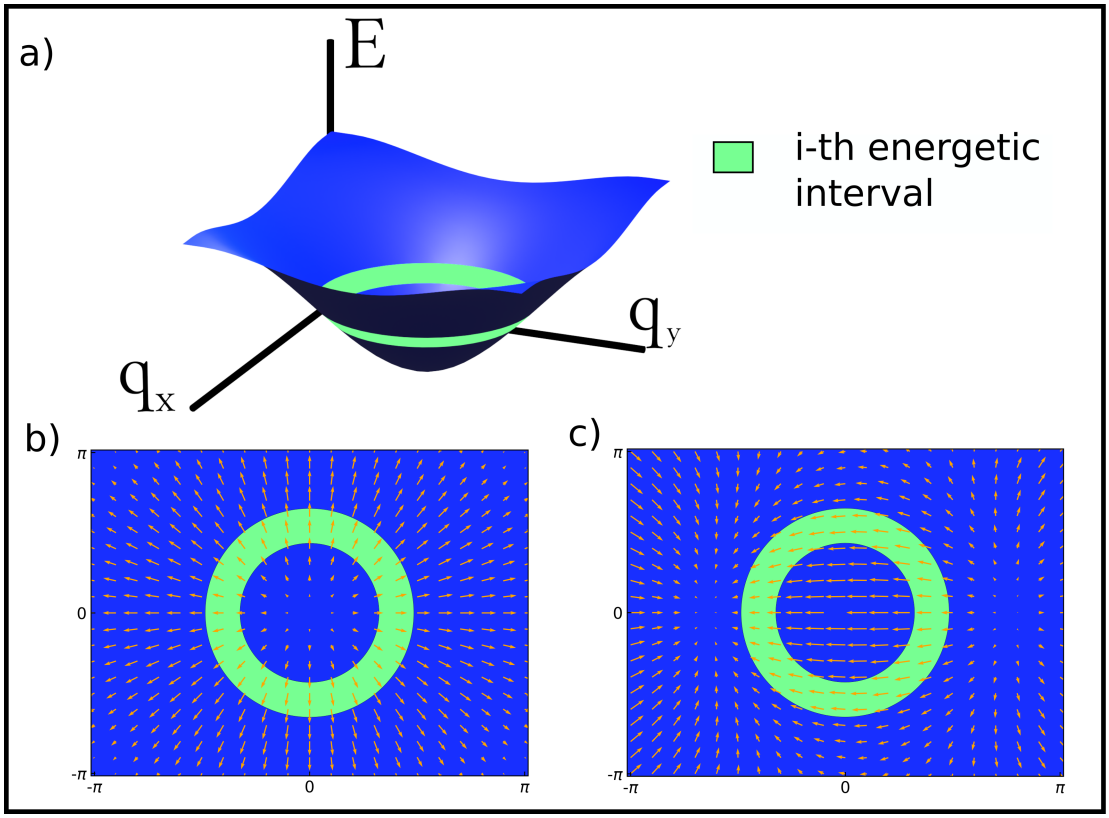

Figure 3.3: Schematic representation of the influence of electric field in velocity. a) 3D representation of a regular miniband, highlighting a particular energetic interval. b) The same miniband and energetic interval with a vector field representation of the equilibrium velocities, i.e. those that exist even if the external electric field is zero (they mutually cancel). c) Vector field representation of the difference between the velocity under electric field and the equilibrium velocity. This vector field is for illustration purposes only, showing how velocity due to the electric field changes with the miniband curvature. It can be seen that, at a certain point near the Brillouin zone limits, these velocities change direction, showing the effects of the inflection point.

one dimensional matrix columns. Thus it can be expressed as a one dimensional vector, $\hat{\mathbf{P}}$ (note the " ˆ " to differentiate the one dimensional vector from the matrix).

After a scattering event, each state electron has a particular probability of being the one from which the scattered carrier will start a new flight. These probabilities will be denoted as $\hat{P}_i$ for the *i-th* state of the energy interval.

There is another important quantity to define from scattering rates for each state, the average time of flight (TOF) $\langle t_i \rangle$. This is obtained from the following relation:

$$\langle t_i \rangle = \frac{1}{\sum_f \Gamma_{i,f}} \tag{3.7}$$

To summarize, the scattering rates are used to define the occupation probabilities in equilibrium within a given energetic interval as well as the times of flight between scattering events. This completes the dynamics description of the carriers inside the superlattice in equilibrium conditions.

3.4. Carriers under electric field

The electric field has an effect in the carriers that is expressed as changes in their crystal momentum $\mathbf{q}$. This change is expressed in equation 3.8, where e is the electron charge and $\mathbf{E}$ is the electric field. For illustrative purposes, the reader may examine figure 3.3. This is based on the semi-classical approximation:

$$\mathbf{q}_f(t) = \mathbf{q}_i - \frac{e}{\hbar}\mathbf{E}t_i \tag{3.8}$$

It can be seen that the change rate is linear with the TOF and the electric field. The TOF is given by the equation 3.7 and the electric field should satisfy two conditions: i) to be low enough that mobility is an independent quantity of the electric field (ohmic regime) and ii) to be high enough that numerical stability of the gradient calculation in equation 3.2 is guaranteed. It should not matter the particular value since electric mobility is independent of electric field, in the ohmic regime.

With all velocities calculated, it is possible to compute the average velocity for each energetic interval. In order to do this, the probability vector $\hat{\mathbf{P}}$ is used,

as shown in equation 3.9

$$\begin{aligned}\langle \mathbf{v} \rangle_j =& \frac{\langle \Delta \mathbf{R} \rangle}{\langle t \rangle} = \frac{\sum_n \mathbf{v}_n t_n}{\sum_n t_n} = \\ =& \frac{\sum_i N \hat{P}_i \mathrm{v}_i \langle t_i \rangle}{\sum_i N \hat{P}_i \langle t_i \rangle} = \frac{\sum_i \hat{P}_i \mathrm{v}_i \langle t_i \rangle}{\sum_i \hat{P}_i \langle t_i \rangle}\end{aligned} \tag{3.9}$$

In this equation, subindex j indicates the energetic interval, n iterates over all flights within the energetic interval. i, on the other hand, iterates along the initial states. In the Markov chain theory, the number of times the electron starts its flight from state i is equal to the number of total flights N multiplied by the probability for the electron starting its flight at state i. $\langle \Delta \mathbf{R} \rangle$ is the average distance travelled by the electron in a single flight.

3.5. Mobility as a Function of Fermi Level and Temperature

At this stage the calculations have yielded the velocities in each energetic interval as a function of the electric field. We use this information to compute electric mobility in the ohmic regime. Carrier mobility in each energetic interval is a tensor quantity. In order to obtain these tensors (one for each energetic interval) two different directions for the electric field should be simulated. The following relation connecting the carrier velocities with their applied electric field counterparts yields the carrier mobility for the *i-th* energetic interval.

$$\begin{pmatrix} v_1 \\ v_2 \end{pmatrix}_i = \begin{pmatrix} \mu_{11} & \mu_{12} \\ \mu_{21} & \mu_{22} \end{pmatrix}_i \begin{pmatrix} E_1 \\ E_2 \end{pmatrix} \tag{3.10}$$

The subscripts $1, 2$ are the direction of the lattice vectors of the superlattice, subscript i stands for the *i-th* energetic interval, $v_{1,2}$ are the carrier velocity components, $\mu_{l,m}$ are the mobility tensor matrix elements and $E_{1,2}$ represents the electric field.

After using the two electric fields, we have two velocity pairs, from which a mobility matrix can be obtained. After this, the mobility tensor is weighted with the Fermi-Dirac distribution, as shown in the next equation, to account for thermalisation

$$\hat{\mu}(T, E_F) = \frac{\sum_i F(E_i, E_F, T) n_i \hat{\mu}_i}{\sum_i F(E_i, E_F, T) n_i} \tag{3.11}$$

where $F(E_i, E_F, T)$ is the Fermi-Dirac distribution at energy E_i for a given Fermi energy level E_F and at temperature T, and n_i is the number of reciprocal vectors that fall into the *i-th* energetic interval, which is proportional to the density of states.

We deem necessary to remember the reader that by using the Fermi Dirac distribution we are assuming a near equilibrium regime, which means that electric fields should not be too strong in order to fulfil both the equilibrium assumption and the ohmic regime where this model stands.

3.5.1. A simplified picture for the electric carrier velocity dependence with temperature and Fermi level

As seen in equation 3.9, the macroscopic velocity is a result of a sum of velocities in a particular energetic interval. Let us take a pair of states with the same energy but opposite reciprocal space vector and calculate their average velocity. As the two states are exactly the same with the exception of a sign in their reciprocal space location (which is arbitrary since rotating the origin the signs would interchange) we can drop the $\hat{P}_{j,i}$ in our sum and write:

$$\langle v \rangle_p = \frac{v(-\mathbf{q}_p) + v(\mathbf{q}_p)}{2}$$

Where the subscript p stands for a particular pair of states.

We can expand equation 3.2 in terms of a different reciprocal space point.

$$v_f = \frac{1}{\hbar}\,\nabla_q(E)|_{q_f} = \frac{1}{\hbar}\,\frac{\partial E}{\partial q}\bigg|_{q_f} \approx \frac{1}{\hbar}\left(\frac{\partial E}{\partial q}\bigg|_{q_i} + \frac{\partial^2 E}{\partial q^2}\bigg|_{q_i}(q_f - q_i)\right) \tag{3.12}$$

In the equation above, q_i is the reciprocal vector where the carrier starts its flight and q_f the reciprocal vector after scattering happens. Because of the symmetry of the miniband there are relations between the first and second derivatives.

$$\begin{aligned} \frac{\partial E}{\partial q}\bigg|_{q_i} &= -\frac{\partial E}{\partial q}\bigg|_{-q_i} \\ \frac{\partial^2 E}{\partial q^2}\bigg|_{q_i} &= \frac{\partial^2 E}{\partial q^2}\bigg|_{-q_i} \end{aligned} \tag{3.13}$$

To clarify, the states q_i just differ only in sign but the final states q_f can be quite different. Using equation 3.8 we obtain the following relations:

$$\begin{aligned} q_{f1} &= -q_i - \frac{e}{\hbar}\mathbf{E}t_i \\ q_{f2} &= q_i - \frac{e}{\hbar}\mathbf{E}t_i \end{aligned}$$

Both positive and negative q_i have the same summation term therefore they are not symmetric around the origin. Now, if we substitute the expansion 3.12 into our sum of velocities and make use of relations 3.13 we obtain

$$v_f = \frac{1}{\hbar}\,\frac{\partial^2 E}{\partial q^2}\bigg|_{q_i}(q_{f1} + q_{f2})\frac{1}{2} = \frac{-1}{\hbar}\,\frac{\partial^2 E}{\partial q^2}\bigg|_{q_i}\frac{e}{\hbar}\mathbf{E}t_i \tag{3.14}$$

This holds true for every pair of states with symmetric reciprocal points around the origin, which includes all existing states inside all existing energetic intervals. Thus, the average carrier velocity depends on the second derivative of the energetic miniband or, in other words, on the effective mass.

In figure 3.4 we can see the behaviour of different aspects of a typical miniband. We can see a change of the effective mass sign, which means that average velocities in energy intervals above that will have opposite direction to the ones in

energetic regions below it. Thus, the average carrier velocities in the system are governed by the occupation distribution, which in this case is the Fermi distribution that depends heavily on Fermi energy and temperature. If both quantities are low, the average velocity is high since the lowermost part of the miniband is populated. As these two quantities increase, states above the inflection point start to populate, reducing overall carrier velocity.

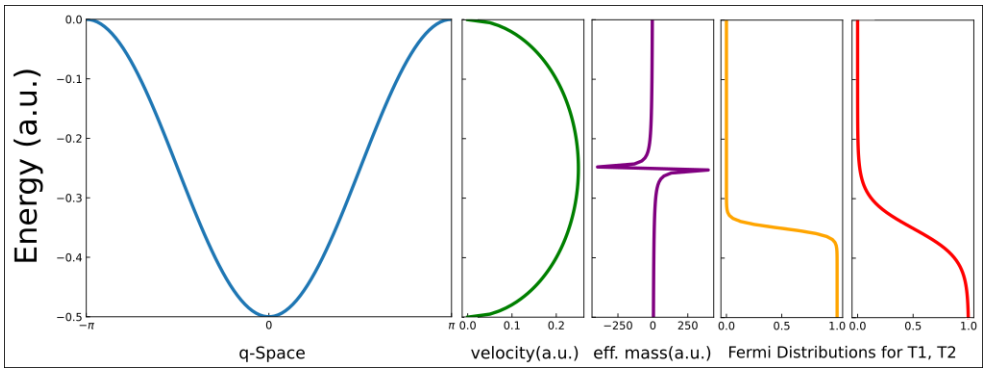

Figure 3.4: Qualitative example of a typical isolated miniband. We showcase the basic behaviour of the important physical quantities. We can observe a change of sign in the effective mass, which governs the direction of the force the electron experiences. For a particular Fermi level, there is a fraction of electrons with energies that make the effective mass negative. If the Fermi level is high enough, this fraction can outgrow the electrons that are below the energetic inflection point and we would observe a change of sign in mobility.

3.6. Various impurities

As shown in [78, 79] in a real scenario there is a continuous QD size distribution profile, usually in the form of a gaussian curve. The model has been reviewed to accommodate to these real situations changing the single impurity QD size for a collection of impurities.

We assume that impurity concentration is low enough so that no interaction between them occurs. This means that the total scattering rate in equation 3.4 changes the integral term to a sum of integrals premultiplied by their correspon-

ding impurity concentration. Thus, equation 3.4 turns into

$$\Gamma_{i,f} = \frac{1}{Q_s}\frac{2\pi}{\hbar}\frac{1}{\Delta E}\frac{1}{\sqrt{K_{cq_i}K_{cq_f}}}\sum_i \nu_i \left|\sum_{m,s} b^*_{cmq_f} b_{csq_i} \int \phi^*_m(\mathbf{r})\Delta V_i(\mathbf{r})\phi_s(\mathbf{r})d\mathbf{r}\right|^2 \tag{3.15}$$

were ν_i and $\Delta V_i(\mathbf{r})$ are the *i-th* non-periodic QD concentration and potential respectively.

Theoretically, the set of concentrations ν_i could be changed by a continuous function, $g_\nu(R_{QD})$ that maps non-periodic QD radius to concentrations. Nevertheless the following has to be considered:

- Not any QD radius is achievable since the minimum addition possible is one atom which increments radius in a discrete quantity.
- It would be too expensive computationally to calculate the overlaps for arbitrarily big sets of QD radii. Nevertheless it is possible to extrapolate scattering rates as an approximated function of QD radius.
- We cannot use an impurity with a radius greater than the periodic QD since this would add tensions to the superlattice and break periodicity.

To model the gaussian size distribution curve we changed the set of concentrations of non-periodic QDs for a single quantity: the standard deviation of the gaussian curve. In figure 3.5 it is shown in a logarithmic plot how our available QD radii decrease their concentrations with a fairly low dispersion.

As the figure shows, following a gaussian curve the concentration of impurities decay so rapidly that QDs with a radius 30 % smaller than the average are irrelevant.

3.6.1. A model for any concentration profile

One of the most important results in this research is a model that allows for a fast mobility calculation not for a single impurity QD, but for a distribution

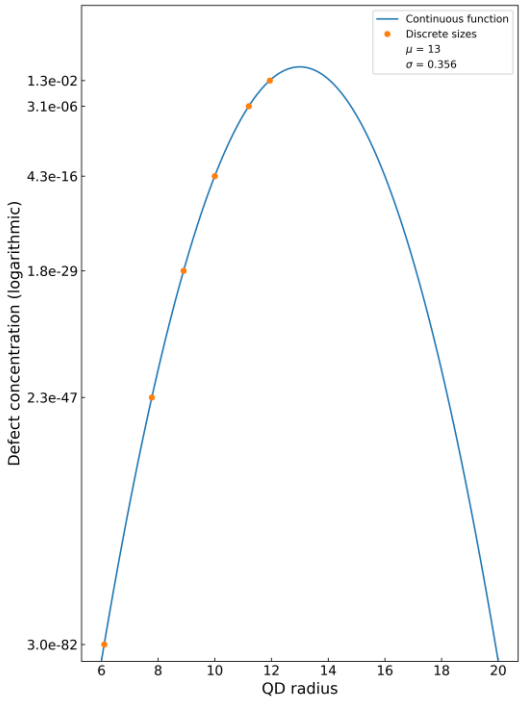

Figure 3.5: Representation of impurities profile used in InAs QDs in our published work [75]. The y axis is logarithmic because the radius decays very pronouncedly as it moves away from the periodic one. Below the second value, concentrations have no observable effects.

of impurities with varying radius[75].

The only approximation made is that, for a given impurity radius, instead of having scattering rates with different values depending on initial and final states, we have an average scattering rate. This is a good approximation since in a particular system, all scattering rates lie in the same order of magnitude. One can observe, in equation 3.4, that the scattering rate is proportional to the impurity concentration. With the above approximation in place, we define the

radius-independent scattering rate as follows.

$$\tilde{\Gamma}^{(r)} = \frac{\left\langle \Gamma_{i,f}^{(r)} \right\rangle}{\nu^{(r)}} \tag{3.16}$$

In this equation we use super index (r) to note that these quantities are for a particular impurity radius. The radius-independent scattering rate is a quantity that depends on the periodic quantum dot, the impurity and the superlattice arrangement and thus is an intrinsic property of the system. This quantity can also be interpreted as the scattering rate in the unphysical situation of an impurity concentration of 100 %.

Mobility is inversely proportional to scattering rate, thus equation 3.11 can be transformed in the following way

$$\begin{aligned} \hat{\mu}^{(r)}(T, E_f) &= \frac{\tilde{\Gamma}^{(r)} \nu \sum_i F(E_i, E_F, T) n_i \hat{\mu}_i}{\tilde{\Gamma}^{(r)} \nu \sum_i F(E_i, E_F, T) n_i} = \\ &= \frac{\hat{\Theta}(E_F, T)}{\tilde{\Gamma}^{(r)} \nu^{(r)}} \end{aligned} \tag{3.17}$$

The quantity $\hat{\Theta}(E_F, T)$ is independent of the impurity concentration, but it is also independent of the concentration independent scattering rate itself, thus depending solely on the miniband structure and the periodic quantum dot. Now it is possible to calculate the mobility for various impurities with the following equation

$$\hat{\mu}^{(r)}(T, E_F) = \frac{\hat{\Theta}(E_F, T)}{\sum_r \tilde{\Gamma}^{(r)} \nu^{(r)}} \tag{3.18}$$

We can now use this equation to obtain any mobility tensor for any concentration provided a non-periodic quantum dot potential or, if we have enough non-periodic QDs we could try to extrapolate their $\hat{\Gamma}^{(r)}$ as in figure 3.6 and use the exact profile for a continuous distribution. We show the results of using these profiles in section 5.4.

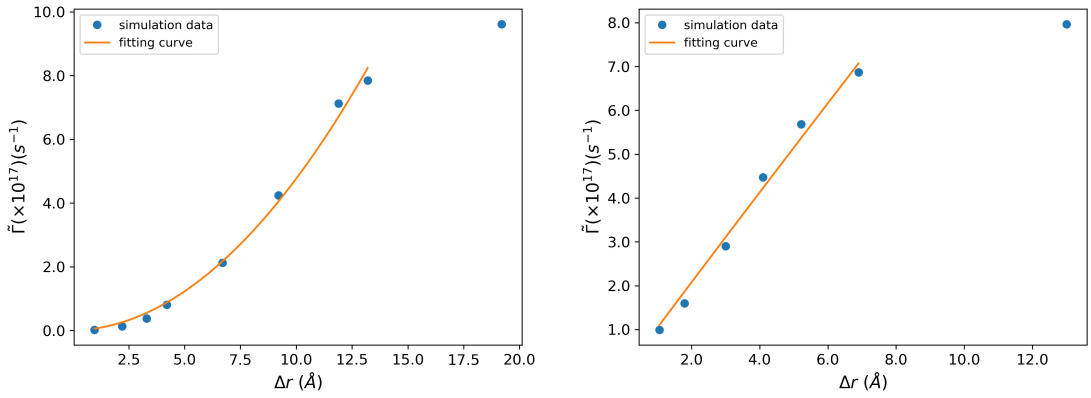

(a) CdSe $\tilde{\Gamma}^{(r)}$ **(b)** InSb $\tilde{\Gamma}^{(r)}$

Figure 3.6: Representation of two different material QD's scattering rates against the difference of periodic and non-periodic radius. It can be seen that different materials yield different curves. Once this curve is interpolated, we can be confident to be able to obtain any scattering rate for any possible QD radius.

4

Absorption coefficient model

4.1. General overview

Quantum dots are a very interesting candidate for tapping solar energy and despite not being among the most prominent technologies in terms of energetic efficiency they are one of the most rapidly advancing in that area[1, 34].

As it has been said in previous chapters, QDs have size-tunable properties and can be cheaply and easily mass produced [2–4, 80] specially in its colloidal form, which are the focus of this work. QD array's characteristics such as bandgap, miniband curvature, absorption spectra or mobility are heavily dependent on the wavefunction overlap. This quantity depends, on one hand, on the isolated quantum dot properties such as size, morphology, chemical composition, surface stoichiometry and on the other hand on device fabrication such as surface passivation, ligand's length, superlattice constant, etc.

Photon absorption (and other macroscopic quantities) are also affected by the superlattice properties, such as interdot separation (superlattice constant) or stacking layers. The photon absorption is also affected by the environment configuration of the device, mainly temperature and Fermi energy level. All these properties are taken into consideration since this chapter is a thorough study of the absorption relationship with all these properties.

There are several strategies for harvesting solar energy using quantum dots, and these can be categorized into three main areas[28, 81]:

• Polymer mixed quantum dots or bulk heterojunction[29, 32, 82] are systems where QDs acting as an electron acceptor (p-type) are blended with an organic polymer acting as electron donor (n-type). This technology has two advantages i) carrier separation happens wherever the photon is absorbed, since donor and acceptor materials are in contact along the entirety of the system. ii) it can be cheaply manufactured, since there is no high ordering required at the microscopic level. Anyway, it has some drawbacks such as high loss in charge transport and the fact that both electron and holes need a percolation path to

the contacts to avoid carrier collection losses [82].

• Quantum dot sensitized solar cell (QDSSC) [14, 83–86]. In a QDSSC quantum dots are sensitizing TiO_2 or semiconductor oxide nanoparticles which are placed in contact with an electrolyte. In these systems the QDs act as the absorbers and transfer their electrons to the semiconductor oxide which in turn transfer them to a transparent contact while the holes are transferred to the electrolyte which in turn transports the carriers to another contact, the counter electrode.

• Ordered arrays[73, 76, 87, 88] There are two other ways in which its possible to harness solar energy with QDs. i) to build a solar cell using QD superlattices. This can be very useful since properties such as band gap can be modulated for n and p type materials independently. ii) the use of quantum dots for intermediate band solar cells (IBSC) [89–91]. This would form a $p-i-n$ structure where n and p materials can be in their bulk form. In these devices the band gap is in the near ultraviolet but is subdivided by an intermediate accessible and narrow energy band formed by the quantum dots. This creates two distinct gaps. If these band gaps are optimized and the rest of Shockley-Queisser assumptions hold, the new efficiency limit could reach 63.2 % [92]. A problem that arises with this bottom-up conversion (in which the strategy to surpass Shockley-Queisser limit is to absorb two photons to create a high energy carrier) is that the electron has to promote from the valence band (VB) to the intermediate band (IB) to be excited once more by another photon to promote to the conduction band (CB). This means that spontaneous emission and phonon emission have to be less relevant than the probability of photon absorption. QDs are advantageous in this area since they present a phonon bottleneck [72] and they have a lower electronic coupling than their atomic lattice counterparts thus phonon scattering or spontaneous emission is less probable to happen.

All the technologies summarized above fall in the third generation photovoltaic cells (PV). All are promising candidates to be the next leap in solar energy tapping. In the present work we focus our attention in the last two mentioned,

those that make use of superlattices: superlattice solar cell and IBSC. This research focuses mainly in the absorption coefficient of these systems since it is a key property in determining quantities such as internal quantum efficiency (IQE) which is a very important feature to assess their commercial viability.

4.2. Absorption definition

The fundamental physical property in this part of our work is the absorption coefficient, α. This physical property describes how much of the incident power per unit area, I_0, is absorbed while travelling through the material. A physical, formal definition for α is

$$\alpha(\hbar\omega) = \frac{R(\hbar\omega)}{N_{ph}(\hbar\omega)} \tag{4.1}$$

where $R(\hbar\omega)$ is the number of absorbed photons per unit of volume and second and $N_{ph}(\hbar\omega)$ is the number of incident photons per unit area and second. The relationship between α and light intensity is the Beer-Lambert law, as shown below[93].

$$I(x) = I_o e^{-\alpha x} \tag{4.2}$$

Where $I(x)$ is the beam light intensity after penetrating a length x below the material's surface.

The absorption coefficient may have different contributions depending on the process involved e.g. optical phonons, trap to band absorptions, free carriers absorptions, etc. We will limit our study to vertical, optical transitions i.e. those in which electric carriers do not change their crystal momentum. These are the transitions responsible for promoting electrons to higher energy minibands allowing them to be harvested by the solar cell contacts and be used for current generation.

4.3. Electromagnetic interaction

Electron interaction with electromagnetic (EM) fields requires to be described in the Hamiltonian. In this case we assumed the semiclassic electromagnetic interaction Hamiltonian shown below[53].

$$H = \frac{(\mathbf{p} - e\mathbf{A})^2}{2m} + e\phi(\mathbf{r}) + V(\mathbf{r}) = \frac{\mathbf{p}^2 - e\mathbf{pA} - e\mathbf{Ap} + e^2\mathbf{A}^2}{2m} + e\phi(\mathbf{r}) + V(\mathbf{r}) \quad (4.3)$$

Where $\mathbf{A}$ is the vector potential, $\phi(\mathbf{r})$ is the electrostatic potential, $V(\mathbf{r})$ is the potential of the system under no illumination conditions and e is the elementary charge. At this point we make use of the following assumptions:

- Coulomb gauge ($\nabla \cdot \mathbf{A} = 0$). This allows momentum operator to commute with the vector potential
- Low intensity field. This allows us to ignore the second order term $e^2\mathbf{A}^2$
- Plane wave in space without charge density. $\phi(r) = C \equiv 0$

Under all these approximations equation 4.3 changes into

$$H = \frac{\mathbf{p}^2}{2m} + V(\mathbf{r}) - \frac{e\mathbf{pA}}{m} \equiv H_0 + H' \quad (4.4)$$

where we defined H_0 as the unperturbed Hamiltonian (this one is solved in chapter 2) and H' as the electromagnetic perturbation.

The illumination is supposed to be harmonic[1] so $\mathbf{A}$ can be expressed as shown below

$$\begin{aligned} \mathbf{A} &= A_0 \cos(\mathbf{k}_{op} \cdot \mathbf{r} - \omega t)\hat{u}_e = \frac{A_0}{2}\left(e^{i(\mathbf{k}_{op}\cdot\mathbf{r}-\omega t)} + e^{-i(\mathbf{k}_{op}\cdot\mathbf{r}-\omega t)}\right)\hat{u}_e \\ &\equiv H'^{\uparrow}e^{-i\omega t} + H'^{\downarrow}e^{i\omega t} \end{aligned} \quad (4.5)$$

[1] At the end of the mathematical derivations we can use any waveform and calculate the absorption by decomposing it in its harmonics and computing the absorption of each one.

Where $\mathbf{k}_{op}$ is the photon electromagnetic wave number, ω the angular frequency, $H'^{\uparrow}$ and $H'^{\downarrow}$ are operators for absorption and emission respectively (they are complex conjugates) and $\hat{u}_e$ is the unit vector of the potential direction, which coincides with the light polarization direction.

4.4. Fermi's Golden Rule for EM interaction

Given an initial superlattice eigenstate $\psi_i(\mathbf{r})$ with energy E_i and final eigenstate $\psi_f(\mathbf{r})$ with energy E_f and the perturbation Hamiltonian from equation 4.4, the Fermi's Golden Rule [53] is expressed as follows[2]

$$\begin{aligned}\Gamma_{i,f} &= \frac{2\pi}{\hbar}\left|\left\langle\psi_f\left|H'^{\uparrow}\right|\psi_i\right\rangle\right|^2\delta(E_f-(Ei+\hbar\omega)) \\ &+ \frac{2\pi}{\hbar}\sum_f\left|\left\langle\psi_f\left|H'^{\downarrow}\right|\psi_i\right\rangle\right|^2\delta(E_f-(Ei-\hbar\omega)) \\ &= W_{i,f}^{\uparrow}+W_{i,f}^{\downarrow}\end{aligned} \tag{4.6}$$

The time dependency of $H'^{\uparrow}$ has become the energy conservation condition as it happens with harmonic perturbations in the Fermi Golden Rule [53]. We had performed several operations over the brackets above. From now on we show only the absorption process, $W^{\uparrow}$.

$$\left\langle\psi_f|H'^{\uparrow}|\psi_i\right\rangle = \frac{eA_0}{2m}\left\langle\psi_f\left|\hat{u}_e\cdot e^{i\mathbf{k}_{op}\mathbf{r}}\mathbf{p}\right|\psi_i\right\rangle \approx \frac{eA_0}{2m}\left\langle\psi_f\left|\hat{u}_e\cdot\mathbf{p}\right|\psi_i\right\rangle \tag{4.7}$$

The above approximation is the electric dipole approximation[94], which assumes that the light wavelength is much larger than the electric carrier one, $\mathbf{q}_i, \mathbf{q}_f \gg \mathbf{k}_{op}$.

At this step we use the Hamiltonian and momentum commutator.

$$\mathbf{p} = \frac{im}{\hbar}[H,\mathbf{r}] \tag{4.8}$$

[2]We have omitted $\mathbf{q}$ in $\psi_{m,\mathbf{q}}$ for notation simplification.

Substitution in equation 4.7 yields

$$\begin{aligned} & \frac{eA_0}{2m}\frac{im}{\hbar}\hat{u}_e\left[\langle\psi_f|H\mathbf{r}|\psi_i\rangle + \langle\psi_f|\mathbf{r}H|\psi_i\rangle\right] \\ = \quad & \frac{eA_0 i}{2\hbar}(E_f - E_i)\hat{u}_e\langle\psi_f|\mathbf{r}|\psi_i\rangle \end{aligned} \tag{4.9}$$

In order to calculate $\langle\psi_f|\mathbf{r}|\psi_i\rangle$, and assuming that the Bloch wave has a wavelength that is much larger than the lattice vector we make use of the slowly varying envelope approximation. We will carry out a change of variable, $\mathbf{r}' \equiv \mathbf{r} - \mathbf{R}$, with the purpose of referring to all the integrals to the same reference cell, and express superlattice eigenstates as Bloch functions.

$$\begin{aligned} & \frac{1}{N}\int_{\infty} U^*_{f,q_f}(\mathbf{r})e^{-i\mathbf{q}_f\cdot\mathbf{r}}\mathbf{r}U_{i,q_i}(\mathbf{r})e^{i\mathbf{q}_i\cdot\mathbf{r}}dr^3 = \\ = & \frac{1}{N}\sum_{R_n}\int_{\Omega_{R_n}} U^*_{f,q_f}(\mathbf{r})\mathbf{r}U_{i,q_i}(\mathbf{r})e^{i(\mathbf{q}_i-\mathbf{q}_f)\cdot\mathbf{r}}dr^3 \approx \\ & \qquad \boxed{\mathbf{r}' \equiv \mathbf{r} - \mathbf{R}_n} \\ \approx & \frac{1}{N}\sum_{R_n} e^{i(q_i-q_f)\cdot\mathbf{R}_n}\int_{\Omega_{R_0}} U^*_{f,q_f}(\mathbf{r}'+\mathbf{R}_n)(\mathbf{r}'+\mathbf{R}_n)U_{i,q_i}(\mathbf{r}'+\mathbf{R}_n)dr'^3 = \\ & \qquad \boxed{U(\mathbf{r}'+\mathbf{R}) = U(\mathbf{r})} \\ = & \frac{1}{N}\sum_{R_n} e^{i(q_i-q_f)\cdot\mathbf{R}_n}\left\{\int_{\Omega_{R_0}} U^*_{f,q_f}(\mathbf{r}')\mathbf{r}'U_{i,q_i}(\mathbf{r}')dr'^3 + \right. \\ & \left. +\mathbf{R}_n\int_{\Omega_{R_0}} U^*_{f,q_f}(\mathbf{r}')U_{i,q_i}(\mathbf{r}')dr'^3\right\} = \\ = & \int_{\Omega} U^*_{f,q_f}(\mathbf{r})\mathbf{r}U_{i,q_i}(\mathbf{r})dr^3\delta(\mathbf{q}_i-\mathbf{q}_f) + \frac{1}{N}\sum_{\mathbf{R}_n}\mathbf{R}_n e^{i(\mathbf{q}_i-\mathbf{q}_f)\mathbf{R}}\int_{\Omega} U^*_{f,q_f}(\mathbf{r})U_{i,q_i}(\mathbf{r})dr^3 \\ = & \int_{\Omega} U^*_{f,q}(\mathbf{r})\mathbf{r}U_{i,q}(\mathbf{r})dr^3 + \frac{1}{N}\sum_{\mathbf{R}_n}\mathbf{R}_n e^{i(\mathbf{q}_i-\mathbf{q}_f)\mathbf{R}_n}\left\langle U_{f,q_f}|U_{i,q_i}\right\rangle_{\Omega} \end{aligned} \tag{4.10}$$

Where N is the number of unit cells in the system (virtually infinite) and Ω is the unit cell volume. We have omitted $\delta(\mathbf{q}_i - \mathbf{q}_f)$ by changing subscripts q_i, q_f by q in the Bloch functions that multiply the Dirac delta. There are two

terms in the solution. A priori, the second one seems to vanish when N tends to infinity because of orthogonality reasons when $\mathbf{q}_i = \mathbf{q}_f$ thus, it will not affect in a periodic system. We will come back to this summation term later in the chapter to discuss it in detail.

It can be seen that all the calculations done for the absorption operator would yield the same results if we repeat calculations for the emission operator, since the only difference between them is the wave number sign, which vanishes anyway with the dipole approximation.

With all these approximations we can now rewrite the Fermi's Golden Rule to calculate the rate at which an electron occupying a particular state ψ_i will promote to an unoccupied state ψ_f when the system is radiated with an harmonic electromagnetic radiation with angular frequency ω such that $E_f - E_i = \pm\hbar\omega$

$$\begin{aligned}\Gamma_{i,f}(\omega) &= \frac{2\pi}{\hbar}\left|\frac{eA_0 i}{2\hbar}(E_f - E_i)\hat{u}_e \cdot \int_\Omega U^*_{f,q}(\mathbf{r})\mathbf{r}U_{i,q}(\mathbf{r})dr^3\right|^2 \delta(E_f - (E_i + \hbar\omega)) \\ &= \frac{\pi}{2\hbar}\left(eA_0\omega\right)^2\left|\hat{u}_e \cdot \int_\Omega U^*_{f,q}(\mathbf{r})\mathbf{r}U_{i,q}(\mathbf{r})dr^3\right|^2 \delta(E_f - (E_i + \hbar\omega)) \quad (4.11)\end{aligned}$$

A property of equation 4.11 is that $\Gamma_{i,f} = \Gamma_{f,i}$ which means that this quantity is the same regardless if the process is an emission or an absorption. It is an absorption process when $E_i < E_f$ and an emission process in the other case.

4.5. Absorption per unit volume and absorption coefficient

The total upward transition rate per unit of volume in the crystal, i.e. a quantity related with the transition probability from an initial state with energy E_i to a final state with energy E_f, $E_f > E_i$, is a quantity that accounts not only the transition probabilities of equation 4.11, but also the occupation probability

of the initial state and the inoccupation probability of the final state. Similarly, the total downward transition rates per unit of volume in the crystal is related to transitions where $E_f < E_i$, considering again the probabilities of equation 4.11 and the occupation and inoccupation probabilities of the initial and final states respectively. The occupation probabilities in the superlattice in equilibrium are given by the Fermi-Dirac statistics. Adding both, the upward and the downward transition rates per unit of volume, we define the net upward transition rate per unit of volume, $R_{i,f}(\hbar\omega)$, that can be written as:

$$\begin{aligned} R_{i,j}(\hbar\omega) &= \frac{1}{V}\sum_{i,f;E_i<E_f} \\ &\quad \Gamma_{i,f}F(E_i,T)(1-F(E_f,T))\delta(E_f-(E_i+\hbar\omega)) - \\ &- \Gamma_{f,i}F(E_f,T)(1-F(E_i,T))\delta(E_f-(E_i-\hbar\omega)) \\ &= \frac{1}{V}\sum_{i,f;E_i<E_f}\Gamma_{i,f}\{F(E_i,T)-F(E_f,T)\}\delta(E_f-(E_i+\hbar\omega)) \end{aligned} \tag{4.12}$$

Here V is the volume of the whole system.

Finally, the number of incident photons with a given energy per unit area and unit time N_{ph} inside the material can be expressed as the energy per unit time per unit area (Poynting vector) divided by the photon energy

$$N_{ph} = \frac{\langle S\rangle}{\hbar\omega} = \frac{n_r c\epsilon_o \omega A_0^2}{2\hbar} \tag{4.13}$$

Where n_r is the relative refractive index, c the speed of light, ϵ_0 is the vacuum dielectric permittivity.

Finally, the absorption coefficient α from equation 4.1 can be expressed

$$\alpha(\hbar\omega) = \frac{\pi e^2\omega}{n_r c\epsilon_0 V}\sum_{\{i,f\}:E_i<E_f}\left|\hat{u}_e\cdot\int_\Omega U^*_{f,q}(\mathbf{r})\mathbf{r}U_{i,q}(\mathbf{r})dr^3\right|^2\{F(E_i,T)-F(E_f,T)\}\delta(E_f-(E_i+\hbar\omega)) \tag{4.14}$$

4.6. Computing the absorption coefficient

Due to the virtually infinite amount of reciprocal space points $\mathbf{q}$ that are in a real system, we choose to sample the reciprocal space with a regular grid, as we did in the tight binding calculation. We made a discretization that reduces this infinite quantity of reciprocal states to a finite one, with Q_S states. This sampling introduces a new factor in equation 4.14, $\frac{N}{Q_S}$. This factor ensures that all the real reciprocal vectors are represented in the limited amount of points in the discrete sampling.

Another concept worth mentioning is the computational strategy to ensure energy conservation. Instead of sweeping in photon energy and looking for any pair of states that happen to have that exact energetic difference, we take the opposite direction: we examine each pair of states (provided their reciprocal state is equal, so momentum conservation is ensured) and calculate equation 4.14. We then associate that absorption coefficient to the energetic difference of the two states involved.

To clarify the calculation we write the integral in terms of the tight binding coefficient expansion. Recalling equation 2.8 and 2.6, we have that

$$\begin{aligned} \psi_{m,q}(\mathbf{r}) &= \frac{1}{\sqrt{K_{m,q}N}} \sum_{n,\mathbf{R}_n} b_{m,q,n} e^{i\mathbf{q}\cdot\mathbf{R}_n} \phi_n(\mathbf{r}-\mathbf{R}_n) \\ &= \frac{1}{\sqrt{N}} U_{m,q}(\mathbf{r}) e^{i\mathbf{q}\cdot\mathbf{r}} \end{aligned} \tag{4.15}$$

Thus, the term $U_{m,q}$ can be rewritten as

$$U_{m,q}(\mathbf{r}) = \frac{e^{-i\mathbf{q}\cdot\mathbf{r}}}{\sqrt{K_{m,q}}} \sum_{n,\mathbf{R}_n} b_{m,q,n} e^{i\mathbf{q}\cdot\mathbf{R}_n} \phi_n(\mathbf{r}-\mathbf{R}_n) \tag{4.16}$$

Therefore the integral of equation 4.14 can be rewritten as

$$\int_{\Omega} U^*_{f,q}(\mathbf{r})\mathbf{r}U_{i,q}(\mathbf{r})dr^3 = \tag{4.17}$$
$$= \frac{1}{\sqrt{K^*_{f,q}K_{i,q}}} \sum_{n,\mathbf{R}_n} \sum_{n'\mathbf{R}'_n} b^*_{f,q,n} b_{i,q,n'} e^{i\mathbf{q}\cdot(\mathbf{R}'_n - \mathbf{R}_n)} \int_{\Omega} \phi^*_n(\mathbf{r}-\mathbf{R}_n)\phi_{n'}(\mathbf{r}-\mathbf{R}'_n)dr^3$$

We point out that in this equation the term $e^{i(\mathbf{q}_f - \mathbf{q}_i)\cdot\mathbf{r}}$ has vanished because $\mathbf{q}_i = \mathbf{q}_f$ due to the vertical optical transitions.

In the same manner we calculated the integrals in equation 2.11, it is feasible to neglect all the integrals except the ones concerning first neighbors and the ones for the considered quantum dot. Defining $\mathbf{R}_p = \mathbf{R}'_n - \mathbf{R}_n$, for a given $\mathbf{R}'_n$ only $\mathbf{R}_p = 0$ and $\mathbf{R}_p$ for nearest vectors are not dropped from the summation.

$$\int_{\Omega} U^*_{f,q}(\mathbf{r})\mathbf{r}U_{i,q}(\mathbf{r})dr^3 = \tag{4.18}$$
$$= \frac{1}{\sqrt{K^*_{f,q}K_{i,q}}} \sum_{n,n',\mathbf{R}_p} b^*_{f,q,n} b_{i,q,n'} e^{i\mathbf{q}\mathbf{R}_p} \int_{\Omega} \phi^*_n(\mathbf{r}-\mathbf{R}_p)\mathbf{r}\phi_{n'}(\mathbf{r})dr^3$$

When we substitute equation 4.18 into the absorption coefficient 4.14 we obtain our final expression for the coefficient.

$$\alpha(\hbar\omega) = \frac{\pi e^2 \omega}{Q_s n_r c \epsilon_0 \Omega} \sum_{\{i,f\}:E_i<E_f} \left| \sum_{n,n',\mathbf{R}_p} \frac{b^*_{f,q_f,n} b_{i,q_i,n'} e^{i\mathbf{q}\mathbf{R}_p}}{\sqrt{K^*_{f,q}K_{i,q}}} \times \ldots \right. \tag{4.19}$$
$$\left. \cdots \times \hat{u}_e \cdot \int_{\Omega} \phi^*_f(\mathbf{r}-\mathbf{R}_p)\mathbf{r}\phi(\mathbf{r})dr^3 \right|^2 \{F(E_i,T) - F(E_f,T)\}\delta(E_f - (E_i + \hbar\omega))$$

We note that V, the system's total volume, disappears in the equation and Ω, the unit cell volume, replaces it. This is because of the $\frac{N}{Q_s}$ factor that relates the

real reciprocal space (N points) and our sampling (Q_s points) of the reciprocal space.

So far, with equation 4.19 we are able to compute the absorption for all photons whose energy is equal to the energy differences from miniband to miniband, between states with the same $\mathbf{q}$ vector. This calculation consists on computing a histogram. Once we calculate the absorption coefficient for all energetic differences available in the system we use bins of a certain width and represent the resulting curve. The final result depends on the Q_s discretization and the bin width. The less granular the Brillouin zone sampling, the more accurate the calculation. The narrower the bin width, the noisier the absorption coefficient curve. Therefore, a compromise for Q_s and the bin width should be considered for a proper calculation.

4.7. Considerations on finite systems

One of the most striking aspects of this work is the unexpected results when computing the absorption coefficient in finite systems. An example is shown in figure 4.1, where we calculate the absorption for a 2D periodic stack of 10 QDs.

We can notice a very high absorption peak at very low energies when light is polarized along the stack direction[3] i.e. $\hat{z}$. This low energy peak is an order of magnitude higher than the other peaks of the absorption curve which, as the inset shows, are of similar magnitude as those corresponding to the $\hat{x}$ polarization. This peak is non-existent in 2D periodic superlattices.

In figure 4.1 the Fermi level is at the conduction band edge (only conduction bands are present) and temperature was 77K thus the population is highly concentrated in the lowermost energetic states of the system. The photon energy corresponding to the low energy absorption peaks could be inferred from figure

[3]All the stacked systems in this work are stacked along the $\hat{z}$ direction and the periodicity is along $\hat{x}$ and $\hat{y}$ directions.

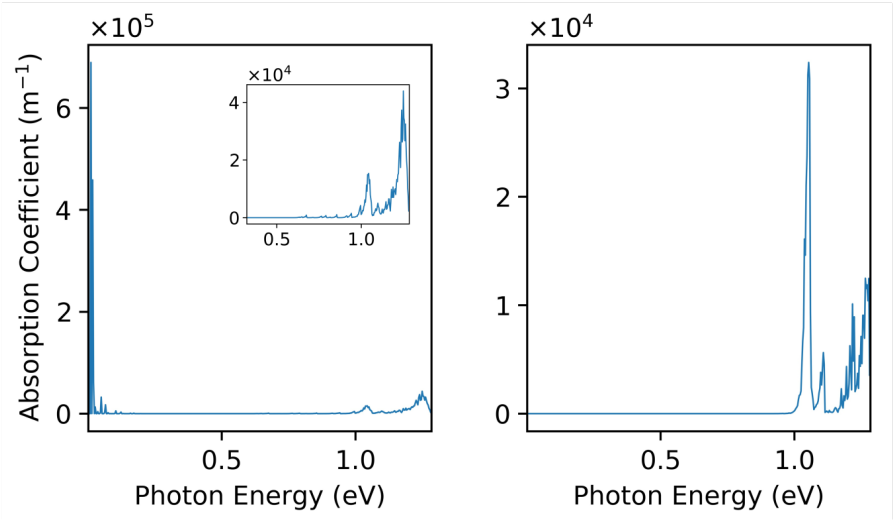

Figure 4.1: Absorption calculations for a 2D periodic stack of 10 QDs. Light polarized along the $\hat{z}$ direction with an inset showing the same curve, cropped to hide the low energy peak (left panel) and absorption curve for light polarized along the $\hat{x}$ direction (right panel).

4.2, corresponding to vertical transitions between the group of lowest energy minibands (the ones originated from the lowest energy miniband in the 2D periodic lattice without stacking).

In the case of a regular 3D periodic superlattice (i.e. physical limit of an infinite 2D stack) this group of bands would turn into a continuum, that would form the energetic band along $\hat{z}$ axis. In that case, there would not be any low peak absorption, since that would violate the momentum conservation, yet it is happening in this case where the stacking along $\hat{z}$ axis is finite. This inspired us to investigate if the conservation of momentum has the same mathematical interpretation when there is a finite system and thus not a proper reciprocal lattice can be established.

To improve our understanding of this effect, we studied 1D systems. Our 1D

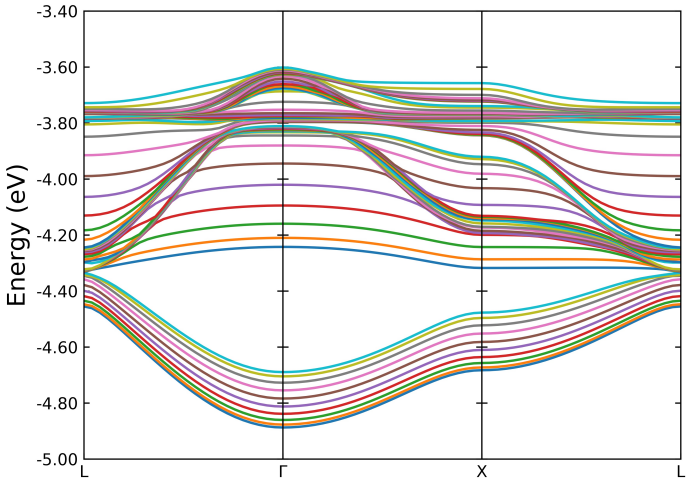

Figure 4.2: Miniband structure of the 10 stacked InAs R=12Å two-dimensional quantum dot array.

study can be divided into two essentially different types of systems: the finite (QD molecules) and the infinite ones (periodic systems).

Figure 4.3 shows the energies of some systems to compare. The figure shows the energy of three finite systems versus the 1D periodic one. It can be seen that in all cases the molecular states are within the width of the periodic system minibands.

We also found an interesting correspondence shown in the figure 4.4 suggesting that there is some relationship between finite and periodic systems. There is an excellent correlation when plotting the **q** vectors of the miniband states whose energy is equal to the molecule ones. This suggests that the molecular states have a relation with the periodic states with particular **q** vectors.

With this context let us now analyse the second term in the last expression

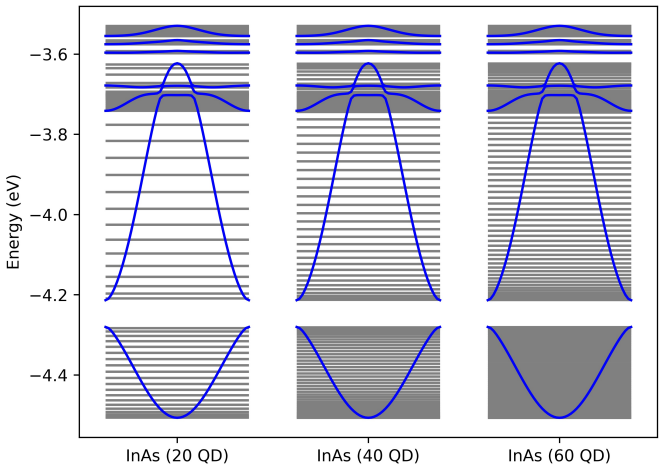

Figure 4.3: Comparison of the 1D InAs R=12Å periodic system minibands (blue lines) and the energy spectra of 20, 40 and 60 R=12Å QD molecules.

of equation 4.10 to gain insight on the complete behaviour of energy absorption.

$$\frac{1}{N}\sum_{\mathbf{R}_n}\mathbf{R}_n e^{i(\mathbf{q}_i-\mathbf{q}_f)\cdot\mathbf{R}_n}\left\langle U_{f,q_f}|U_{i,q_i}\right\rangle \tag{4.20}$$

For now we can omit the bracket, since it can be factored out of the summation and make some changes to facilitate our calculations. Firstly we define the reciprocal vector distance $\boldsymbol{\xi} = \mathbf{q}_i - \mathbf{q}_f$. Secondly, we redefine $\mathbf{R}_n = l_{cu} n \hat{u}_z$ where n is the *n-th* superlattice position and l_{cu} is the unit cell length. We can relate this expression to the geometric series as shown below

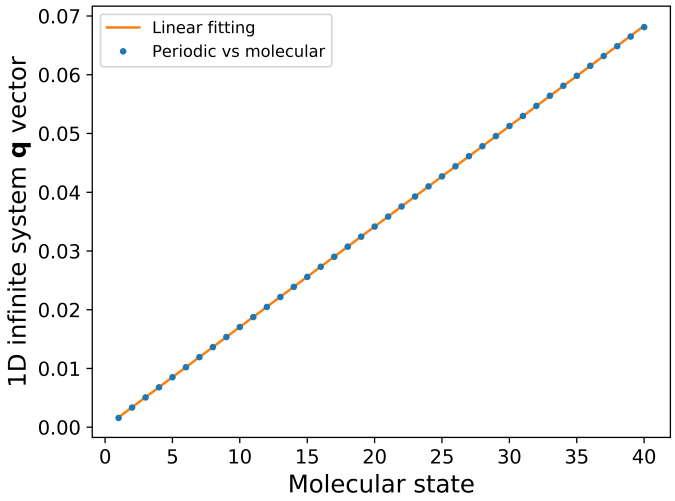

Figure 4.4: Plotting of **q** vector whose energy coincides with the *i-th* molecular state. We used the first 40 molecular states of a 40 QDs molecule and compared them with the first miniband. The slope is $7.7032 \times 10^{-2} \simeq \dfrac{1}{N+1}$

$$
\begin{aligned}
\frac{1}{N}\sum_{n=-(N-1)/2}^{(N-1)/2} l_{cu} n e^{i\boldsymbol{\xi} l_{cu} n} &= -\frac{i}{N}\frac{\partial}{\partial \boldsymbol{\xi}} \sum_{n=-(N-1)/2}^{(N-1)/2} e^{i\boldsymbol{\xi} l_{cu} n} = \\
&= -\frac{i}{N}\frac{\partial}{\partial \boldsymbol{\xi}} e^{-\frac{i\boldsymbol{\xi}(N-1)l_{cu}}{2}} \sum_{n=0}^{N-1} e^{i\boldsymbol{\xi} l_{cu} n} = -\frac{i}{N}\frac{\partial}{\partial \boldsymbol{\xi}} \frac{1-e^{i\boldsymbol{\xi} N l_{cu}}}{1-e^{\frac{i\boldsymbol{\xi} l_{cu}}{2}}} e^{-\frac{i\boldsymbol{\xi}(N-1)l_{cu}}{2}} = \\
&= -\frac{i}{N}\frac{\partial}{\partial \boldsymbol{\xi}} \frac{\sin\left(\dfrac{\boldsymbol{\xi} l_{cu} N}{2}\right)}{\sin\left(\dfrac{\boldsymbol{\xi} l_{cu}}{2}\right)} \equiv -\frac{i}{N}\frac{\partial}{\partial \boldsymbol{\xi}} F(\boldsymbol{\xi}) = \\
&= -\frac{F(\boldsymbol{\xi})}{N}\left\{\frac{l_{cu}N}{2}\cot\left(\frac{\boldsymbol{\xi} l_{cu} N}{2}\right) - \frac{l_{cu}}{2}\cot\left(\frac{\boldsymbol{\xi} l_{cu}}{2}\right)\right\} \equiv G(\boldsymbol{\xi})
\end{aligned}
\tag{4.21}
$$

To understand the functions $F(\boldsymbol{\xi})$ and $G(\boldsymbol{\xi})$ we have plotted them in figure 4.5 for different values of N. We can see that as N grows the function $G(\boldsymbol{\xi})$ tends

to behave as the Dirac delta, $\delta(\boldsymbol{\xi})$, while the function $G(\boldsymbol{\xi})$ tends to the Dirac delta derivative.

In agreement with previously presented results, these functions show that in the limit of large N, i.e. a periodic system, the absorption coefficient will peak at very low energies.

There is a reason why these low energy peaks do not show in the 2D periodic systems with no stacking. While the summation of equation 4.21 is non-zero, the bracket $\langle U_{f,q_f} | U_{i,q_i} \rangle$ is equal to zero whenever $i = f$ i.e. the transition occurs between states in the same miniband. Thus, the only transitions that are possible given the usual Fermi energy levels are those from photons with energy grater than the band gap. There is a thorough discussion on section 5.6.2 about how absorption is affected when using 2D periodic stacks.

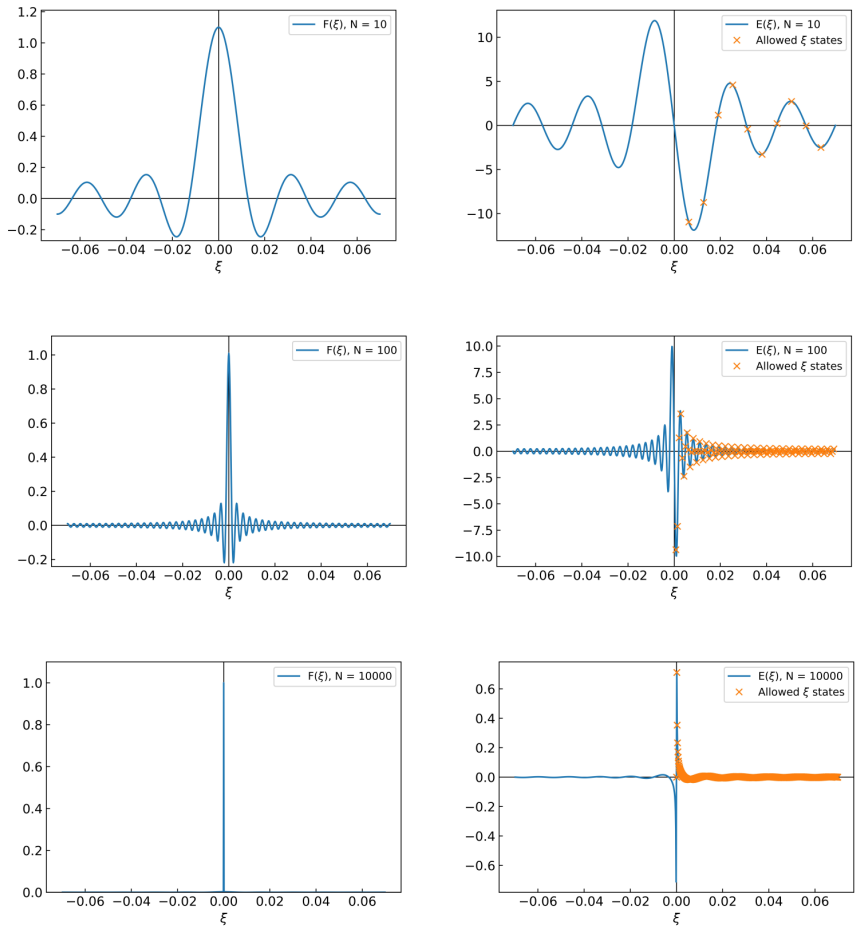

Figure 4.5: $F(\boldsymbol{\xi})$ and $G(\boldsymbol{\xi})$ against different values of $\boldsymbol{\xi}$. It can be seen that for low values of N the term in equation 4.21 is non-zero for values of $\boldsymbol{\xi}$ different than zero, which means that for small molecules the crystal momentum conservation is not exactly fulfilled. The orange crosses indicates the allowed $\boldsymbol{\xi}$ for a molecule of N quantum dots. To simplify our analysis the allowed $\boldsymbol{\xi}$ have been calculated using figure 4.4 with $q_i = 0$. When N tends to infinite $G(\boldsymbol{\xi})$ tends to an infinitely peaked function, with peaks infinitely close to zero. Thus, transitions that do not exactly conserve momentum are still allowed, but at infinitesimal photon energies

5

Results

5.1. Results outline

We have divided our results by published articles [65, 75, 76, 87], in chronological order of publication. These articles, along with the unpublished work, represent the overall results produced during this thesis.

5.2. Nanoscale, 10 20 9679-9690 (2018)

In this article we calculated the electron mobility dependence with temperature for 2D periodic superlattices for four different CdSe quantum dots. These are two wurtzite CdSe of 1.84 nm and 1.26 nm radius forming an hexagonal superlattice and two having zincblende crystal structure with 1.22 nm radius and opposite stoichiometry, Se and Cd rich surfaces, forming a square superlattice. We also analysed the simulator for numerical stability and obtained useful insights and predictions for experimentalists who wish to synthesize these types of QDs.

In figure 5.1 we show a 3D representation of the 1.84 nm wurtzite QD. It can be seen that the 2D superlattice is hexagonal in this case.

5.2.1. Introduction and numerical stability analysis

Before publishing our mobility results we wanted to analyse the numerical stability of the simulation, specifically the numerical solutions for equation 3.2. These are very important, since the material is deemed to be ohmic, thus its mobility has to be independent of the electric field strength. Equation 3.2 has an implicit fraction, expressed as a gradient. In a simplified picture of this calculation, we have a variation in energy divided by a variation in superlattice crystal momentum. The change in superlattice crystal momentum $\mathbf{q}$ is given by equation 3.8 which depends on the electric field. The variation in energy also depends indirectly on the variation of the crystal momentum. Thus, if the electric field is very low the gradient is essentially the result of a fraction of two very small values. Computations like this one can be very noisy because of the

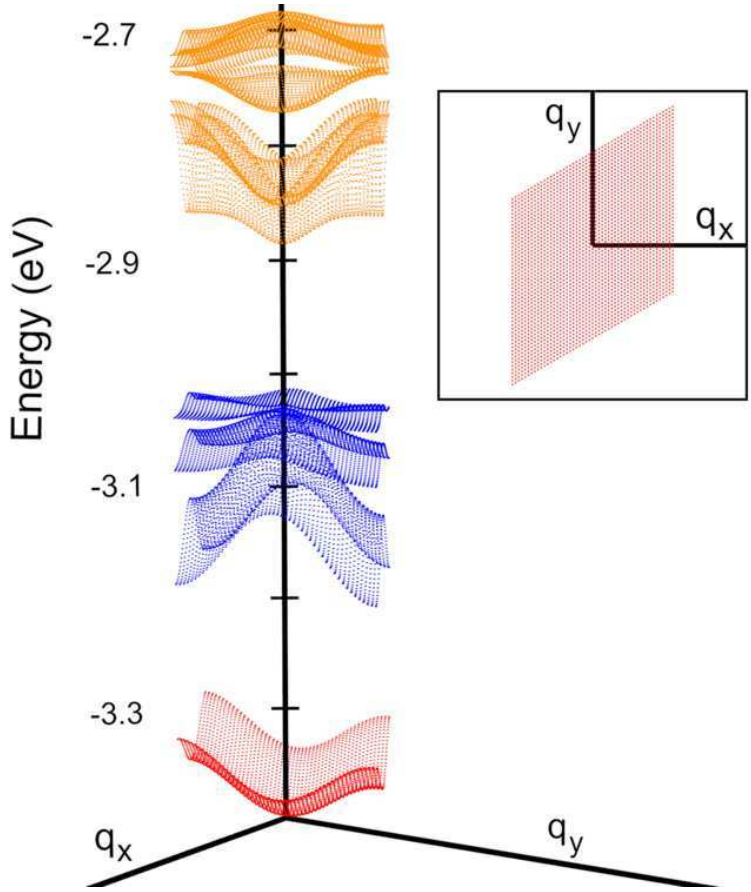

Figure 5.1: 3D representation of wurtzite CdSe 1.84 nm quantum dot minibands derived from the conduction band states.

limited numerical resolution of computers. On the other hand, if the electric field is too high, the change in crystal momentum would break the ohmic regime assumptions.

By representing electronic mobility with varying electric fields we found a plateau as shown in figure 5.2. Thus we chose 100 V/m as our electric field intensity since around this value electric mobility is kept constant.

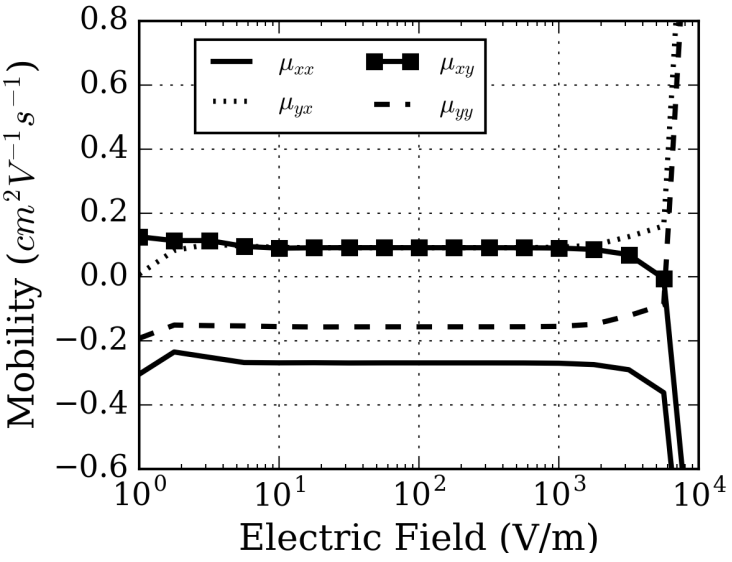

Figure 5.2: Mobility eigenvalues of the first energetic interval of the miniband as a function of electric field intensity. It can be seen that the simulation shows the expected ohmic behaviour one order of magnitude around 100V/m.

Another interesting aspect to assess was the noisiness of the mobility versus the energetic interval curve. We found in equation 3.11 that this value depends strongly on the number of states per energetic interval n_i. This value is very fluctuating from one energetic interval to the other, which could be due to a poor Brillouin zone discretization, that do not distribute smoothly the reciprocal space sampling between energetic intervals. This is important because it can introduce a mobility dependence with reciprocal space discretization, which would not have physical meaning. This could be solved by using a less coarse discretization, but that would increment the algorithmic time complexity resulting in large simulation times. We chose another strategy. We used a thinner discretization but instead of using it to calculate the mobility we used it only to obtain a more precise DOS and as a result better n_i values which do not depend on the discretization used to make the calculations. Figure 5.3 shows two mobility eigenvalues as a function of energy without density of states correction (black diamonds) and

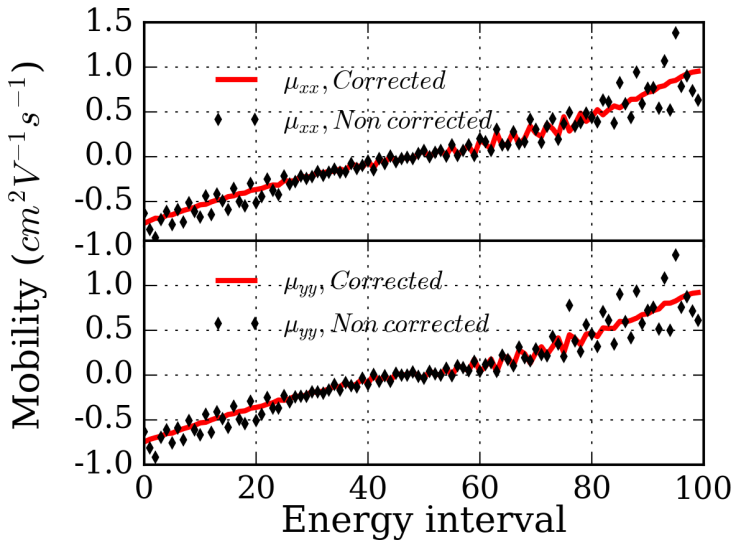

Figure 5.3: Comparison of mobilities with and without correction. We premultiply each n_i in equation 3.11 by $\frac{n_i'}{n_i}\frac{Qs}{Qs'}$ where n_i' and Q_s' are the number of states per energetic interval and total reciprocal space vectors of a less coarse discretization, respectively.

the same calculation with the corrected DOS (red lines). This correction affects mostly to the edges of the miniband. This is specially important since we usually choose the Fermi level to be on the lower edge of the lowest energy miniband (in this work the minibands are all above the bulk bandgap) so the first energetic intervals are the most important to the mobility values.

There are four quantities affecting the superlattice that are important to study i.e. Fermi level, temperature, superlattice constant and impurity concentration. In this paper we studied the four of them and proposed compact models to extend our calculations beyond the simulation.

5.2.2. Mobility as a function of Fermi level

In figure 5.4 we show the mobility dependence with temperature and Fermi level for the wurtzite CdSe with 1.84 nm radius in a superlattice with minimum

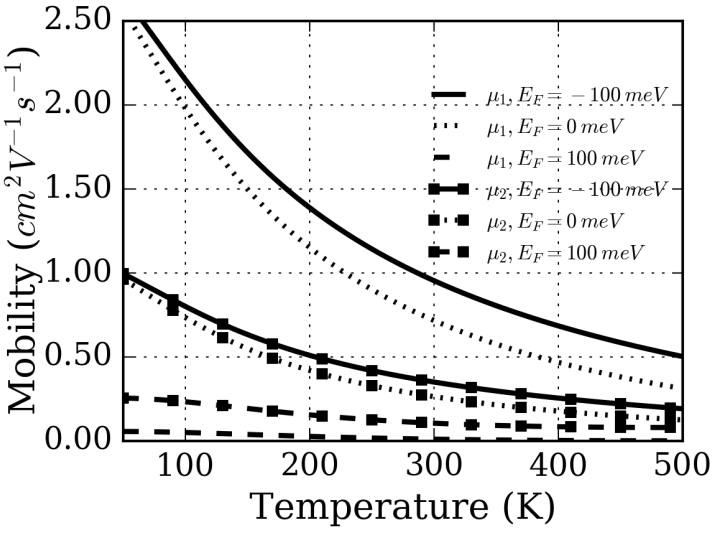

Figure 5.4: Electronic mobility as a function of temperature for different Fermi levels.

lattice constant. QDs are one bond length (1 bl) apart from one another. It is noticeable that Fermi level affects mobility dramatically as long as it is not below the miniband minimum by a large margin. We were not interested in analysing very high Fermi levels since that configuration would be difficult to produce in an experimental setting. As the Fermi level is lowered below the miniband minima, the Fermi statistics tend to the Boltzmann distribution and mobility becomes independent of the Fermi level position. We chose the latter scenario, with a Fermi level 1.5 eV below the lowest energy miniband minimum, in the CdSe bandgap (5 eV below vacuum level).

5.2.3. Mobility as a function of the superlattice constant

Figures 5.5 and 5.6 show the mobility as a function of temperature for the two wurtzite crystalline structure QDs for different superlattice constants. It can be seen in both figures that the mobility is abruptly reduced as the superlattice constant grows. This is due to the exponential decay of the strongly confining nature of the quantum dot which makes wavefunction overlaps to

change strongly with dot-to-dot separation. The distance between the QDs' walls are ranging between 1 and 2 bond lengths, which is achievable experimentally [3], and the mobility changes in three orders of magnitude. This also happens because in our simulations the quantum dot is surrounded by vacuum. In the real case, quantum dots would be surrounded by ligands providing coupling for varying distances. Thus, our mobility calculations are a worst case scenario.

We also observe the different mobility eigenvalues between the 1.84 nm QD radius and the smaller 1.26 nm radius one. In figure 5.7 we can see why. The figure represents both systems' minibands at a particular energetic interval, 5 meV above the miniband minima. It can be seen that the bigger quantum dot shows a clear miniband anisotropy while the smaller is isotropic. This is another example of the size dependent properties of quantum dots. The smaller QD superlattice shows higher mobility. This seems to be a rule of thumb for quantum dots: the overlap between QDs tends to grow with decreasing quantum dot radius, and as a consequence the carrier mobility increases.

In the case of CdSe 1.84 nm radius quantum dots we chose the impurity quantum dot to be 1.7nm radius in 1 % concentration (one in a hundred are impurities in the superlattice) which corresponds to a size dispersion of about 7 %. In the case of CdSe 1.26 nm quantum dots, the chosen impurity is of 1.1 nm radius, which, when it is in 1 % concentration, represents a size distribution of 10.4 %.

We also simulated the two zincblenda CdSe QDs with a Cd and a Se rich surface, both in square superlattices. In figures 5.8 and 5.9 we show their mobility curves. In the square superlattice case we have a decrease in the maximum mobilities of one order of magnitude when compared to their hexagonal counterpart. This is because the nearest neighbours are reduced from six to four, which reduces overall coupling. We can see that stoichiometry also has an effect in mobility, being Se rich the system with a higher value of this magnitude.

It can be seen in some of the last figures that mobility tends to plunge to low

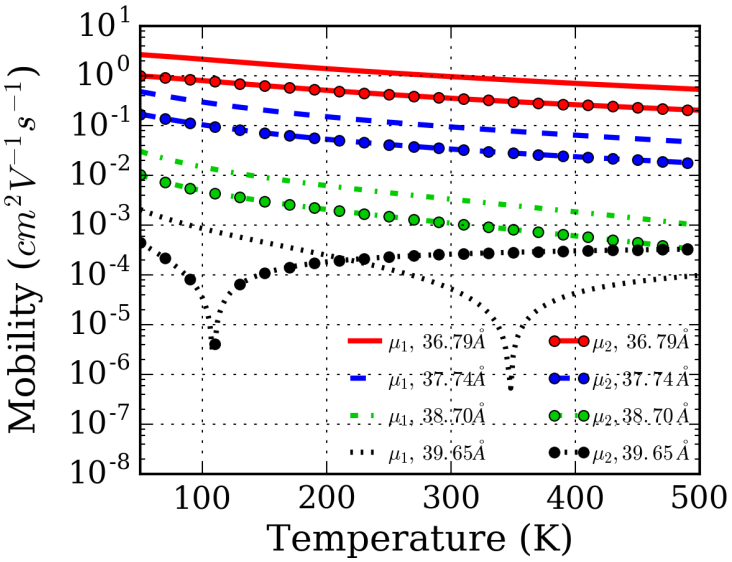

Figure 5.5: Absolute value of electron mobility curves for wurtzite CdSe 1.84 nm radius, with different dot to dot separations. The distances are measured from QD center to center.

values at certain temperatures and then tends to grow again. This is due to the fact that we are representing the mobility's absolute value. Actually, the mobility changes sign at a certain temperature. This phenomenon is explained in figure 3.4, and it is related to the miniband curvature. At low temperatures only the lowest energetic intervals of the miniband are populated thus affecting mobility. When temperature increases, higher energy levels are being populated. When the temperature is high enough a point is reached in which there is the same population above and below the energy where effective masses change sign and mobility reaches its lowest point. At higher temperatures, mobility raises again but with opposite sign. We cannot see these changes in any of the figures represented here because we chose to represent the absolute value of mobility.

This mobility decrease with temperature is a feature of band-like transport. Nevertheless, our model attributes this decrease to the QD superlattice electronic structure and its electronic occupation rather than the higher relevance of

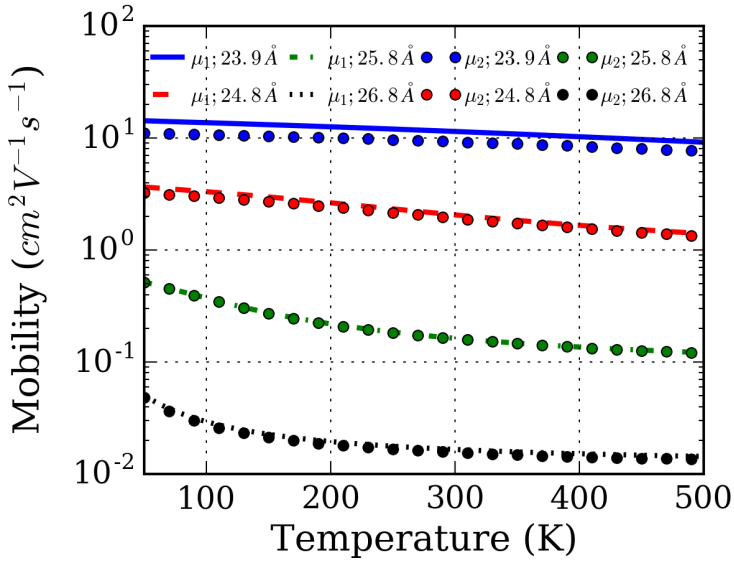

Figure 5.6: Absolute value of electron mobility curves for wurtzite CdSe 1.26 nm radius for different dot to dot separation. The distances are measured from QD center to center.

carrier-phonon scattering at higher temperatures.

Model for dot-to-dot separation

It has been shown that mobility changes drastically with dot-to-dot separation i.e. superlattice constant. We tried to capture this behaviour in a suitable model.

The overlap values show a roughly exponential dependence with superlattice constant. Mobility is dependent on the overlap quantities but in a complex, nonlinear way. At lower temperatures where only the lowest miniband states participate in transport the exponential dependence is clearer than at higher temperatures, where the presence of different energetic states create a more complex relationship with overlapping values.

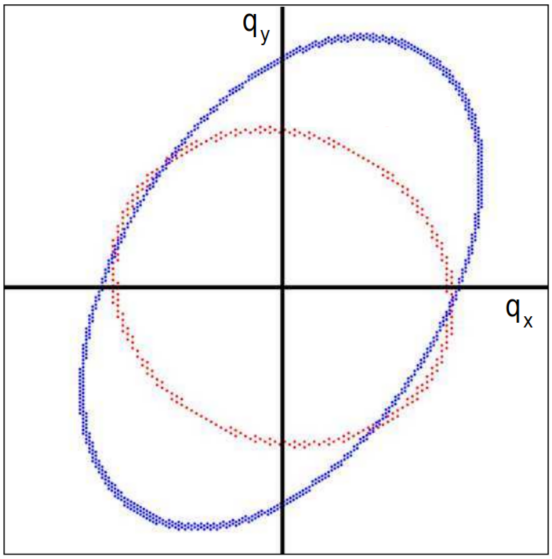

Figure 5.7: Representation of both energy minibands at a particular energy (5 meV above miniband minimum) for the CdSe 1.84 (blue) and CdSe 1.26 nm (red) radius wurtzite QDs. It can be observed a change in anisotropy with QD radius.

We proposed the following model

$$\mu_i(T, \Delta) = s_i(T) e^{\Delta \eta(T)} \tag{5.1}$$

where subscript $i = 1, 2$ is the eigenvalue index, $s_i(T)$ is the mobility for the minimum possible superlattice vector (QD in "contact" with first neighbours), $\Delta = d - d_0$ is the difference between actual interdot distance d and the minimum possible dot-to-dot separation d_0 and $\eta(T)$ is a parameter that modulates the exponential behaviour at higher temperatures.

Fitting curves for the model are shown in figure 5.10. As explained above, we found a much higher steep dependency with superlattice vector value at low temperatures than at higher ones, as shown in relation 5.2

$$\mu(300, \Delta) = \mu(300, d_0) \left(\frac{\mu(50, \Delta)}{\mu(50, d_0)} \right)^{5/4} \tag{5.2}$$

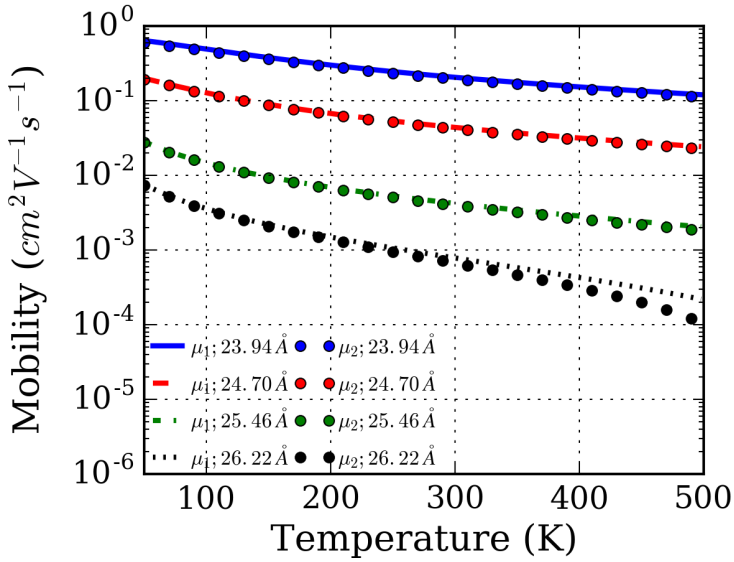

Figure 5.8: Absolute value of electron mobility curves for Cd-rich surface 1.22nm radius zincblenda CdSe QD for different dot to dot separation. The distances are measured from QD center to center.

5.2.4. Mobility as a function of impurity concentration

The dependence of mobility with impurity concentration is simpler. As seen in equation 3.4, the scattering rate is linearly proportional to the rate of impurities. The scattering rates are similar to each other and thus is the scattering probability. This allows all reciprocal space states to have a similar probability of being populated after scattering. All this means that if we multiply by some factor the concentration of impurities then all TOFs will be reduced by a similar quantity. Thus, the whole mobility is approximately inversely proportional to the impurity concentration ν. Figure 5.11 shows the effect of changing the concentration in the CdSe 1.86 nm radius QD hexagonal array.

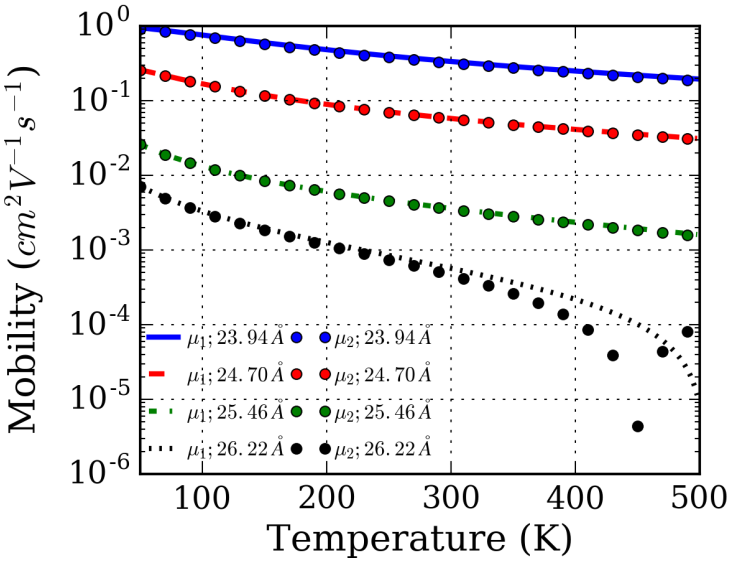

Figure 5.9: Absolute value of electron mobility curves for Se-rich surface 1.22nm radius zincblenda CdSe QD for different dot to dot separation. The distances are measured from QD center to center.

5.2.5. Comparison with the hopping model and real data

We have used real data from [3] and [4] where a FET device with CdSe quantum dots was built using different capping ligands. There are two major differences between our simulated systems and the ones used in the experimental set: i) in the experiment, the quantum dots are sandwiched between two dielectrics and ii) the QD ligands in the real systems affect to the wavefunction overlap because they fill the space between nanoparticles. In our case, the 2D periodic superlattice is surrounded by vacuum. Thus, our results represent a lower limit for superlattice mobility.

The hopping model used for comparison [64] is the one of equation 3.1. We also compare with a model for ordered nanocrystal films proposed by Efros and Shabaev [69] $\mu = \alpha/T^{1/2}$, which is valid when the Fermi level is below the miniband minima, as it is our case. The former system was used with an

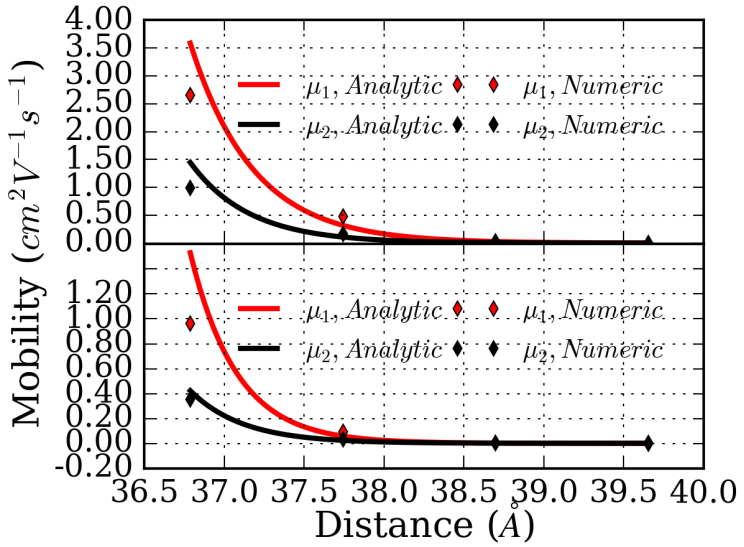

Figure 5.10: Mobility eigenvalues for 50 K (upper panel) and 300 K (lower panel) for the wurtzite CdSe 1.86 nm radius QD with 1 % impurity concentration. Solid lines represent the analytical fitting of equation 5.1.

activation energy $E_a = 25meV$ and $\alpha = 9.3$ in the second one.

We used our mobility simulation results and a toy model (curves labeled as "TM") where we set all the scattering rates to a particular constant value regardless the initial and final state. Results are shown in figure 5.12. They suggest that our model is the best fit to the experimental data, with a concentration of 1 % impurities (5 % size distribution) at 1 bond length separation.

5.2.6. Conclusions

In this article we explained our computational electron transport model, its approximations, its limits of validity, and proved to have a consistent, numerically stable simulator, in the ohmic regime for QD periodic superlattices.

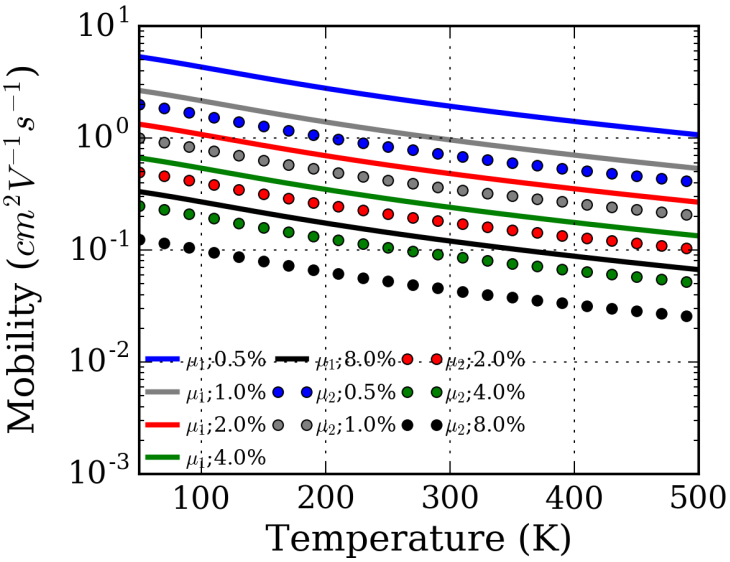

Figure 5.11: Mobility curves of CdSe 1.86 nm radius QD superlattice for different impurity ratios.

We calculated the electron mobility for four different QD superlattices with accuracy and in a wide range of physical variables avoiding a costly Monte Carlo process, thus allowing to speed up the computation by a large margin.

We also improved on aspects of mobility fluctuation that can arise from a finite discretization smoothing the fluctuations in the DOS obtained with a coarse reciprocal space adding a correcting factor that accounts for the real density of states.

We compared our results with experimental data, obtaining a good agreement with these. This suggests that our model could properly describe the carrier dynamics in QD superlattices, meaning that band-like transport scattering mechanisms could be dominated by size-variation scattering mechanisms around room temperature, and electron-phonon scattering having a secondary role as a thermalising agent.

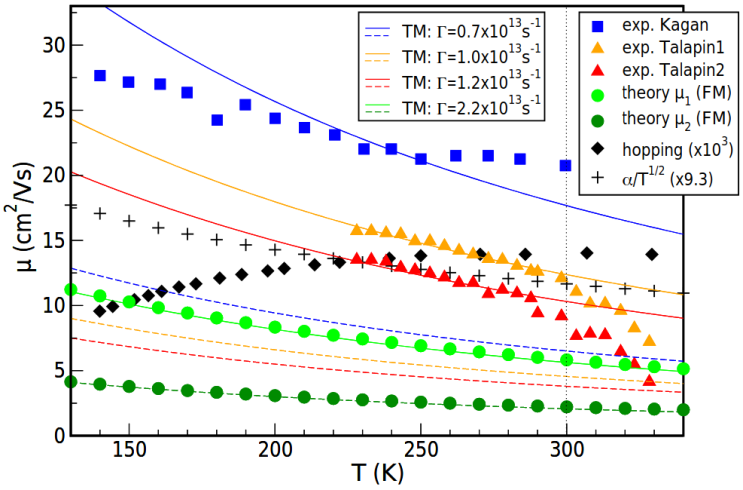

Figure 5.12: Comparison with experimental work from Talapin's et al FET in linear and saturation regime (orange and red triangles respectively), Kagan's experimental set (blue squares) the hopping models and our full model's mobilities eigenvector for the hexagonal superlattice of CdSe 1.86 nm radius and the toy model for different scattering ratios. It can be observed that our models capture the behaviour better, proving the utility of this work.

5.3. J. Chem. Phys. 151, 154101 (2019)

In this paper we reviewed a novel way to build intermediate band solar cells (IBSC) using quantum dots as the active material. IBSCs are a promising path to achieve an efficiency higher than the Shockley-Queisser limit (S-Q) [89–91, 95] by taking advantage of an intermediate band (IB). Two photons are involved in the process of generating a carrier. One promotes the electron from the valence band (VB) to the IB and another promotes it from the IB to the conduction band (CB). In this manner, the cell can convert photons into electric carriers using two different paths, depending on the photon energy: i) if the photon has an energy greater than the bandgap a VB-CB transition will happen, as in regular solar cells or ii) the photon has greater energy than the difference between intermediate and valence bands energetic separation thus the carrier will promote to the intermediate band (VB-IB transition) and then it

will absorb another photon with greater energy than the difference between the intermediate and conduction bands (IB-CB transition). Carrier extraction will happen as usual, extracting only carriers from the VB and CB only, being the intermediate band a carrier reservoir where electrons await to promote to the CB.

Using the detailed balance framework as in the S-Q model, one can explore different values for the energy differences $E_{IB} - E_{VB}$ and $E_{CB} - E_{IB}$ to yield maximum conversion efficiency [96, 97] as a starting point strategy to search for materials, stoichiometry, QD radius, etc.

IBSCs are not only restricted to quantum dot based structures. Anyway, the tunable properties of QDs makes them ideal to be used to create intermediate bands without having to use highly doped materials or heterojunctions, which have their particular problems in real devices as lattice strain or high synthesis difficulty [35]. In the field of QDs, epitaxial QDs made of InAs have been used in combination with a matrix of GaAsX[95]. The bulk GaAsX would provide the VB and CB bands while one of the states of the InAs QDs would be used as IB. Unfortunately these devices performed poorly compared to expectations.

A novel way to produce an IB with colloidal QDs as active material is described in [98]. In this case, intra-gap states (IGS) are created in the QD due to structural relaxation, according to DFT calculations. The IGS, as the name suggests, is an eigenstate with an energy inside the bandgap. Thus, a QD array with such IGS would contain the VB, IB and CB, so there is no need to embed it in another device as in p-i-n structures [99]. In the case of an IBSC, it is desirable the intermediate band to be as narrow as possible (no energy dispersion) and thus as a consequence the IGS should be very localized, having no overlap with any other wavefunction.

In [98] the calculations were made for CdSe QDs of R $\sim$ 0.6 nm, which are not commonly synthesized. Also, CdSe has a large bulk bandgap which is not the most efficient option from the IBSC perspective. Lastly, the intra-gap state in that system showed a high degree of delocalization. A delocalized state would

have overlapping wavefunctions in the array, thus creating a wide miniband. This is a problem for IBSCs since once the electron promotes to the IB it rapidly decays to its minimum energy state via thermalisation, loosing its excess energy and limiting the energetic spectrum otherwise available for the IB-CB transition.

In our work we have used two schemes to build an IBSC:

- Scheme I: We created an IB by inducing an IGS in the form of a surface trap. To do this we chose a site to remove a passivating bond to create a surface electron trap modeled according to [100]. This creates a highly localized state around the dangling bond site, and we chose in all examples a surface trap that is energetically distant from both VB maxima (VBM) and CB minima (CBM) states. When creating the superlattice these IGS create an IB that is distant from VBM and CBM. These IGS have been extensively documented [101–104]. In figure 5.13 whe show these states in the three InAs QDs used in this scheme. The selected radius are 0.6 nm, 0.8 nm and 1.0 nm.
- Scheme II: Taking advantage of the energetic difference between the CBM miniband (s-type orbital) and the next CB minibands (p-type orbitals) that exist in InAs QDs we decided to analyse the use of the CBM as an IB. For this reason we selected two bigger QDs, with 1.2 nm and 2 nm radius, where this effect is more prominent.

InAs is a good candidate for IBSC since its 0.4 eV bulk bandgap provides a good starting point matching the solar spectrum.

5.3.1. Results

In this section, for the sake of clarity, we have separated the results obtained within schemes I and II

Scheme I: Using IGS

There are two conditions required for an IGS to be a good candidate for IBSCs: i) it has to be separated by a zero density of states from VB and CB.

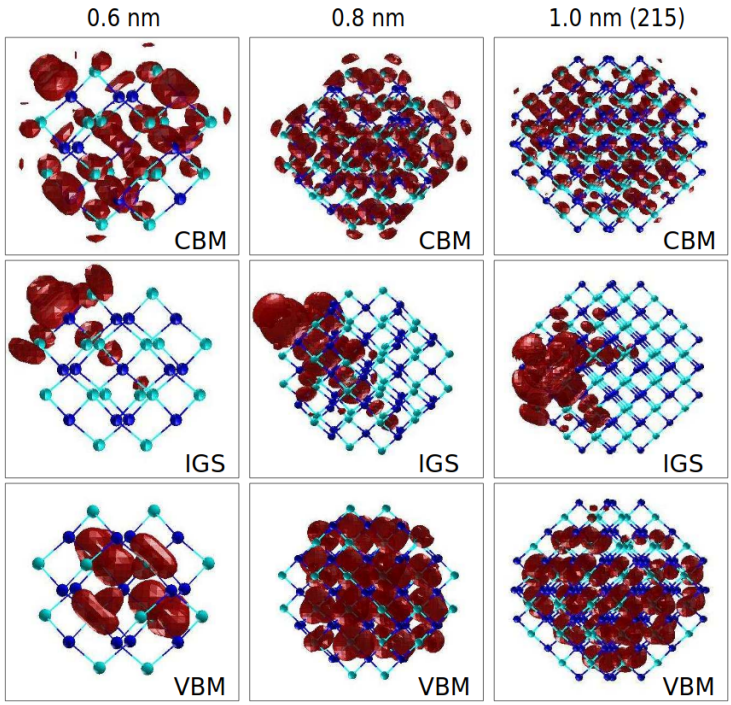

Figure 5.13: Charge density representations. In columns from left to right: 0.6nm, 0.8 nm and 1 nm quantum dots. In rows from up to down: Minimum energy conduction band eigenstate, intra-gap state and valence band maximum energy eigenstate. These are the quantum dots used in scheme I of this work.

This provides to each level its own quasi-Fermi level and, if separated enough energetically, non-radiative recombination will not be important since the energy difference $E_{IB} - E_{VB}$ and $E_{CB} - E_{IB}$ is much greater than the phonon energies, and ii) there have to be a high number of VB-IB and IB-CB transitions, since a great portion of the spectrum is converted into carriers through the IB path.

We can see in figure 5.14 that in the case of the isolated QDs proposed for scheme I both conditions are fulfilled. The three coloured curves indicate which type of transition is being represented, being VB-IB black, IB-CB red and VB-CB green. Solid vertical lines are the transition probability between the different

states of the isolated QD, and the dashed and solid curves are a lorentzian broadening of 50 meV and 100 meV respectively, used to create a preview of how suitable the QDs are when used in a superlattice.

Not any value of transition probabilities makes a good candidate for IBSCs. If for example IB-CB is very low compared to VB-IB transitions, the IB states will fill up, and will severely limit VB-IB absorption. If the opposite happens, the IB will have no carriers to promote to the CB. Thus, a low transition rate in one of the two processes will be a bottleneck for the whole conversion process.

We can see from the solar spectrum in figure 5.15 that most of light energy is in the form of low energy photons. This has to be taken into account when evaluating if the relationship between transition probabilities is convenient. Generally, the lowest energetic process should have the biggest absorption rate, since it is in the lower part of the spectrum (near infrared and infrared) where the majority of photons exist.

We can see in figure 5.14 VB-IB and IB-CB transitions are reduced as the radius increases. There is also another property that has to be taken into account, which is IB width. On one hand the IGS-derived miniband should have some width. This would help the IB to be partially full, facilitating the IBSC operation. On the other hand, too much width would produce a high energy loss due to phonon interaction. It has to be taken into account that the thermalisation scattering rates in the case of QDs are normally slower than in the bulk case [72].

Figure 5.16 shows the miniband structure and absorption for superlattices built with QDs following scheme I. Both the IB curvature and intragap transition rates increase with decreasing QD radius. This means that there is no easy way to select the ideal QD when it comes to the QD radius: too small will have high intragap transition rates (i.e. transitions between valence band and intraband or intraband and conduction band) as seen in figure 5.14 but will likely have an IB band width too high and thus a higher energy loss in the IB. A bigger

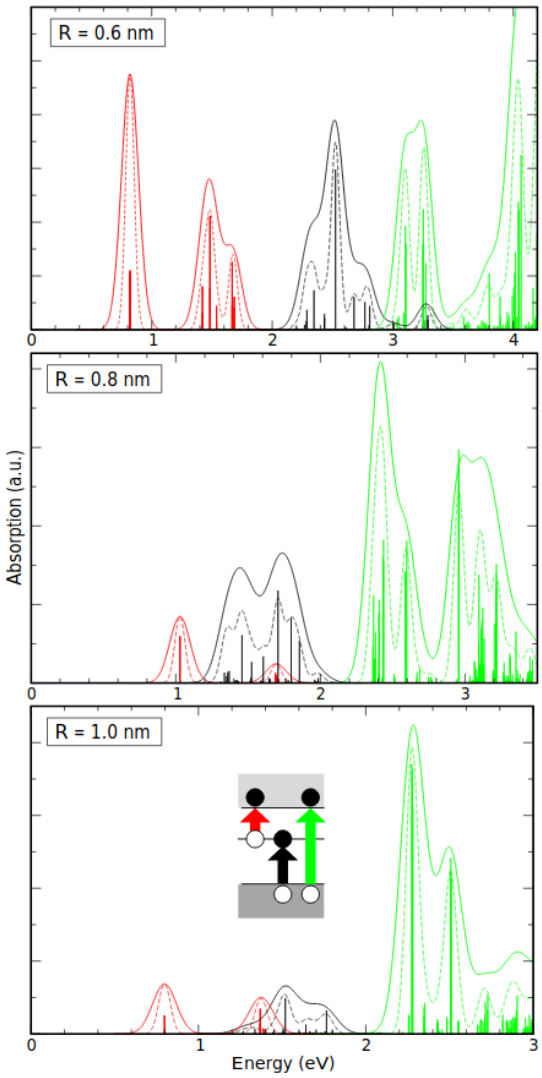

Figure 5.14: Absorption spectra of InAs isolated QDs used on scheme I. Green, black and red colours represent VB-CB, VB-IB and IB-CB, respectively. Vertical lines represent transition rates between the discrete energetic states of the QD. Doted and dashed lines represent the same states' transitions broadened by 50 meV and 100 meV respectively, to show a glimpse of how a superlattice made out of these QDs would behave.

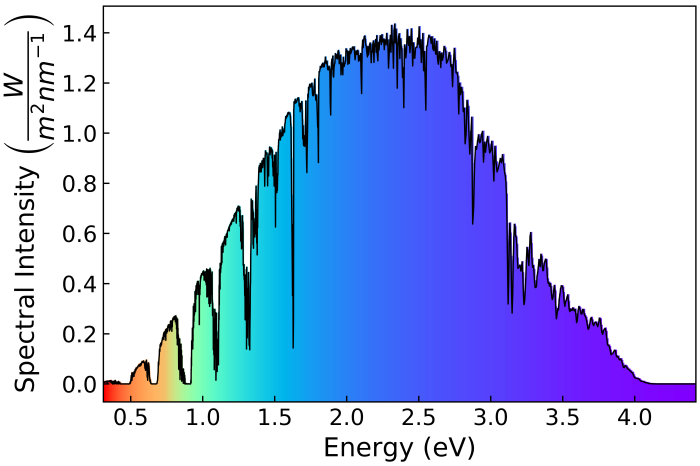

Figure 5.15: Solar spectral energy density at sea level.

QD would have lower intraband transition rates but a smaller IB curvature. In CdSe QDs, for example, it has been observed [105] an IB width proportional to D^{-2} where D is the QD diameter. Lastly, a CBM lowering has been observed in 0.6 nm and 0.8 nm radius QDs, which suggests that the superlattice properties, such as light absorption, cannot be simply deduced from the isolated QDs.

In this work we chose to place the Fermi energy in the middle of the IB, thus providing the partial filling needed to guarantee that there will be both VB-IB and IB-CB transitions.

It is also important to underline that this is a best case scenario since our superlattices are perfectly periodic. In a real system there will be size dispersion and superlattice dislocations which will broaden the absorption range but will affect mobility in a negative way.

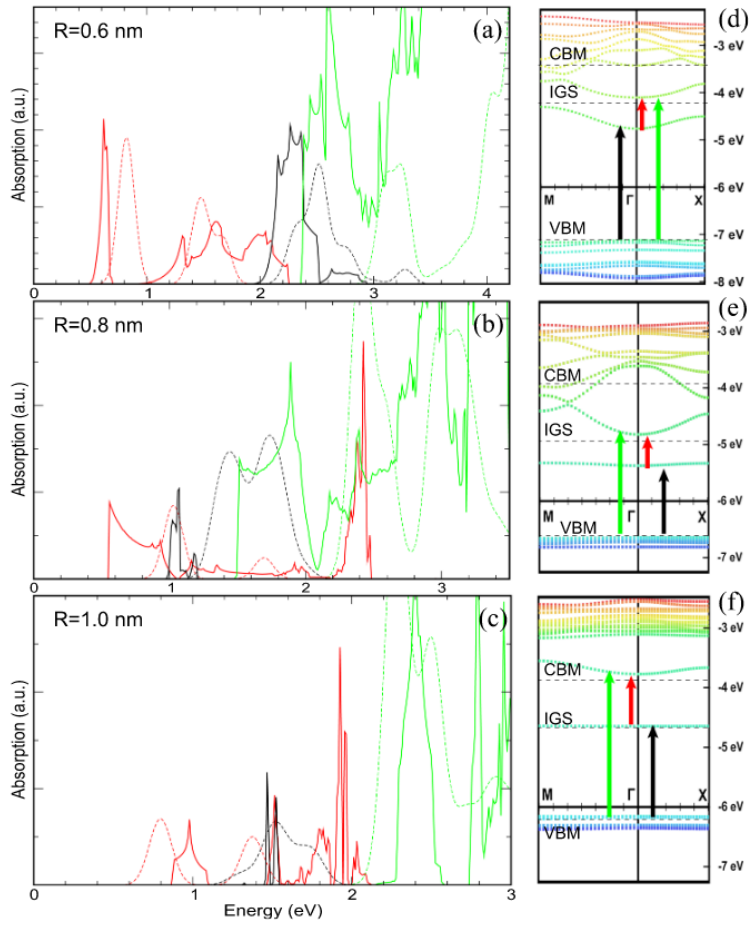

Figure 5.16: Absorption spectra (doted lines are the isolated QDs for comparisson with superlattice, in solid lines) and minibands for the three quantum dots used for scheme I. It can be seen how miniband structure is strongly affected by the selected QD. It is also clear that the QD absorption is more redshifted the smaller the QD.

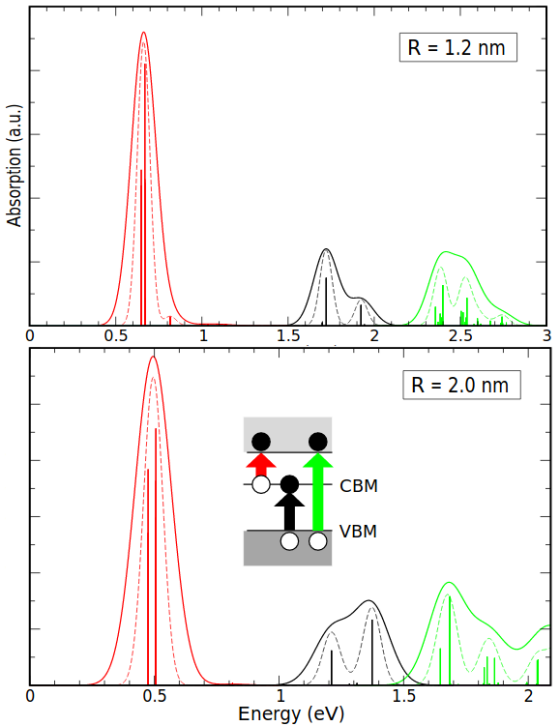

Figure 5.17: Absorption spectra of InAs isolated QDs used on scheme II. Green, black and red colours represent VB-CB, VB-IB and IB-CB respectively. Vertical lines represent transition rates between the discrete energetic states of the QD. Doted and dashed lines represent the same states' transitions broadened by 50 meV and 100 meV, to show a glimpse of how a superlattice made out of these QDs would behave.

Scheme II: Using CB lowest energy miniband

In our second scheme we take advantage from the energy difference between the s and p orbitals, from which the first to the fourth miniband come from. The system still accomplishes the above conditions, namely a 0 DOS between VB-IB and IB-CB and there is a high transition rate between all minibands. To avoid confusion between the first and the rest of conduction band minibands, we refer to the lowest energy miniband from the CB (which is now used as IB) as M_1 and the p-states derived minibands as $M_{2,3,4}$.

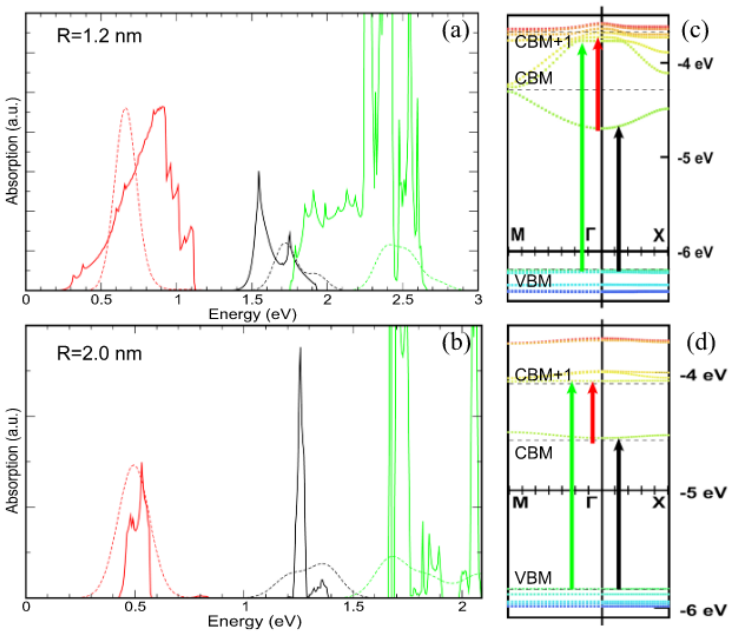

Figure 5.18: Absorption spectra (dotted lines are the isolated QDs for comparison with the superlattice, in solid lines) and minibands for the three quantum dots used for scheme II. We observed a redshift in the R=1.2 nm absorption. We also observed that with 1.2 nm radius, M_1 and M_2 are very near in the limits of the Brilloin zone, which could yield high recombination rates yet this is compensated with a lower transition rate in that region of reciprocal space.

We found that 1.2 nm and 2.0 nm radius QDs are good candidates to achieve a QD superlattice that surpasses S-Q efficiency because of their energetic levels position and because of their good balance between VB-IB and IB-CB processes, as shown in figure 5.17.

In figure 5.18 we can see specially for the 1.2 nm case that $M_{2,3,4}$ are wide enough as to provide good electron transport. Apart from the energetic shift observed (specially) in the R=1.2 nm case the minibands' relative position still offers a good chance to overcome the S-Q limiting efficiency.

	Isolated		Film	
R (nm)	η (1 sun) (%)	η (100 suns) (%)	η (1 sun) (%)	η (100 suns) (%)
		IB = IGS		
0.6	<30	~30	$\lesssim$30	~35
0.8	~37	39–44	40–43	52–54
1.0	~46	52–54	43–45	48–52
		IB = CBM		
1.2	~38	45–50	48–49	54–55
2.0	~43	52–54	40–43	48–52

Table 5.1: IBSC efficiency limit calculations for the InAs QDs used in this work, for 1 sun and 100 sun concentration, and for the isolated QD and in array arrangement (film) cases. Estimations are based on Bremner, Levy, and Honsberg [97] and Krishna and Krich [96].

5.3.2. Assessing real efficiencies

As it has been said before, our case of study is a best case scenario for the efficiency estimation since in table 5.1 we are assuming a) carrier mobilities to be infinite, b) no non-radiative recombination and c) complete absorption of all energies compatible with the miniband positions.

For assumption a) we refer to [105] where we found that R=1.2 nm and R=2.0 nm QDs have mobilities of the order 2.6 and 0.4 $cm^2V^{-1}s^{-1}$ respectively. Assuming the mobility to be dependent on the miniband width, we can assume mobilities of the same order of magnitude for the five QDs used in this work. For assumption b), in a recent work [106] it was found that recombination is proportional to mobility, since the carrier is more capable of finding paths to low energy states via diffusion to electron traps. Thus high mobility, while increasing short circuit current (J_{sc}) can yield a lower open circuit voltage (V_{oc}), thus affecting overall efficiency. In agreement with our work, the mobility is inversely dependent on QD radius. To summarize, smaller QDs can yield better mobility

and, counterintuitively reduce the operation efficiency. This is another balance to do when choosing a QD candidate for solar cells. In [106] they concluded that the best mobilities were in the range of 10^{-3}-10^{-2} $cm^2V^{-1}s^{-1}$, although this margin could be different if the quality of the superlattice improves i.e. has less carrier trap density. Finally, for assumption c) quantum dots superlattice have a separation from the first CB miniband to the rest that reduces as the QD size increases. This makes bigger QDs superlattices to have smaller absorptionless windows in the IB-CB transitions, which makes them preferable over the smaller ones, from the spectrum absorption point of view. In the case of the absorptionless window in the VB-IB transitions, these are because of the lack of valence band minibands included in the simulations. The 0.8 nm radius QD is the better candidate from this point of view. Also, molar extinction coefficient (the light extinction per unit QD) is greater in bigger QDs, which, for limited QD stacking can tip the balance of choice to the bigger QDs[107–113] .

Taking into account the previous reasoning, we concluded that for scheme I the best QD is the one of R=0.8 nm while for scheme II we could be interested in bigger QDs since the $M_1 - M_{2,3,4}$ curvatures are lower and thus thermalisation would have less effect on conversion losses in the IB-CB transitions. Also in the 2 nm radius case there is a nearly constant energetic difference between minibands. Anyway, there is an upper limit for viable candidates. Over R=3.5 nm the gap (energetic difference between $M_{2,3,4}$ and VB) would be too small. So we deem as reasonable to consider QDs of $2 < R < 3.5$ nm.

5.3.3. Final comment

To end the discussion on quantum dot based IBSCs we make the following remarks on other properties apart from conversion efficiency that are necessary to have a working solar cell.

Charge extraction Once generated, carriers have to be extracted from the solar cell in order to be used as energy source. In the case of an IBSC we have an intermediate band from which carriers have not to be extracted. This can be done in two ways: i) by using selective contacts that will not accept carriers

with the IB energy or by blocking the IB in the regions near to the contacts e.g. materials such as ITO or LiF/Al/Ag for PbS QDs [106] and TiO for CdSe ones [114]. The particular path for selecting only carriers from the VB and CB is out of the scope of this work. However this inconvenience could be compensated by the fabrication simplicity that these devices suggest, specially when compared to more proven concepts such as the tandem solar cell which is difficult to build[115].

IB occupation As said before, the intermediate band has to be partially occupied to maintain a continuous flow from VB to CB via the IB. In epitaxial QD systems maintaining this condition has been proved to be challenging[116]. To overcome this it has been proposed to make use of smaller QDs in more compact and lower impurity concentration superlattices, and to use doping (either photodoping or electrical) to position the Fermi level in the middle of the IB. Colloidal QDs are a promising pathway to achieve this, since they can be synthesized in very small sizes, and with low size dispersion. Also, passivation allows them to build highly dense and ordered arrays. In the field of epitaxial quantum dots this has been difficult because lattice strain increases when the QD is smaller, creating surface traps.

Excitonic nature of spectrum absorption The discreteness of the electronic states and the ensuing discrete character of the excitonic optical transitions in QDs may significantly reduce the single junction conversion efficiency, by reducing the photogenerated current[115]. The main origin of this effect is the transparency of the QD absorption spectrum between sets of absorption peaks, which is more pronounced for R=1.0 nm and 2.0 nm but is also present in all other sizes (see figures 5.16 and 5.18). However, CQD-based IBSCs have two additional advantages: minibands with a finite width and absorption rates that increase with increasing energy. Both properties are crucial to achieve conversion efficiencies beyond the S-Q limit as they ensure the participation of photons of the lowest possible energy in the available absorption processes, avoiding the loss of photon energy in excess of the energy gap[115]. When high and low energy absorption processes compete, the required photon selectivity is “naturally” achieved in CQD-based IBSCs, where higher energy processes are more strongly absorbing

compared to lower ones as apparent from figures 5.16 and 5.18. The finite miniband width introduces, however, an upper bound on the energy of the absorbed photons, which in practice is not likely to lead to significant losses, considering that such photons are already filtered by the atmosphere or by the use of ultraviolet absorbers (protecting the cell encapsulation), providing a similar high energy cutoff[117].

5.3.4. Conclusions

We reviewed a novel path to produce QD based IBSCs by using two different IB schemes. One using an IGS as IB and the other using the lowest energy miniband of the CB. These devices can surpass the S-Q efficiency limit and, in the case of InAs, we came to the conclusion that the best candidates for an experimental setup are the 0.8 nm radius when using IGS as IB and for completely passivated QDs the radius should be between $2 < R < 3.5$ nm.

5.4. Phys. Chem. Chem. Phys., 2019, 21, 25872 (2019)

In our previous mobility work [65] we investigated QD arrays having one type of impurity. This is an approximation since real systems have a size distribution instead of only one sized impurity.

In this article we showed our results when using various impurities i.e. more than one differently sized QD. We used this to calculate the electron mobility of an InSb R=13Å 2D periodic superlattice in a more realistic way. Then we showed some theoretical results that allow us to build a model that can describe transport for any size distribution while avoiding a great amount of computation, and we used these findings in a reversed manner to estimate the size distribution of an experimental set based on the measured mobility.

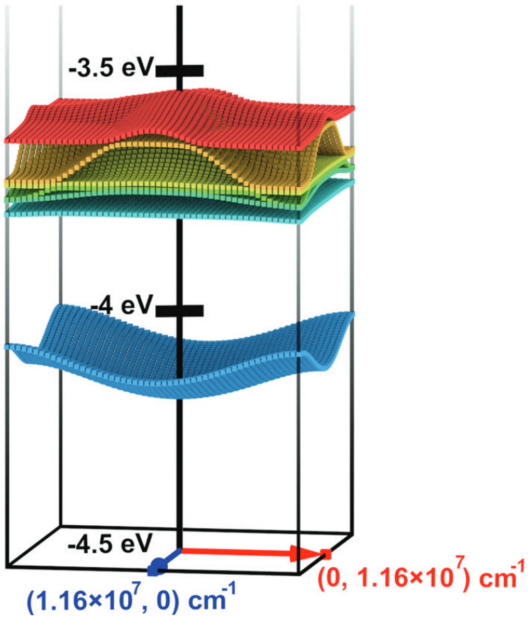

Figure 5.19: Miniband structure for the 2D square periodic array of 13 Å radius InSb QD, at minimum superlattice vector i.e. one bond length separation from dot to dot

5.4.1. Mobility calculation with various impurity QDs

After the already described process of using the pseudopotential and tight binding model, we obtained the miniband structure for the system we chose in this case, InSb R=13 Å QD, which is shown in figure 5.19. We chose three different impurities: 11.94 Å and 11.2 Å radius InSb QD and the vacancies, which are "quantum dots" with zero-valued potential (vacuum). Figure 5.20 shows a cross section of the potential energy difference ($\Delta V(\mathbf{r})$) of the three impurities with the periodic InSb QD, which is a central quantity when evaluating the scattering rates and thus the mobility. We also simulated CdSe 20Å radius with various impurity sizes to compare results with the InSb case.

With three impurities we have to specify three different concentrations. In order not to be confusing with notation, we add a superscript to the scattering

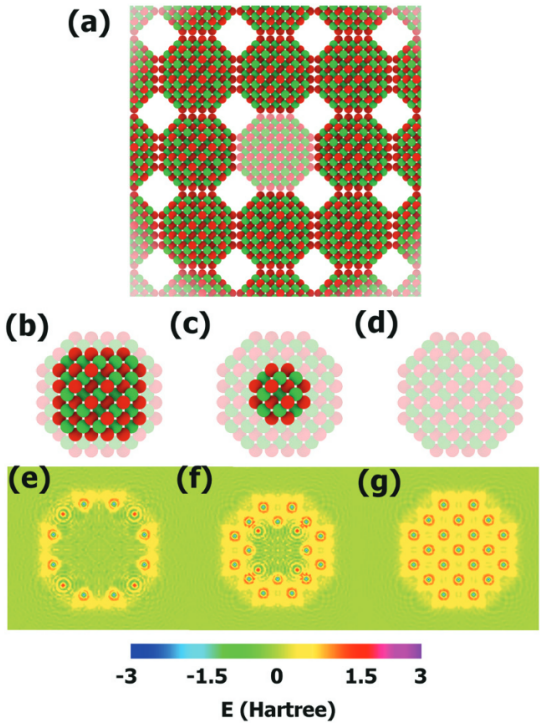

Figure 5.20: Impurities used in this work. a) a sample of the superlattice where the semitransparent QD is replaced by an impurity. b), c), d) comparison between periodic (semitransparent) and impurity (solid) QD atomic arrangements for 11.94Å, 11.2Å and 0Å radius respectively. e), f), g) represent a cross section of the potential difference between the periodic QD and the three impurities in the same order.

rates and concentrations throughout this work. For example, the scattering ratio and concentrations of the 11.94 Å QD will be expressed as $\Gamma^{(11.9)}$ and $\nu^{(11.9)}$ respectively.

In figure 5.21 we can see the mobility per energetic interval for different impurity concentrations and QD impurity sizes. It is noticeable that, for a given energetic interval, mobilities are inversely proportional to impurity concentration; we noted this earlier in our works by stating the inverse relationship $\mu \propto \frac{1}{\nu}$. One important finding in this article is that mobilities for different impurities are

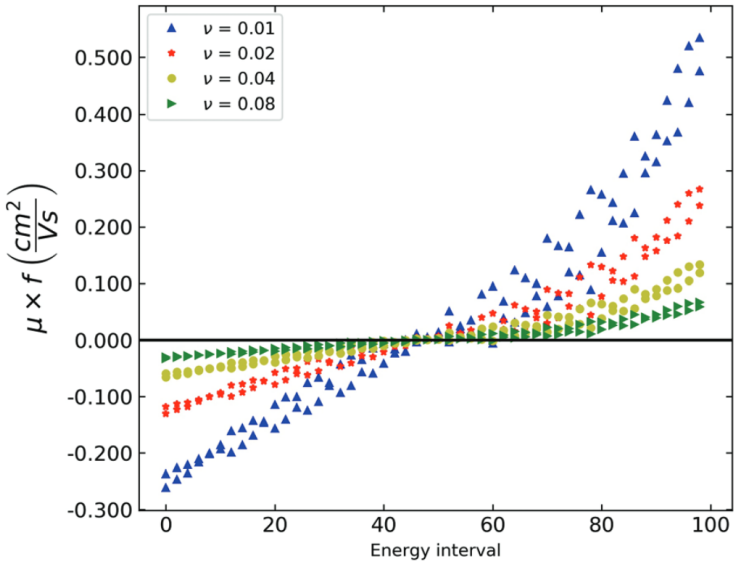

Figure 5.21: Mobility as a function of energetic interval for different impurity concentrations. The three impurities were used separately in each simulation. When concentration is changed the curves vary inversely proportional to the concentration value. However, when the impurity is changed, the whole curve is changed as if it were multiplied by a constant value, which is represented as f in the y-axis. We used $f = 1$ for the 11.94 Å radius impurity, $f \approx 1.6$ for the 11.2 Å one and $f \approx 8$ for the vacancy to make all impurity curves coincide at each of the concentrations shown in the legend. This is a consequence of the relationship of equation 5.3.

proportional:

$$\frac{\mu_{E_i}^{r_i}}{\mu_{E_i}^{r_j}} = constant \tag{5.3}$$

Relation 5.3 shows the paramount importance of the miniband curvature. In order to understand this relation, it is important to remark that there are two factors that affect mobility the most. One is the TOF, which depends on scattering rates, which depends on the impurity QD. When the impurity QD is changed and the mobilities are compared, they show the above relation. The other factor is the energy gradient or miniband curvature. We showed our theoretical breakthrough on this matter in the next subsection.

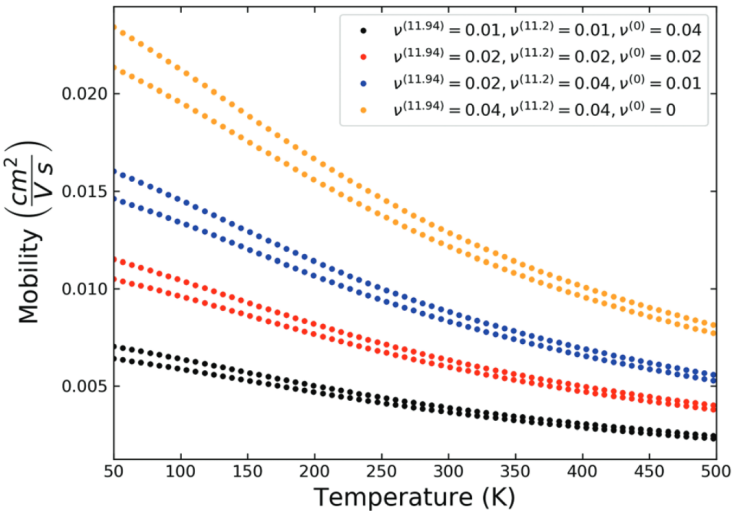

Figure 5.22: Mobility as a function of temperature (Fermi level at 100 meV below the minimum of the lowest energy miniband) for different combination of impurity concentrations. It can be seen that the vacancy governs the overall value, since the lowest mobility curves are the ones with highest vacancy values, regardless to the values of the similar impurities.

There is also another expected behaviour, which is that the more similar the impurity is to the periodic QD size, the lower the scattering rates it produces and the higher the mobility for the same concentration and conditions. Figure 5.22 shows the mobility calculations when all three impurities are present with different concentrations profiles. It can be seen that the most important impurity in terms of how it affects mobility is the vacancy, since this yields the greatest values when equation 3.15 is applied.

5.4.2. Mobility dynamics extraction

The theoretical work in this article is explained in section 3.6.1. It can be synthesised as follows:

- It is possible to calculate the scattering rates of the unphysical impurity

concentration of $\nu = 1$ (all QDs are impurities) and average the scattering rates for all the miniband states, as shown in equation 3.16, noted as $\tilde{\Gamma}^{(r)}$.

- Then, the mobility tensor for each energetic interval, $\mu_{E_i}^{(r)}$ can be calculated. The superscript r denotes that this is calculated for a particular impurity, the same that is used in the scattering calculation above.

- Plugging this results into equation 3.11 and multiplying by the scattering rate $\tilde{\Gamma}^{(r)}$ we obtain equation 3.17. It can be proved that this quantity, $\hat{\Theta}$, only depends on the miniband features, and is completely independent of the particular impurity used for its calculation.

- To obtain a quite accurate mobility value for a particular set of QD impurities with varying concentration rates, we calculate all $\tilde{\Gamma}^{(r)}$ to interpolate a continuous function and use it with equation 3.18 as below

$$\hat{\mu}(E_f, T) = \frac{\hat{\Theta}(E_f, T)}{\sum_r \nu^{(r)} \tilde{\Gamma}^{(r)}} \tag{5.4}$$

It has to be taken into account that this is an approximation, since we averaged all the scattering rates to be able to factor them out of the whole Markov chain, which would be impossible if scattering rates are different from one another.

In figure 5.23 we showed the $\tilde{\Gamma}^{(r)}$ for different QD impurities placed at periodic InSb 13 Å and CdSe 20 Å QD radius 2D periodic superlattices. Both models were fitted with a second order polynomial, $\tilde{\Gamma}^{(r)} = a \times (R - r)^2 + b \times (R - r)$ where R is the periodic QD radius and r is the impurity radius. The values (a,b) in the InSb case were (0.0248 $Å^{-2}s^{-1}$, 1.041$Å^{-1}s^{-1}$) and in the CdSe case (0.046 $Å^{-2}s^{-1}$, 0.0147$Å^{-1}s^{-1}$), which, as shown in the figure, reflects very distinctive behaviours with radius impurity. We concluded that this behaviour depends on many factors and we cannot draw conclusions for a particular QD beforehand. According to these fittings, we suggested to interpolate $\tilde{\Gamma}^{(r)}$ in order to obtain information for these impurities in the ensemble whose mobilities have not been explicitly computed, avoiding the whole mobility calculation process for them.

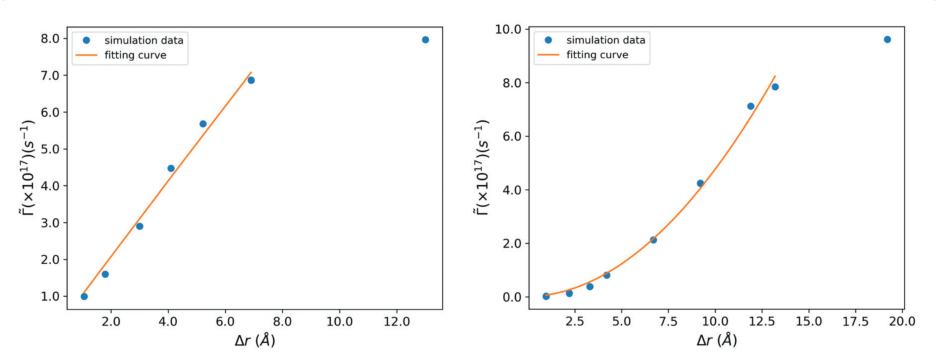

Figure 5.23: $\tilde{\Gamma}^{(r)}$ representation as a function of the periodic and impurity radius difference for InSb R=13 Å (left) and CdSe R=20Å (right). Several impurities were used in each case in order to obtain a good interpolation. In both interpolations the vacancy has been excluded. Both models were fitted with a second order polynomial, $\tilde{\Gamma}^{(r)} = a \times (R-r)^2 + b \times (R-r)$ where R is the periodic QD and r the impurity radius. The values, (a,b) in the InSb case were (0.0248 $Å^{-2}s^{-1}$, 1.041$Å^{-1}s^{-1}$) and in the CdSe case (0.046 $Å^{-2}s^{-1}$, 0.0147$Å^{-1}s^{-1}$).

5.4.3. Size dispersion estimation

Based on the above results we concluded that we can calculate a mobility for a QD impurity distribution profile given precalculated scattering ratios from a set of impurities.

There exists an infinite number of concentration profiles that would yield a particular mobility value. Instead of guessing separately each concentration value, we assume in this section the most realistic case, a gaussian size distribution. To this end, we propose that concentrations follow the equation below

$$\nu^{(r)} = \frac{e^{-\left(\frac{r-R}{\sigma}\right)^2}}{1 + \sum_r e^{-\left(\frac{r-R}{\sigma}\right)^2}} \tag{5.5}$$

where σ is the standard deviation of the Gaussian distribution, a measure of size dispersion.

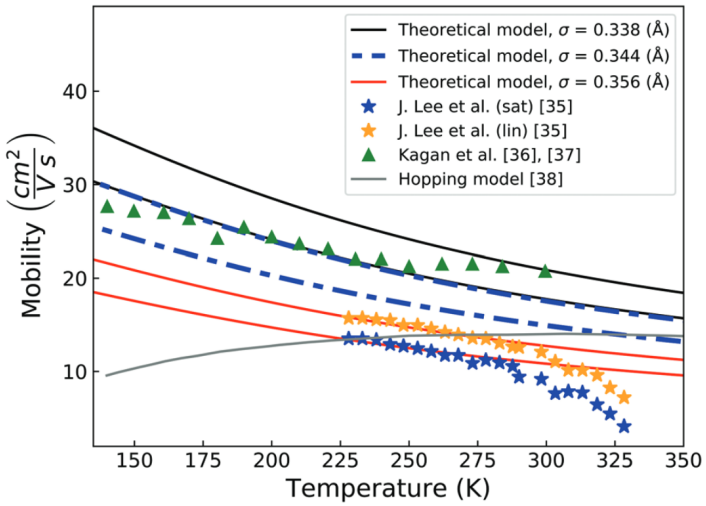

Figure 5.24: Fitted Gaussian distribution of sizes for experimental results of Kagan et al. [3, 118] and Talapin et al. (shown as J. Lee et al. in the legend) [4]. Hopping model mobilities are included to compare.

Figure 5.24 shows the fitted standard deviation of the assumed Gaussian profile for size distribution for the experimental results of Kagan et al. [3, 118] and Talapin's group results (shown as J. Lee et al. in the legend) [4]. It can be observed a good agreement between our model and experimental data, highlighting the viability of our model as a tool to predict size distributions in QD superlattices from mobility measurements and, conversely, carrier mobilities in superlattice for particular QD size profiles. The fitted values where in agreement with the experimental samples ($< 5\,\%$ size standard deviation).

5.4.4. Conclusions

We presented our mobility model applied to an impurity size distribution to achieve more realistic results. After the theoretical derivations conducing to this possibility, we studied the relationship between the electron mobility and

changing impurity size and used the fact that changes in mobility with impurity size can be used to build a continuous model. We concluded that, given scattering rates that are similar across the first Brillouin zone, the miniband characteristics are responsible for the mobility behaviour, rendering the impurity size dispersion as the factor responsible for the actual values of electron mobility. Finally, we used this theoretical breakthrough to predict mobilities for two types of QD superlattices, for which a Gaussian distribution for QD size dispersion is assumed.

5.5. Nanoscale Adv., 2, 384 (2020)

In this article we analysed the absorption coefficient dependency on the different properties of a 2D film. These are, namely, QD size, superlattice constant (sometimes referred as dot to dot separation), surface stoichiometry, morphology, temperature, Fermi level and light polarization.

We have observed a blue shift in intra-band transitions, i.e. the energy difference between minibands of the conduction band are bigger than the ones of the diluted/isolated QDs albeit we also observed the expected [119–122] red shifts for transitions from the valence band to the conduction band. All the parameters we vary along the paper have strong repercussions over these effects, which translates into not only a variable absorption strength but also on a variable absorption spectra.

We found that these energetic shifts are closely related to the miniband structure, the miniband shape and width being the most important features. These, in turn, as often noted throughout this work, are dependent on the QD wavefunction overlaps. Overlaps are highly affected by surface morphology, stoichiometry and QD radius.

The absorption shifts are greater at (in order of importance): i) smaller QDs, ii) smaller superlattice constants, iii) anion-rich surfaces and iv) morphologies allowing interlocking. We call interlocking to the possibility of

placing the dots closer due to features in their surface; as shown below, in the case of the spherical quantum dot the superlattice constant can be less than its radius. These effects leads us to the conclusion that it is not possible to predict the collective superlattice behaviour from the isolated/diluted QDs.

5.5.1. Theoretical method

As usual, we begin with the potential and eigenfunctions of the isolated QDs obtained via pseudopotential method. We then use these results to obtain the superlattice miniband structure. In this work, we used a denser discretization of the Brillouin zone, $Q_s = 501 \times 501$. This helps to obtain better quality results in the absorption curve. We have observed during our research that for a sparser discretization the absorption curve was too noisy. Therefore, we chose to compute on a denser one.

The index of refraction has been set to 1 in this work for simplicity.

5.5.2. Results

In order to observe how the different physical properties affect to absorption we used four different types of QDs or *systems*

- A) InAs 1.2 nm radius cation centered QD
- B) InAs 1.2 nm radius anion centered QD
- C) InAs 2 nm radius spherical QD
- D) InAs 2 nm radius rough-faceted QD

Type A and B QDs are of the same size and shape, with the only difference being that their atoms are interchanged, which allows us to observe the effects when only surface stoichiometry is changed, A-type and B-type being anion and cation rich respectively. System C is also cation rich thus comparisons between B and C can be used to study the effects of changing the QD size. Systems C and

D are also closely related. The QD in C is the same as in D but it has two extra As atoms in each of its six faces. These extra atoms are placed in a way that allows inter-locking between type C QDs, like two Lego™ pieces. The differences between systems C and D allows us to observe how morphology affects the system.

Figure 5.25 shows the four types of QDs and their respective miniband structures. All the eigenstates considered for the tight binding expansion are above the QD bandgap. We have considered 7 QD eigenstates for systems A,C and D, and 8 for system B.

In this work we noted the different minibands M_i where i is the miniband index in order of increasing energy. We observe that in all cases the lowest energy miniband is very distant from the rest and has its lowest energy at the Γ point. Also, the maximum and minimum energetic separation between M_1 and M_2 is at the Γ point an the Brillouin zone boundaries respectively.

It is clear that system A is the one with the widest M_1 which is a sign that it has the most overlapping wavefunctions. We also observed blue shifts in the absorptions, in contrast to what is usually expected from [119–122]. We have to recall that this is not in disagreement with experimental results since what we are simulating are absorptions between minibands inside the conduction band, not across the bandgap as observed in those works. In fact, figure 5.26 shows a comparison between transitions of the isolated QD and the nanocrystal film. Transitions are separated into interband (across de gap) and intraband (inside the conduction band) and it can be seen that the interband transitions are red shifted in accordance with experimental data. In table 5.2 we show the energetic difference between the first and the next four states, along the Γ point for the superlattice and the isolated dot. It can be seen that these quantities are always greater in the periodic case than in the isolated one.

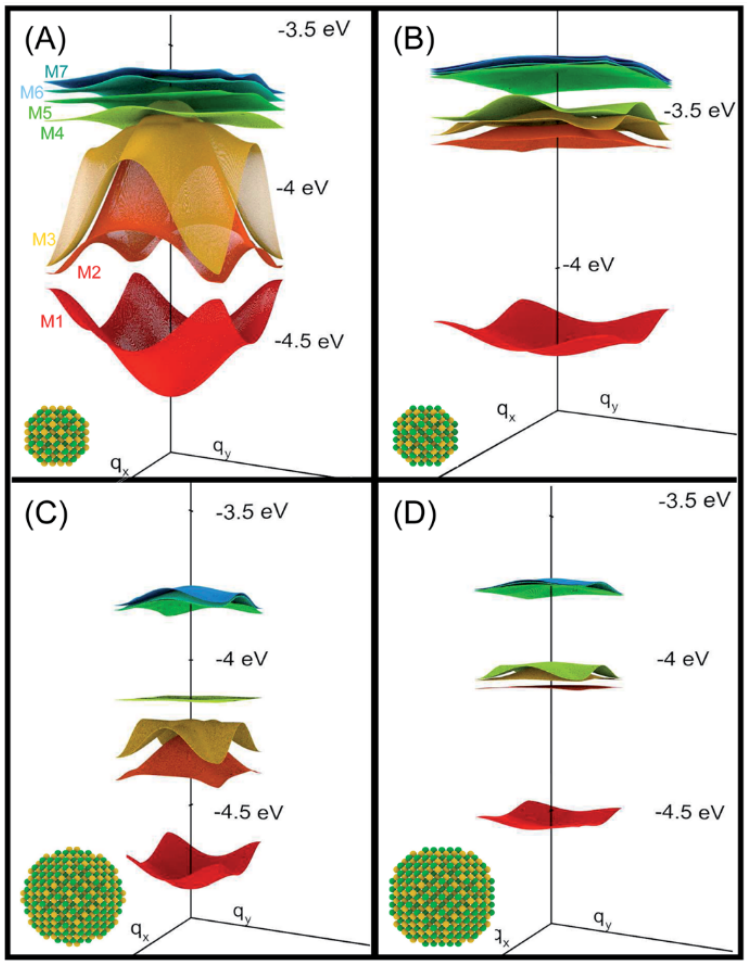

Figure 5.25: The four types of QDs used as building blocks for the superlattices throughout this article. Letters in the upper-left corners of each panel correspond with the systems labelling. Here is visually represented how systems A and B have the same QD but interchanging indium and arsenide atoms, green and yellow respectively. It can also be observed how the D system is faceted and that spherical system C is identical with the exception of the two extra As atoms in each face. It is also evident from this representations that system A stands out in terms of miniband width and curvature.

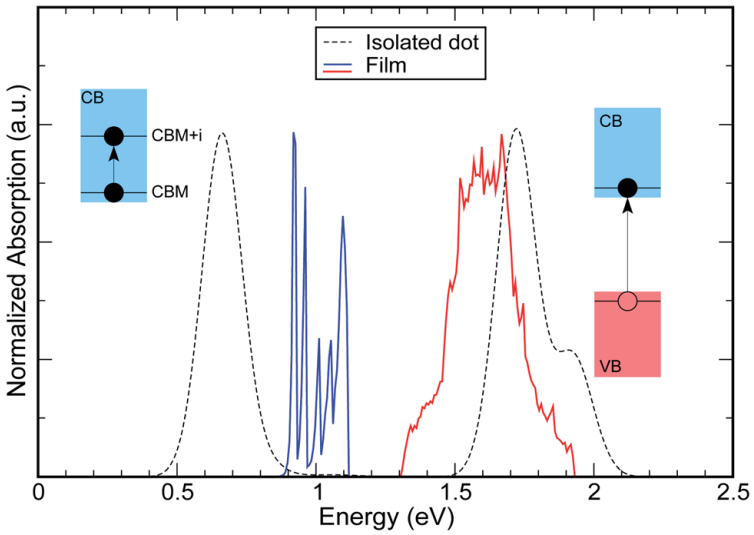

Figure 5.26: Comparison between isolated QD and the superlattice at minimum superlattice constant absorption curves for system A. The interband absorption (transitions across the gap) is included as the red curve along with the intraband (inside the conduction band) as the blue one. The dotted curves correspond with the absorptions of the isolated/diluted QD (including some peak broadening). It can be observed that while the absorptions investigated in this article (intraband) are blue shifted, the interband transitions are red shifted in accordance with the experimental data [119–122].

Absorption coefficient

We have calculated the absorption coefficient for two different temperatures and Fermi levels and 7 linear combinations of linear light polarization. Figures 5.27 and 5.28 show the absorption coefficient curves for the four systems at the two different temperatures and Fermi levels and all polarizations. The cases shown in these figures are superlattices with minimum dot-to-dot separation, i.e. 1 bond length (BL) $\approx$ 0.26 nm for systems A, B, D and 0.25 BL $\approx$ 0.05 nm for system C, due to inter-locking.

The temperatures we simulated are 77 K and 300 K. The former allows us to simulate a situation where the Fermi level governs occupation and the latter temperature allows us to study room temperature behaviour. We also chose two

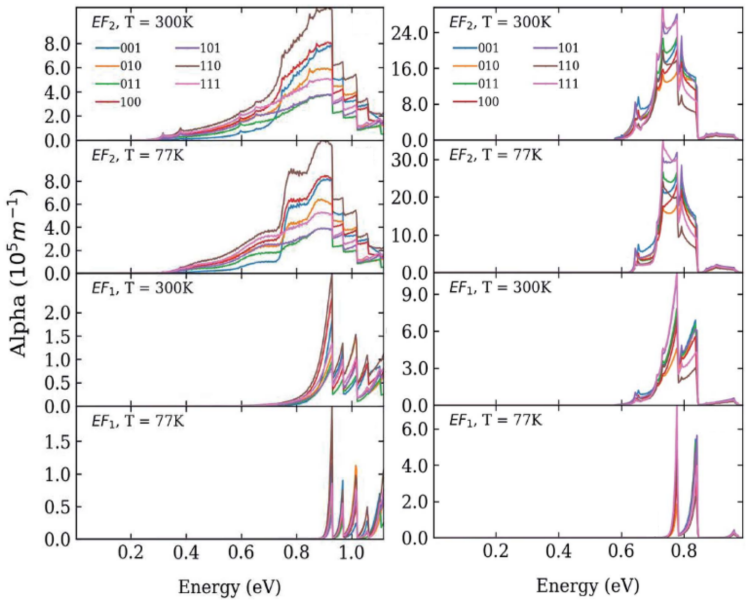

Figure 5.27: Absorption curves for superlattices made with system A (left panel) and system B (right panel) QDs at minimum dot-to-dot distance. There are four panels for the combination of the two Fermi levels (M_1 minimum and middle) and two temperatures (77 K and 300 K).

Fermi levels, EF_1 and EF_2. EF_1 is at the M_1 minima when the system has its lowest dot-to-dot separation i.e. minimum superlattice constant. And we used the same value with all dot-to-dot separations. We maintain this value across different superlattice constants. On the other hand, EF_2 is situated in the middle of M_1 and is changed as the minibands shift with changing dot-to-dot separations, to simulate a relatively similar doping level. The position of the Fermi level with respect to minibands in systems A and B is illustrated for clarification in figure 5.29. As shown in that figure, as the superlattice constant increases EF_1 penetrates deeper into the gap while EF_2 gets closer to the M_1 energy of the isolated QD.

When the dot-to-dot distance increases, the miniband structure flattens. This is due to a decrease in overlap between QD wavefunctions. The overlap integral and the first miniband M_1 width are represented for the four systems in

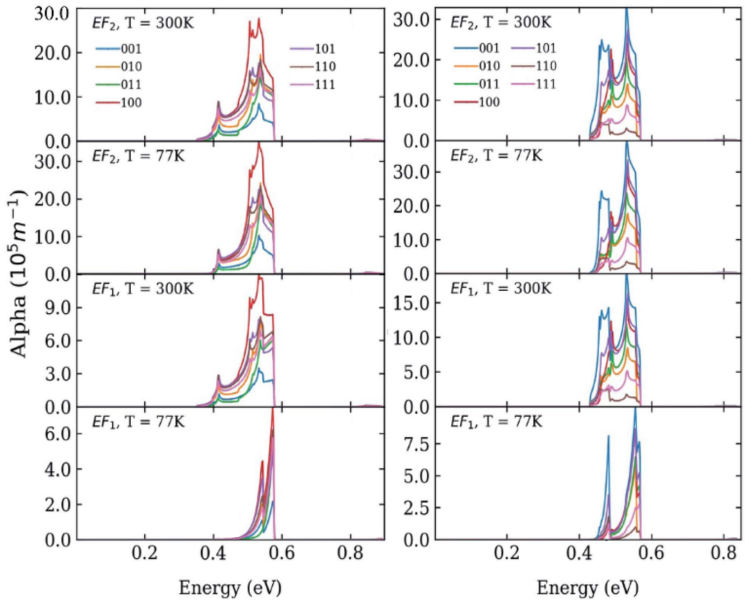

Figure 5.28: Absorption curves for superlattices made with system C (left panel) and system D (right panel) QDs at minimum dot-to-dot distance. There are four panels for the combination of the two Fermi levels (M_1 minimum and middle) and two temperatures (77 K and 300 K).

figure 5.30.

What follows is our findings in the system's behaviour with each of the changing parameters.

Light polarization

Absorption curve features show no dependence with light polarization. Figures 5.27 and 5.28 show the absorption for all light polarizations used in this paper. It can be seen that all the curves have roughly the same shape but different heights depending on polarization. Polarization does not change the absorption coefficient in more than an order of magnitude (our absorptions are between $10^5 \mathrm{m}^{-1}$ - $10^6 \mathrm{m}^{-1}$, in accordance with InAs/GaAs epitaxial QDs [123]). Light polarization affects differently depending on the system. For example,

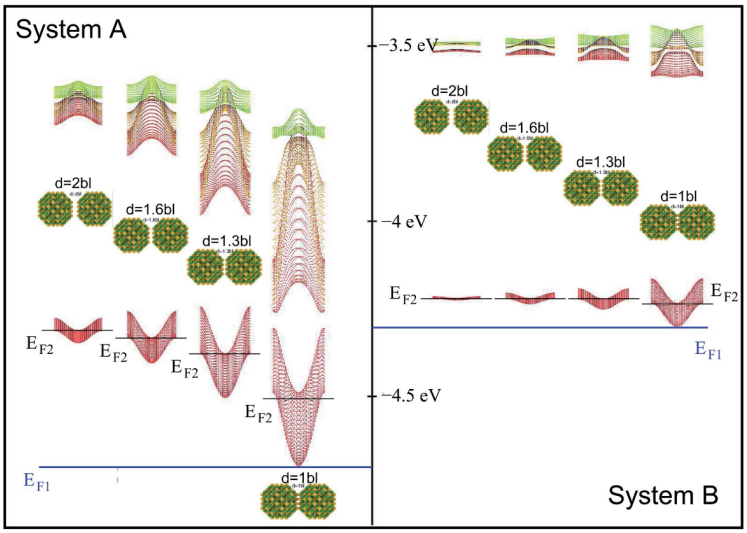

Figure 5.29: Illustration of the effects of superlattice constant i.e. dot-to-dot separation of the quantum dots A (left panel) and B (right panel) over the miniband curvature and position. Fermi level is represented to better explain how their values change. It can be seen that while EF_1 is not varied and is maintained at the minimum of M_1 at minimum superlattice constant, EF_2 is shifted in order to be always placed at the middle of M_1.

light polarized along [110] shows the highest peak in system A, but produces the curve with minimum values in systems B and D.

Temperature and Fermi level

$EF = EF_1$ at low temperature (77 K): the only importantly populated states are the ones closest to the Γ point. In this case it is noticeable that the absorption peaks are located very closely to the energies shown in table 5.2. This is because the only transitions happening are from states near the centre of the first Brillouin zone.

$EF = EF_1$ at room temperature (300 K): The absorption peaks widen for system A and there is some change in the overall shape of the curve at systems B,C,D. In all four cases the temperature increase leads to occupation at states

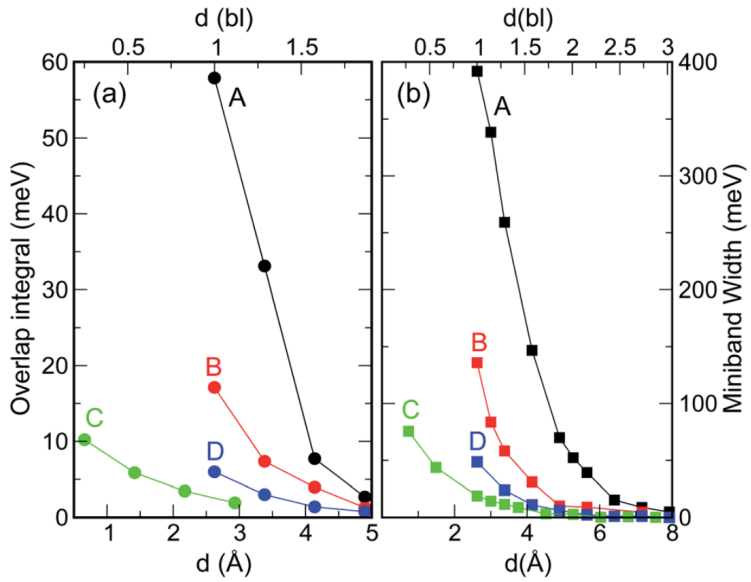

Figure 5.30: Overlap integral $\langle\psi_1(\mathbf{r})|V(\mathbf{r})|\psi_1(\mathbf{r}-\mathbf{R})\rangle$ change with dot-to-dot distance (left panel) and M_1 miniband width as a function of dot-to-dot separation (right panel). It can be shown in this figure the strong correlation between overlap and miniband width, as well as the steep changes that the superlattice constant produces to the system behaviour.

	Film				Isolated dot			
	A	B	C	D	A	B	C	D
$\Delta_{1\to2}$	930	779	545	483	648	706	470	475
$\Delta_{1\to3}$	969	838	576	558	669	726	502	506
$\Delta_{1\to4}$	1019	843	577	569	669	726	502	506
$\Delta_{1\to5}$	1060	961	892	828	815	880	815	814

Table 5.2: Energetic difference between minibands at the Γ point and energetic difference between the isolated QD states, all values are in meV.

with higher energy than the M_1 minimum. The flatter M_1 is, the further from the Γ point those states are. This means for system A that these newly occupied states are still very close to the centre of the Brillouin zone thus the absorption curves show no change in features, the peaks just widen and overlap some more. In systems B,C,D M_1 is flat enough as to produce new small absorption peaks because regions that are far from the Γ point take part in the absorption process and they have different absorption energies.

$EF = EF_2$ at low temperature (77 K): In this case, $EF2$ changes with the M_1 miniband position and curvature. Thus, the wider the miniband, the greater the observed change in absorption. System A is the most affected by the change in Fermi energy. It can be observed that with this Fermi energy level absorption peaks are all at lower energies with respect the dominant peaks at EF_1 and low temperature, because of the opposing curvatures of M_1 and the rest of the miniband structure.

$EF = EF_2$ at room temperature (300 K): Due to the fact that the Fermi level is in the middle of the miniband the systems with flat minibands have all their states participating in the absorption process. Temperature change has little effect, since all the M_1 states are highly occupied and since M_1 is far energetically from the rest of the miniband structures, the other minibands are highly unoccupied thus the occupation difference is very similar. However for system A, there is room for occupation to be affected by temperature and a dependence with temperature can be observed in this case.

In conclusion, all systems are more affected by the Fermi level than temperature. Both Fermi level and temperature have greater impact on results the lower the other parameter is. As a rule of thumb, temperature affects the flatter the minibands are (or the lower the overlaps) and Fermi level has a greater effect when minibands are wider.

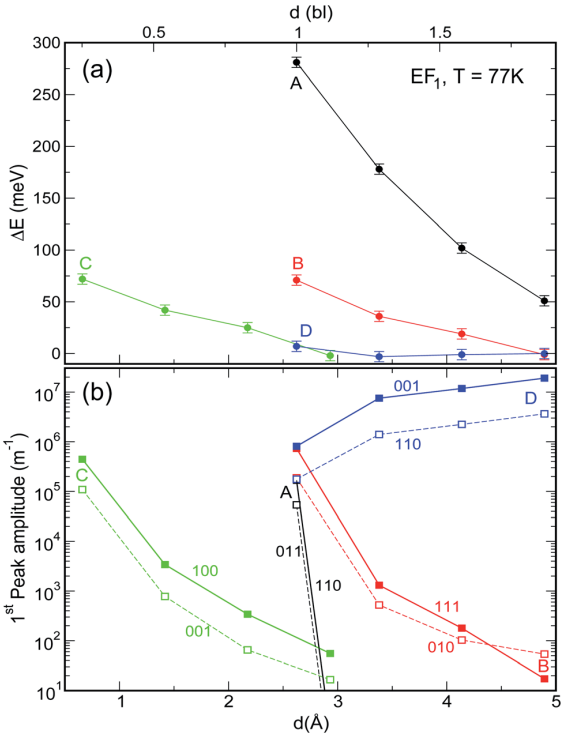

Figure 5.31: Energetic difference between M_1 and M_2 along the Γ point as a function of inter-dot separation (upper panel) and absorption peak maxima for the same inter-dot separation for polarizations producing highest and lowest absorption peaks (lower panel).

Inter-dot distance

The dot-to-dot distance affects primarily to the wavefunction overlaps, which in turn affect the miniband width and position. Figure 5.31 shows the dependency of minibands width and absorption peak width on dot-to-dot separation. The steepest curve is for system A, which suggests that the wider the miniband the stronger the effect.

The most noticeable effects when increasing the superlattice constant are i) the absorption values generally decrease if Fermi level remains unchanged,

because as the miniband flattens, the miniband energetic minimum increases and ii) the absorption spectrum is redshifted as the miniband position moves closer to the isolated QD energetic states.

Oscillator strength

The oscillator strength (equation 5.6) is a quantity that is proportional to the absorption and captures the dependency with the reciprocal vector and photon energy.

$$os = \frac{2m_0\omega}{\hbar K_{i\mathbf{q}} K_{f\mathbf{q}}} \left| \langle u_{f\mathbf{q}} | \, \hat{e} \, \mathbf{r} \, | u_{i\mathbf{q}} \rangle_\Omega \right|^2 \tag{5.6}$$

The oscillator strength is represented in figures 5.32 and 5.33. It can be seen that its average value changes slightly with light polarization (roughly the same change as in the absorption curves since the dependency with light polarization relies on the oscillator strength) but it is highly affected by superlattice constant, not only in its average value, but also changing the dependency on the reciprocal vector. When superlattice constant increases not only the minibands flatten and more reciprocal vectors participate in absorption but also their transition rates are higher. Therefore, there are two effects at play that make states in the Brillouin boundaries to participate in the absorption process i) enhanced occupation due to the proximity of the Fermi level and ii) higher oscillator strength at the Brillouin zone boundaries.

In figure 5.33 we show the oscillator strength for all transitions for system A. It can be seen that transitions $M_1 \rightarrow M_{2,3,4}$ are similar. This is due to the s-orbital nature of the first state and the p-orbital nature of the three next minibands, in accordance with the spherical symmetry of the QD. Transition from M_1 to the higher energy states (d-orbital) are much lower making high energy absorptions have lower absorption coefficient.

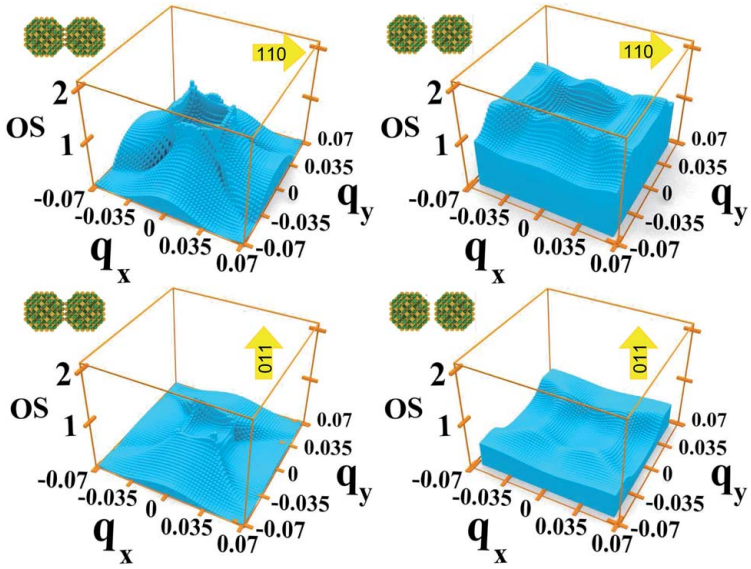

Figure 5.32: Oscillator strength for transitions M_1 to M_2 from system A, for all the **q** vectors of the Brillouin zone. For representational purposes the discretization has been reduced to 51×51. On the left panel the system has 1 bl separation between QDs and on the right one we have 2 bl separations. On the upper panel polarization is yielding maximum absorption, as opposed to the lower panel where we have minimum absorption. It can be seen, firstly, that the overall oscillator strength is higher for the 2 bl and, secondly, that the relative values between Γ point and Brillouin zone boundaries have changed, being the values close to the Γ point not so dominant for the 2 bl case.

5.5.3. Conclusions

We investigated the photon absorption characteristics and miniband structure of 2D superlattices of 4 different types of InAs QDs, varying superlattice constant, temperature, Fermi level, light polarization, surface stoichiometry and QD size. We found great blue shifts in the intraband transitions inside the conduction edge along with the usual red shift for transitions across the band gap. We found this effect to be independent of light polarization, which has less effect on absorption profile. Superlattice constant on the other hand, plays a significant role in the red and blue shifts, thus making possible to tune the absorption energies via lattice engineering. This might be done by choosing the right ligands.

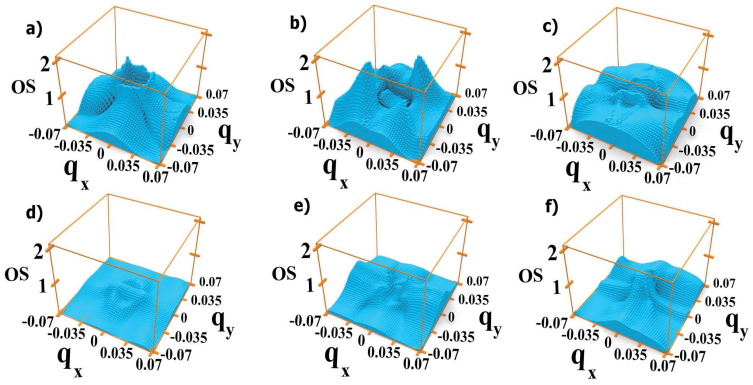

Figure 5.33: Oscillator strength for transition M_1 to M_2,M_3, M_4, M_5, M_6, M_7, for system A. It can be seen that for cases a), b) and c) (s→ p transitions) the oscillator strength is much higher than for cases d) e) and f) (pertaining to the s→ d) transitions.

5.6. Unpublished work

Our recently published work has been constrained to two-dimensional QD superlattices being one QD thickness (system d in figure 1.4). We have referred to these systems as 2D periodic superlattices. In this section we present other QD based device configurations that go beyond this scope. With the purpose to avoid any confusion, we refer to the description of the terminology used to refer these novel device configurations that was made on section 1.6.

The QD molecule and the 2D stack superlattice are two examples of systems that were possible to model by combining the periodic and finite tight binding models in section 2.1.2 and 2.1.3. There are many more combinations to cover that we decided to left out of our study because of the widespread possibilities of this research field.

The 1D and 3D configurations are used to study how finite systems behave when their structures grow and tend to their periodic counterparts. In the case of the QD stack, if the stack is made long enough, this should tend to behave as the 1D periodic system. For the 2D stack superlattice, if the stack is thick enough we should observe a behaviour that approaches the 3D periodic system.

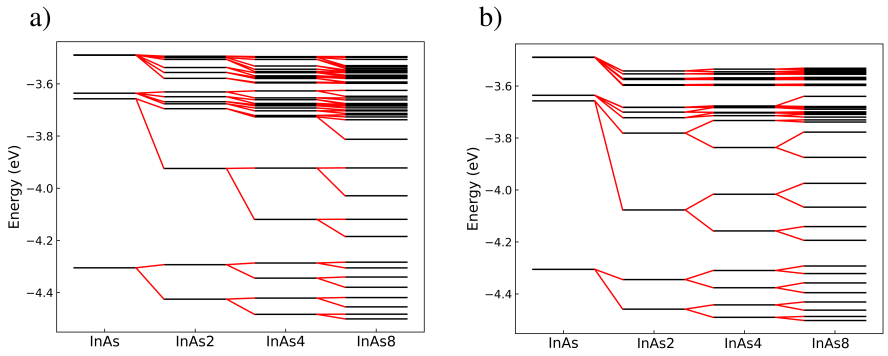

Figure 5.34: . Comparison between different stacks obtained for the two different approaches. a) The quantum dot stack energy spectrum for different numbers of QDs in the stack in the asymmetric approach (from 1 to 8 QDs in the stack) and b) the same example for the symmetric approach. We can see the energy hybridization when more QDs interact. It can be seen, comparing a) and b), that the two approaches yield similar, but differently distributed eigenergies. Energies are referred to vacuum level.

5.6.1. Current results

In this section we showcase the results we have obtained and the results that led us to the theoretical development of section 4.7. We start by the energetic description of the systems, using the energetic miniband structure where applicable.

When solving the finite tight binding Schrödinger equation for a molecule the resulting number of eigenstates is the same as the sum of eigenstates in the QD molecule constituents (e.g. a molecule of seven QDs using 8 eigenfunctions each would have $7 \times 8 = 56$ different eigenstates and eigenergies). In figure 5.34 we show how the energetic states evolve when increasing the number of QDs, compared to the isolated InAs QD. As said in chapter 1, we focused on one type of QD molecule arrangement which consists on stacking QDs along the z-axis.

There is an ongoing discussion about how to numerically model the QD stacks.

We use two different approaches.

- Asymmetric approach: A finite system, with its boundary effects.
- Symmetric approach: In this case we use a "virtual"quantum dot at the boundaries whose wavefunctions overlap with the real boundaries of the stack.

The two approaches handle the tight binding Hamiltonian in two distinct ways. In the first approach, we obtain the Hamiltonian matrix as in equation 2.12 and solve it directly, obtaining the corresponding eigenstates. In the second approach we introduce an intermediate step before solving the Hamiltonian. If we want to solve a stack of M quantum dots in the symmetric approach, we obtain the Hamiltonian matrix for a stack of $(M + 2)$ QDs, where two virtual quantum dots are added to the stack boundaries. Before solving the Hamiltonian we manipulate the matrices to eliminate the eigenstates of the two extra QDs, thus representing a system with M QDs. This will change the overlaps in the boundaries, because there are the effects of a virtual QD. We call it a virtual QD because it will not contribute to the stack spectrum adding extra eigenstates but will affect the original ones in terms of overlapping. In order to avoid the localized wavefunction states we took the decission to do the calculation using the latter approach. However the convenience of using the asymmetric or the symmetric approach is a subject that is currently under debate. Figure 5.35 illustrates the operation we performed. The figures show the component moduli of one of the Hamiltonian matrices (matrix A in equation 2.12).

The symmetric approach might be understood as the equivalent to molecular passivation. In regular passivation the QD dangling bonds are usually saturated by means of a surface hidrogen-like atom, removing highly reactive surface states which would result in unphysical results. In spite of the obvious differences between regular passivation and the symmetric approach, both procedures remove the surface states in the systems. Figure 5.34 shows how the energies of a passivated stack change with increasing QD number in the stack.

Both approaches are interesting. The symmetric approach was developed to

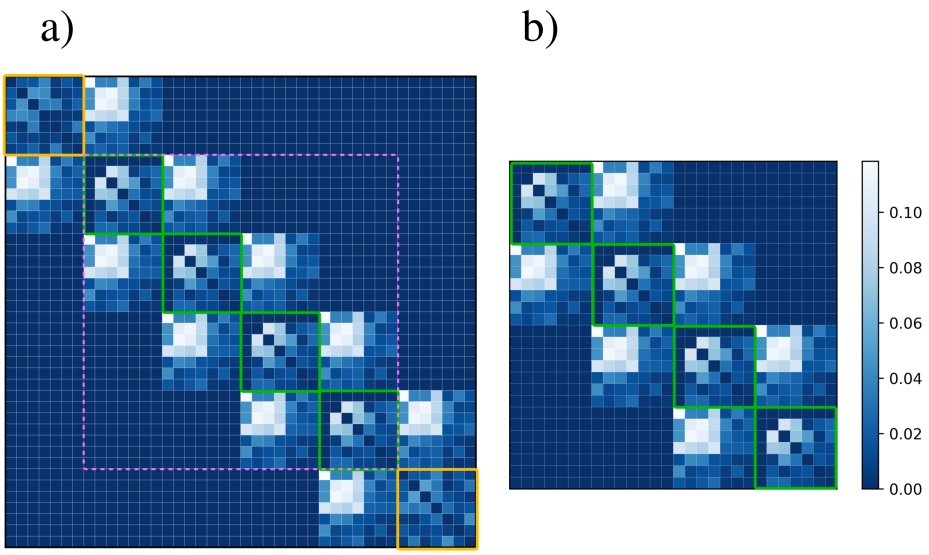

Figure 5.35: Visual representation of the Hamiltonian matrix for the antisymmetric and symmetric approaches. a) Hamiltonian representation of a 6 QD stack in the asymmetric approach and b) Hamiltonian representation of a 4 QD stack in the symmetric approach. Each plotted square is a numerical value of the Hamiltonian matrix A (equation 2.12) for a stack of six QDs, which has been turned to its modulus and coloured as a function of numerical value (the diagonal terms of the matrix have been turned to zero since these are much larger than the off-diagonal terms, thus blinding the numerical values of the rest of the matrix). It can be seen that the matrix is divided into patterns, which we call submatrices. Submatrices along the diagonal are sums of wavefunctions overlaps of a particular quantum dot in the stack. The off-diagonal submatrices are interactions between wavefunctions of different QDs. The submatrices form a tridiagonal system because of the nearest neighbours approximation. The diagonal consists on repeating submatrices. This periodicity is broken at the boundary QDs, since these quantum dots have overlapping from one side but there is no overlapping from the opposite.

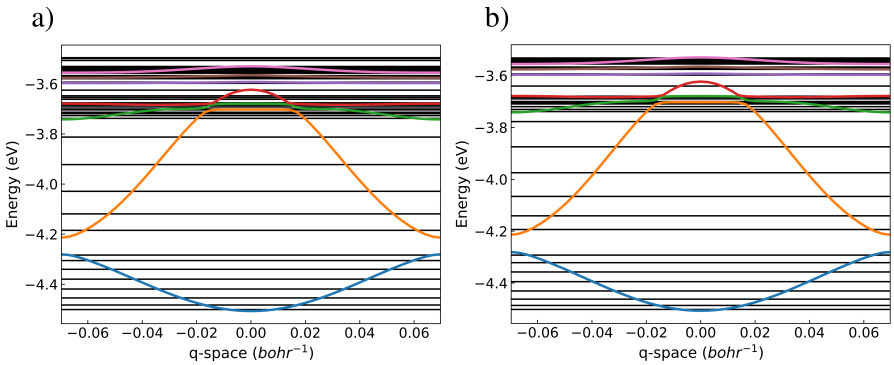

Figure 5.36: Comparison between stack energies and a 1D periodic system using InAs 12Å radius QD. Coloured lines represent the periodic system minibands and black lines represent the stack energy spectrum. We can see that in the asymmetric approach (a) the stack energies are greater than the maximum energies of the periodic system while in the symmetric approach (b) all stack energies lay inside the energetic width of the periodic system.

see if the low energy absorption peaks in 2D periodic stacks (discussed later in this chapter) were derived from the existence of boundary conditions at the stack. We ultimately saw that this was not the case (we understood the low energy peaks as shown in section 4.7) but when comparing 1D periodic system energies with the stacks (figure 5.36), the symmetric approach was more convincing in terms of eigenenergies and wavefunction behavior. Therefore we decided to use QD stacks in the symmetric approach framework throughout this investigation.

In order to calculate 2D periodic stacks we firstly obtain the stack eigenstates and then we use these as the unit cell of an otherwise regular 2D periodic system. This has a direct consequence in the miniband structure. If we solve a stack of M QDs using N wavefunctions per quantum dot we obtain a $M \times N$ dimension matrix to diagonalize eigenstates. This system, when used as the 2D periodic stack unit cell, yields a $M \times N$ miniband structure. These minibands are similar to the original N minibands of the 2D periodic array, as shown in figure 5.37, where we compare a 2D periodic InAs 12Å radius QD with a

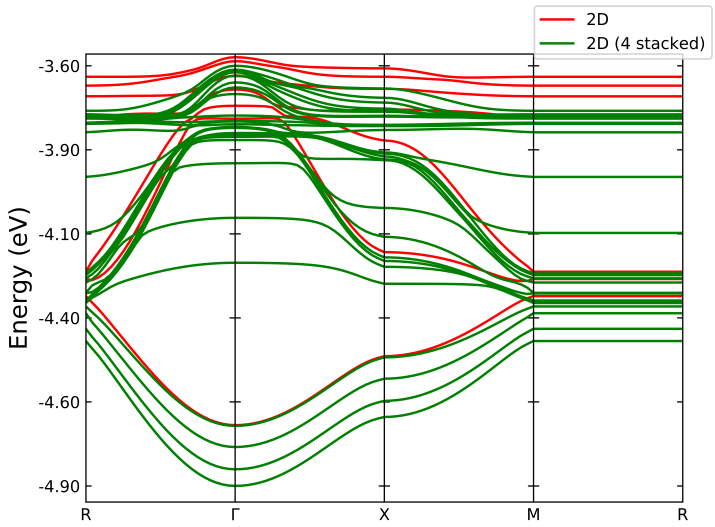

Figure 5.37: Miniband structure of 2D periodic InAs QDs R=12 Å (red) and 2D periodic stack of four InAs QDs R=12 Å (green). It is remarkable how the 2D periodic stack shares common features with the 2D periodic superlattice. In this chapter we maintain a consistent miniband structure representation, in which we choose the 3D reciprocal space to represent minibands (figure 2.2). The rightmost panel has flat minibands since it is representing states through q_z direction, in which the 2D structure has no periodicity.

periodic 2D stack of four QDs of the same material and radius. In both cases, all quantum dots are 1 bonding length from one another. The energetic distance between the 2D periodic stack minibands and the original 2D system depend on the overlapping quantities between QDs. In figure 5.38 we show the same system as in figure 5.37 but with the QDs moved away by 2.1 bohrs from each other along the perpendicular direction to the periodic plane (z-axis). This reduces overlap and makes the 2D stack minibands closer to the one QD thick 2D periodic system. In the limit where there is no overlap between QDs at the stack there would be a complete M-fold degeneracy. The physical interpretation would be the consideration of M independent 2D periodic, one QD thick systems.

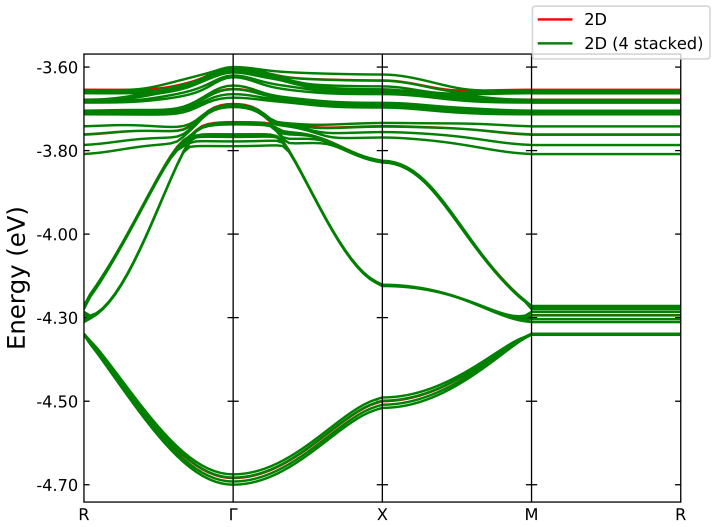

Figure 5.38: Miniband structure of 2D periodic InAs QDs (red) and 2D periodic stack of four InAs QDs taken apart 2.1 bohr (green). We can observe how the minibands derived from the stack get closer to the 2D periodic miniband structure.

5.6.2. Low energy absorption peaks at 2D periodic stacks

There has been a great effort of theoretical research along this work in order to explain the results we obtained when calculating the absorption coefficients. The most striking feature about the absorption coefficient calculations of the 2D periodic stacks is the large low energy absorption peak we found in every simulated system.

As it has been previously said, we thought that the existence of this peak would be due to the boundary effect of the stack. After discarding this possibility with the use of the symmetric approach, we observed no monotonous dependency with the peak height and the number of QDs in the stack. This is a problem since at a certain stack thickness we should observe a trend to the 3D behaviour. Lastly, the other striking property of these peaks is that they only appear when light polarization is along the z-axis.

We scrutinized the periodic system absorption formalism and developed the theory explained in section 4.7. We arrived to the conclusion that the low energy peak approaches to a Dirac delta around zero photon energy, which is equivalent to say that it vanishes when N tends to infinity. Nonetheless in our simulation calculations it is visible for any number of QDs stack. This is because we use a histogram to represent the absorption coefficient along the available energies on the Q_s discrete space. Thus, the lowermost bin of the histogram contains this low energy peak.

This peak, nonetheless, is present, specially in small thickness 2D periodic stacks. We suggest that the measurement of these low energy peaks can be used by experimentalists to obtain insights on the coupling between layers of a 2D stack superlattice. This will be the topic of future works on this research line.

Firstly, for comparison purposes, figure 5.39 shows the absorption coefficient of a one InAs QD thick 2D periodic superlattice (no stacking). All lattices in this section are periodic (infinite) along the xy-plane, the interdot distance being one bond length. Separation along the perpendicular direction (z axis) may vary. The figure shows the absorption coefficient for light polarized along the three axis. Before starting our discussion, it is important to discuss on the coefficient unit dimensions, noted as $\tilde{\alpha}$ instead of the usual α. A 3D QD array has a well defined unit cell given by the interdot distance between neighbours. Nevertheless, as the system dimensionality reduces, some lengths are not well defined. For example 2D QD or 2D stack QD arrays have well defined unit cell sizes along the x and y directions because the interdot distances are well defined along these directions. However the unit cell size has no well defined length along the z direction. We could assume this length being the QD diameter, but there is no perfectly defined boundaries along that direction. In the same manner QD stacks and 1D QD arrays have no well defined cross section area. For this reason the next discussion has to be considered.

In a 2D system the absorption coefficient can be measured as the fraction

between emitted and transmitted light, I and I_0 respectively[93]:

$$\alpha L = \ln(\frac{I_0}{I}) \tag{5.7}$$

where L is the distance travelled by the light in the material. Assuming light travelling through the material along the z direction, L is the system thickness which is not well defined as it has been previously explained. With this in mind, we decided to modify the absorption coefficient formulation in equation 4.19. Instead of introducing the unit cell volume in the denominator, we used the unit cell surface in the xy plane (or the dot-to-dot distance in 1D arrays) which are well defined quantities. This yields a dimensionless absorption coefficient for 2D systems and a counter intuitive length dimension for 1D systems. Nevertheless, the absorption features remain unchanged.

In order to find a correspondence between the absorption coefficient values and experimental ones, the above factors should be considered.

Figure 5.40 shows the absorption coefficient obtained in a 2D periodic stack. It can be seen how the low energy absorption peak is much higher than the rest of the curve, yet we can see similar absorption quantities in the inset, which shows that this system, having greater thickness, absorbs more light than the one QD thick 2D periodic superlattice.

Finally, to demonstrate an important feature of our findings, we show in figure 5.41 a comparison between this 2D stack superlattice and one that has a greater separation between QDs along the stack (2.1 bohrs more than the other stack). We can observe that the low energy peak has decreased significantly, while the higher energy transitions have remained similar (it is even higher for the greater separation stack case). This can be explained by looking at equation 4.20. It can be seen that the bracket overlaps multiply the whole derivation. When QDs are taken apart in the stack, the overlaps reduce dramatically, reducing the peak by a similar amount. There is not a linear relationship between overlap and low energy peak value or position, since reducing overlap is done by moving the quantum

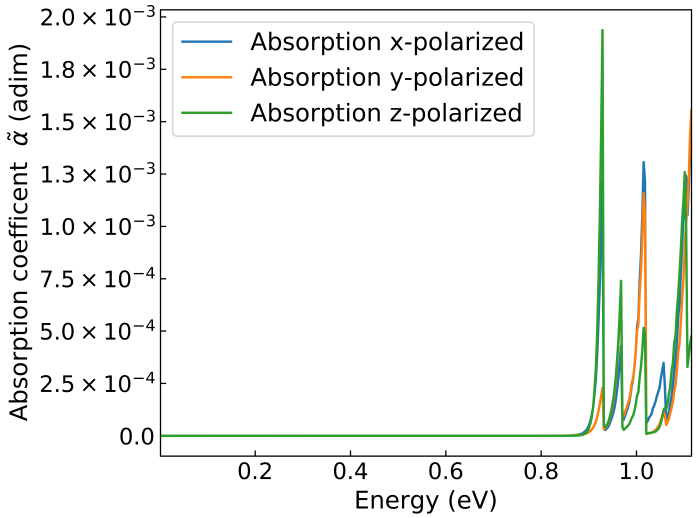

Figure 5.39: Absorption coefficient for a 2D superlattice without stacking for a periodic superlattice with one bond length dot-to-dot separation between InAs R=12Å QDs.

dots apart from each other, which in turn modifies **R** in the sum, changing the $F(\xi)$ and $E(\xi)$ in equation 4.21 has complex dynamics.

5.6.3. Conclusions

This unpublished work will shed some light on the dynamics of finite width superlattices (2D stack superlattices) of arbitrary stacks. For the sake of clarity we have summarized in this section the main results we obtained on this topic. There are many physical features that could be derived from a deeper study applying the obtained procedure to different materials, different crystalline structures and different QD arrangements.

We also predict a significant low energy peak that should be present in stacked QDs films, whose intensity hints the degree of coupling between film layers. More results about these systems are now on their way.

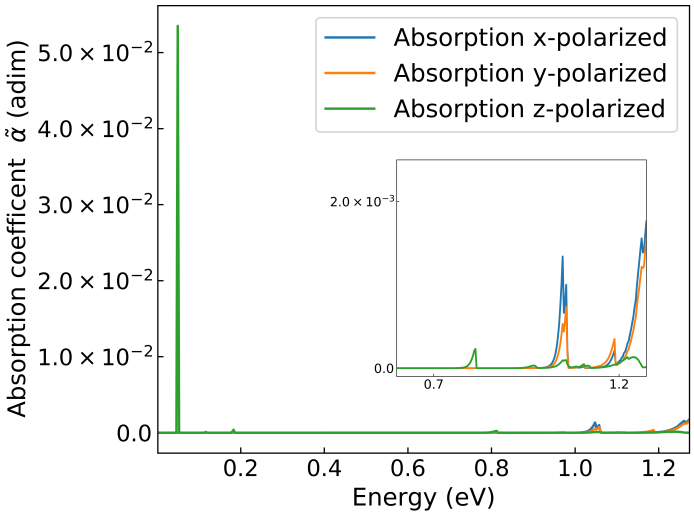

Figure 5.40: Absorption coefficient of a 2D stack superlattice made of stacks of 4 QDs. It can be observed a low energy peak for light polarized along z-direction. It can be seen that at higher energies (greater than the bandgap) $\tilde{\alpha}$ modified coefficient is of similar value than the 2D non stacked superlattice counterpart.

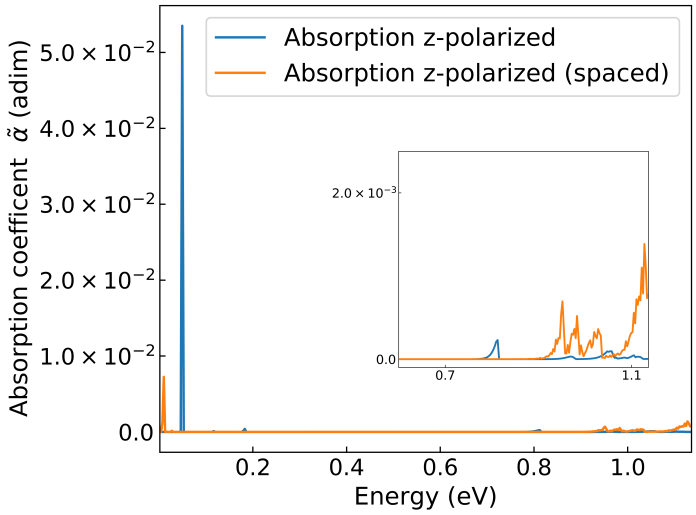

Figure 5.41: Absorption coefficient comparison between two 2D stack superlattices. Blue curve corresponds to a 2D stack superlattice whose layers are one bond length apart from another (minimum distance) while the orange curve corresponds to a 2D stack superlattice whose layers are separated by 2.1 bohrs, lowering the overlap between quantum dots. The superlattice constant (distance between QDs across the xy-plane) is the same. We can see how the low energy peak is reduced, due to the overlap decrease in equation 4.20

6

Conclusions

In this work we have investigated the optical absorption and electronic mobility for periodic quantum dot systems (superlattices), taking into account atomistic details of the quantum dots used. This allowed us to work with a wide variety of system parameters such as QD radius, chemical compounds and surface traps.

In order to do this, our methodology was divided into three basic steps: i) Isolated QD empirical pseudopotential calculation ii) use of tight binding formalism to calculate the properties of a periodic array (or QD molecule) of a particular QD as shown in chapter 2 and iii) electronic mobility/photon absorption calculation using the methodology explained in chapters 3 and 4.

We explained the two different approaches of the tight binding method we used in this work, mainly the periodic and non-periodic ones. The periodic is used to calculate properties such as energy dispersion (minibands) for the QD arrays while the non-periodic is used to calculate the properties of QD molecules. In the latter case, we used the periodic approach after the non-periodic one, to calculate a periodic array made of QD molecules. We called this the 2D periodic stack. There is a vast number of configurations we can study with this research, and we had to limit ourselves to the 2D periodic stack, leaving other configurations, such as the 1D periodic stack (or QD nanoribbon) for future work.

We shown a novel approach in which we use Markov chains instead of the computationally more expensive Monte Carlo approach to calculate electric mobility in QD periodic arrays. The limiting factor of electric mobility in this work was assumed to be size dispersion. We assumed a perfectly periodic QD array that is disturbed by the presence of differently sized QDs which we call impurities, in analogy with semiconductor crystals. During this work we have calculated electronic mobility values as a function of QD chemistry, morphology, size (for both periodic and impurity QDs) superlattice constant, Fermi level and temperature. We concluded that our model is suited as a complementary tool to the better known hopping model, in the sense that when QD arrays are sufficiently ordered, our model follows the real data better than the hopping

model, and vice versa for highly disordered QD arrays. We developed our model to the point where experimental researchers can use it as a hint to the size distribution in their fabricated device, from macroscopic measurements such as mobility dependence with temperature.

In the case of photon absorption, our theoretical approach was the semiclassical approximation. We have made a thorough study across the same physical properties than in the mobility case i.e. QD chemistry, morphology, size, array lattice constant, Fermi level and temperature. Nevertheless, in this study we found a very unusual photon absorption result which, deemed as a simulation bug, turned out to be a mathematically explainable phenomenon in the semiclassical approximation when some assumptions on orthogonality are dropped. These results are yet to be published.

To summarize, in this work we have developed a theoretical and computational toolkit that will allow us to guide the experimental effort in the high quality, highly ordered QD devices paradigm shift in the years to come.

Bibliography

[1] Nrel efficiency chart 2020. *https://www.nrel.gov/pv/cell-efficiency.html*.

[2] Sergey B Brichkin and Vladimir F Razumov. Colloidal quantum dots : synthesis , properties and applications. *Russian Chemical Reviews*, 85(12):1297–1312, 2016.

[3] Ji Hyuk Choi, Aaron T Fafarman, Soong Ju Oh, Dong Kyun Ko, David K Kim, Benjamin T Diroll, Shin Muramoto, J Greg Gillen, Christopher B Murray, and Cherie R Kagan. Bandlike transport in strongly coupled and doped quantum dot solids: A route to high-performance thin-film electronics. *Nano Letters*, 12(5):2631–2638, 2012.

[4] Jong-Soo Lee, Maksym V Kovalenko, Jing Huang, Dae Sung Chung, and Dmitri V Talapin. Band-like transport, high electron mobility and high photoconductivity in all-inorganic nanocrystal arrays. *Nature Nanotechnology*, 6:348–352, 2011.

[5] S Bednarek, B Szafran, and J Adamowski. Many-electron artificial atoms. *Physical Review B*, 59(20):36–42, 1999.

[6] J.M. Gérard and B. Gayral. InAs quantum dots : artificial atoms for solid-state cavity-quantum electrodynamics. *Physica E*, 9:131–139, 2001.

[7] Gert Schedelbeck, Werner Wegscheider, Max Bichler, and Gerhard Abstreiter. Coupled Quantum Dots Fabricated by Cleaved Edge Overgrowth: From Artificial Atoms to Molecules. *Science*, 278, 1997.

[8] Heather Goodwin, Tom C Jellicoe, Nathaniel J L K Davis, and Marcus L Böhm. Review article Multiple exciton generation in quantum dot-based solar cells. *Nanophotonics*, 7(1):111–126, 2018.

[9] Jun-wei Luo, Alberto Franceschetti, and Alex Zunger. Quantum-size-induced electronic transitions in quantum dots : Indirect band-gap GaAs. *Physical Review B*, 78(035306), 2008.

[10] Dong Ick Son, Byoung Wook Kwon, Dong Hee Park, Won-seon Seo, Yeonjin Yi, Basavaraj Angadi, Chang-Lyoul Lee, and Won Kook Choi. Emissive ZnO–graphene quantum dots for white-light-emitting diodes. *Nature Nanotechnology*, 15(1):565–573, 2012.

[11] Cherie R. Kagan, Efrat Lifshitz, Edward H. Sargent, and Dmitri V. Talapin. Building devices from colloidal quantum dots. 353(6302):885–894, 2016.

[12] Remi Beaulac, Paul I Archer, Stefan T Ochsenbein, and Daniel R Gamelin. Mn 2+ -Doped CdSe Quantum Dots : New Inorganic Materials for Spin-Electronics and Spin-Photonics. *Advanced Functional Materials*, 18:3873–3891, 2008.

[13] Yue Wang, Xiaoming Li, Jizhong Song, Lian Xiao, Haibo Zeng, and Handong Sun. All-Inorganic Colloidal Perovskite Quantum Dots : A New Class of Lasing Materials with Favorable Characteristics. *Advanced Materials*, 27:7101–7108, 2015.

[14] Debasis Bera, Lei Qian, Teng Kuan Tseng, and Paul H. Holloway. Quantum dots and their multimodal applications: A review. *Materials*, 3(4):2260–2345, 2010.

[15] D Vasudevan, Rohit Ranganathan Gaddam, Adrian Trinchi, and Ivan Cole. Core-Shell Quantum Dots: Properties and Applications. *Journal of Alloys and Compounds*, 636(5):395–404, 2015.

[16] Aaron Tan, Lara Yildirimer, Jayakumar Rajadas, De La Peña Hugo, Giorgia Pastorin, and Alexander Seifalian. Quantum dots and carbon nanotubes in oncology : a review on emerging theranostic applications in nanomedicine. *Nanomedicine*, 6(6):1101–1114, 2011.

[17] Jinhao Gao, Kai Chen, Renguo Xie, Jin Xie, Seulki Lee, Zhen Cheng, Xiaogang Peng, and Xiaoyuan Chen. Ultrasmall Near-Infrared Non-cadmium Quantum Dots for in vivo Tumor Imaging. *NanoMicroSmall*, 6(2):256–261, 2010.

[18] Vilius Poderys, Marija Matulionyte, Algirdas Selskis, and Ricardas Rotomskis. Interaction of Water-Soluble CdTe Quantum Dots with Bovine Serum Albumin. *Nanoscale Research Letters*, 6(9):256–261, 2011.

[19] Pavel Zrazhevskiy, Mark Sena, and Xiaohu Gao. Designing multifunctional quantum dots for bioimaging , detection , and drug delivery. *Chem. Soc. Rev.*, 39:4326–4354, 2010.

[20] N Jones Cody, Rodney Van Meter, Austin G Fowler, Peter L Mcmahon, Jungsang Kim, Thaddeus D Ladd, and Yoshihisa Yamamoto. Layered Architecture for Quantum Computing. *Phys. Rev. X*, 2(3):2160–3308, 2012.

[21] Christoph Kloeffel and Daniel Loss. Prospects for Spin-Based Quantum Computing in Quantum Dots. *Condens. Matter Phys.*, 4:51–58, 2013.

[22] M Veldhorst, H G J Eenink, C H Yang, and A S Dzurak. Silicon CMOS architecture for a spin-based quantum computer. *Nature Communications*, 8(1):1766, 2017.

[23] Yue Wang, Van Duong Ta, Kheng Swee Leck, Hau Tan, Zeng Wang, Tingchao He, Claus-Dieter Ohl, Hilmi Volkan Demir, and Handong Sun. Robust whispering-gallery-mode microbubble lasers from colloidal quantum dots. *Nano Letters*, 17(4):2640–2646, 2017.

[24] Kenichi Nishi, Keizo Takemasa, Mitsuru Sugawara, and Yasuhiko Arakawa. Development of Quantum Dot Lasers for Data- Com and Silicon Photonics Applications. *IEEE Journal of Selected Topics in Quantum Electronics*, 23(6):1–7, 2017.

[25] Alan Y. Liu, Jon Peters, Xue HUANG, Daehwan Jung, Justin Norman, Minjoo L. Lee, Arthur C. Gossard, and John E. Bowers. Electrically pumped continuous-wave 1.3 μ m quantum-dot lasers epitaxially grown on on-axis (001) GaP / Si. *Optics Letters*, 42(2):338–341, 2017.

[26] Yuchang Wu and Levon V. Asryan. Theory of photovoltaic characteristics of semiconductor quantum dot solar cells. *Journal of Applied Physics*, 120(084302), 2016.

[27] Sandeep Kumar, Monika Nehra, Akash Deep, Deepak Kedia, Neeraj Dilbaghi, and Ki Hyun Kim. Quantum-sized nanomaterials for solar cell applications. *Renewable and Sustainable Energy Reviews*, 73:821–839, 2017.

[28] Arthur J Nozik. Next Generation Photovoltaics Based on Multiple Exciton Generation in Quantum Dot Solar Cells. In *Next Generation of Photovoltaics*, chapter 7, pages 191–207. 2012.

[29] Zhenyu Yang, James Z. Fan, Andrew H. Proppe, F. Pelayo García De Arquer, David Rossouw, Oleksandr Voznyy, Xinzheng Lan, Min Liu, Grant Walters, Rafael Quintero-Bermudez, Bin Sun, Sjoerd Hoogland, Gianluigi A. Botton, Shana O. Kelley, and Edward H. Sargent. Mixed-quantum-dot solar cells. *Nature Communications*, 8(1325), 2017.

[30] A J Nozik, M C Beard, J M Luther, M Law, R J Ellingson, and J C Johnson. Semiconductor quantum dots and quantum dot arrays and applications of multiple exciton generation to third-generation photovoltaic solar cells. *Chemical Reviews*, 110(11):6873–6890, 2010.

[31] Zhijun Ning, Yuan Ren, Sjoerd Hoogland, Oleksandr Voznyy, Larissa Levina, Philipp Stadler, Xinzheng Lan, David Zhitomirsky, and Edward H. Sargent. All-inorganic colloidal quantum dot photovoltaics employing solution-phase halide passivation. *Advanced Materials*, 24:6295–6299, 2012.

[32] Xinzheng Lan, Silvia Masala, and Edward H Sargent. Charge-extraction strategies for colloidal quantum dot photovoltaics. *Nature materials*, 13:233–240, 2014.

[33] Octavi E. Semonin, Joseph M. Luther, and Matthew C. Beard. Quantum dots for next-generation photovoltaics. *Materials Today*, 15(11):508–515, 2012.

[34] Mengmeng Hao, Yang Bai, Stefan Zeiske, Long Ren, Junxian Liu, Yongbo Yuan, Nasim Zarrabi, Ningyan Cheng, Mehri Ghasemi, Peng Chen, Miaoqiang Lyu, Dongxu He, Jung-ho Yun, Yi Du, Yun Wang, Shanshan Ding, Ardalan Armin, Paul Meredith, Gang Liu, Hui-ming Cheng, and Lianzhou Wang. Ligand-assisted cation-exchange engineering for high-efficiency colloidal Cs1-x FAxPbI3 quantum dot solar cells with reduced phase segregation. *Nature Energy*, 5:79–88, 2020.

[35] Jiang Tang, Kyle W Kemp, Sjoerd Hoogland, Kwang S Jeong, Huan Liu, Larissa Levina, Melissa Furukawa, Xihua Wang, Ratan Debnath, Dongkyu Cha, Kang Wei Chou, Armin Fischer, Aram Amassian, John B Asbury, and Edward H Sargent. Colloidal-quantum-dot photovoltaics using atomic-ligand passivation. *Nature Materials*, 10:765–771, 2011.

[36] Kusum Kumari, Umesh Kumar, Shailesh N Sharma, Suresh Chand, Rita Kakkar, V D Vankdar, and Vikram Kumar. Effect of surface passivating ligand on structural and optoelectronic properties of polymer: CdSe quantum dot composites. *Journal of Physics D*, 41:235409, 2008.

[37] Gabriel Bester. Excitations in Nanostructures An Empirical Electronic Excitations in Nanostructures. *Journal of Physics, Condensed Matter*, 21(2):40–74, 2008.

[38] David Vanderbilt. Optimally smooth norm-conserving pseudopotentials. *Physical Review B*, 32(12), 1985.

[39] G P Kerker. Non-singular atomic pseudopotentials for solid state applications. *Journal of Physics C*, 13(94):189–194, 1980.

[40] David Vanderbilt. Soft self-consistent pseudopotentials in a generalized eigenvalue formalism. *Physical Review B*, 41(11):7892–7895, 1990.

[41] N. Troullier and Jose Luís Martins. A straight forward method for generating soft transferable pseudopotentials. *Solid State Communications*, 74(7):613–616, 1990.

[42] D.R. Hamman, M. Schlüter, and C. Chiang. Norm-conserving pseudopotentials. *Physical Review Letters*, 43(20):1494–1497, 1979.

[43] A Canning, L W Wang, A Williamson, and A Zunger. Parallel Empirical Pseudopotential Electronic Structure Calculations for Million Atom Systems. *Journal of Computational Physics*, 160:29–41, 2000.

[44] Christof Vömel, Stanimire Z. Tomov, Osni A. Marques, Lin-Wang Wang, and Jack J Dongarra. State-of-the-art eigensolvers for electronic structure calculations of large scale nano-systems. *Journal of Computational Physics*, 227:7113–7124, 2008.

[45] Lin-wang Wang and Alex Zunger. Pseudopotential calculations of nanoscale CdSe quantum dots. *Physical Review B*, 53(15):9579–9582, 1996.

[46] A. Franceschetti, H. Fu, L. W. Wang, and Alex Zunger. Many-body pseudopotential theory of excitons in InP and CdSe quantum dots. *Physical Review B*, 60(3):1819–1829, 1999.

[47] C B Murray, C R Kagan, and M G Bawendi. Self-Organization of CdSe Nanocrystallites into Three-Dimensional Quantum Dot Superlattices. *Science*, 270(5240):1335–1338, 1995.

[48] Hoi Chun Po, Liujun Zou, T Senthil, and Ashvin Vishwanath. Faithful tight-binding models and fragile topology of magic-angle bilayer graphene. *Physical Review B*, 99:195455, 2019.

[49] A N Rudenko, Shengjun Yuan, and M I Katsnelson. Toward a realistic description of multilayer black phosphorus : From GW approximation to large-scale tight-binding simulations. *Physical Review B*, 92:085419, 2015.

[50] Mark J Ablowitz and Justin T Cole. Tight-binding methods for general longitudinally driven photonic lattices : Edge states and solitons. *Physical Review A*, 96:043868, 2017.

[51] Neil W Ashcroft, N David Mermin, et al. Solid state physics [by] neil w. ashcroft [and] n. david mermin., 1976.

[52] Jim Napolitano and J.J. Sakurai. *MODERN QUANTUM MECHANICS*. Pearson, 2011.

[53] B.H. Bransden and C.J. Joachain. *Quantum Mechanics*. Pearson, 2000.

[54] R.M. Hill. Variable-Range Hopping. *physica status solidi*, 601(34):601–613, 1976.

[55] N Apsley and H P Hughes. Temperature and field-dependence of hopping conduction in disordered systems. *The philosophical magazine*, 30(5):963–972, 1974.

[56] Hugo E Romero and Marija Drndic. Coulomb Blockade and Hopping Conduction in PbSe Quantum Dots. *Physical Review Letters*, 95:156801, 2005.

[57] A. L. Efros and B.I. Shklovskii. Percolation theory and conductivity of strongly inhomogeneous media. *Soviet Physics*, 18:845–862, 1975.

[58] A. L. Efros and B.I. Shklovskii. Coulomb gap and low temperature conductivity of disordered systems. *Journal of Physics C*, 8:49–51, 1975.

[59] Yu. N. Gartsein and E.M. Conwell. High-field hopping mobility in molecular systems with spatially correlated energetic disorder. *Chemical Physics Letters*, 245(4-5):351–358, 1995.

[60] Yu. N. Gartstein and E. M. Conwell. Off-diagonal disorder activation energy of high-field hopping motion. *Physical Review B*, 51(11):6947–6952, 1995.

[61] S. V. Novikov and A. V. Vannikov. Hopping Charge Transport in Disordered Organic Materials : Where Is the Disorder ? *Journal of Physical Chemistry C*, 113(6):2532–2540, 2009.

[62] I I Fishchuk, A Kadashchuk, S T Hoffmann, S Athanasopoulos, J Genoe, H. Bässler, and A. Köhler. Unified description for hopping transport in organic semiconductors including both energetic disorder and polaronic contributions. *Physical Review B*, 88(12):125202, 2013.

[63] Thomas B Schrøder and Jeppe C Dyre. ac Hopping Conduction at Extreme Disorder Takes Place on the Percolating Cluster. *Physical Review Letters*, 88:125202, 2008.

[64] Philippe Guyot-sionnest. Electrical Transport in Colloidal Quantum Dot Films. *Journal of Physical Chemistry Letters*, 3(9):1169–1175, 2012.

[65] Francisco M. Gómez-Campos, Salvador Rodríguez-Bolívar, Erik S. Skibinsky-Gitlin, and Marco Califano. Efficient, non-stochastic, Monte-Carlo-like-accurate method for the calculation of the temperature-dependent mobility in nanocrystal films. *Nanoscale*, 10(20):9679–9690, 2018.

[66] Kun Huang. Temperature dependence of the low-field mobility of miniband conduction in superlattices. *Physical Review B*, 45(24):14404–14406, 1992.

[67] Daeha Joung, Lei Zhai, and Saiful I Khondaker. Coulomb blockade and hopping conduction in graphene quantum dots array. *Physical Review B*, 83:115323, 2011.

[68] Heng Liu, Alexandre Pourret, and Philippe Guyot-Sionnest. Mott and Efros-Shklovskii Variable Range Hopping in CdSe Quantum Dots Films. *ACS Nano*, 4(9):5211–5216, 2010.

[69] Andrew Shabaev, Alexander L Efros, and Alexei L Efros. Dark and Photo-Conductivity in Ordered Array of Nanocrystals. *Nano Letters*, 13(11):5454–5461, 2013.

[70] Prashant Nagpal and Victor I Klimov. Role of mid-gap states in charge transport and photoconductivity in semiconductor nanocrystal films. *Nature Communications*, 2:486–493, 2011.

[71] Brian Skinner, Tianran Chen, and B I Shklovskii. Theory of hopping conduction in arrays of doped semiconductor nanocrystals. *Physical Review B*, 85:205316, 2012.

[72] J Urayama, T B Norris, J. Singh, and P. Bhattacharya. Observation of Phonon Bottleneck in Quantum Dot Electronic Relaxation. *Physical Review Letters*, 86(21):4930–4933, 2001.

[73] Olga L Lazarenkova and Alexander A Balandin. Electron and phonon energy spectra in a three-dimensional regimented quantum dot superlattice. *Physical Review B*, 66:245319, 2002.

[74] Shigeyasu Uno, Nobuya Mori, Kazuo Nakazato, Nobuyoshi Koshida, and Hiroshi Mizuta. Theoretical investigation of electron-phonon interaction in one-dimensional silicon quantum dot array interconnected with silicon oxide layers. *Physical Review B*, 72:035337, 2005.

[75] Erik S. Skibinsky-Gitlin, Salvador Rodríguez-Bolívar, M. Califano, and Francisco M. Gómez-Campos. Band-like electron transport in 2D quantum dot periodic lattices: the effect of realistic size distributions. *Physical Chemistry Chemical Physics*, 21:25872–25879, 2019.

[76] Marco Califano, Erik S. Skibinsky-Gitlin, Francisco M. Gómez-Campos, and Salvador Rodríguez-Bolívar. New strategies for colloidal-quantum-dot- based intermediate-band solar cells. *The Journal of Chemical Physics*, 151:154101, 2019.

[77] Yuri Suhov and Mark Kelbert. *Markov Chains: A Primer in Random Processes and thier Applications*. 2008.

[78] Pratim Biswas. Characterization of size , surface charge, and agglomeration state of nanoparticle dispersions for toxicological studies. *Journal of Nanoparticle Research*, 11:77–89, 2009.

[79] E Rodriguez, E Jimenez, G J Jacob, A A R Neves, C L Cesar, and L C Ã Barbosa. Fabrication and characterization of a PbTe quantum dots multilayer structure. *Physica E*, 26(1-4):361–365, 2005.

[80] Kunyuan Lu, Yongjie Wang, Zeke Liu, Lu Han, Guozheng Shi, Honghua Fang, Jun Chen, Xingchen Ye, Si Chen, Fan Yang, Artem G Shulga, Tian Wu, Mengfan Gu, Sijie Zhou, Jian Fan, Maria Antonietta Loi, and Wanli Ma. High-Efficiency PbS Quantum-Dot Solar Cells with Greatly Simplified Fabrication Processing via " Solvent-Curing ". *Advanced Materials*, 30(25):1707572, 2018.

[81] K. Tvrdy and P. V. Kamat. Quantum Dot Solar Cells. *Comprehensive Nanoscience and Technology*, 1-5:257–275, 2011.

[82] Ryan Kisslinger, Weidi Hua, and Karthik Shankar. Bulk heterojunction solar cells based on blends of conjugated polymers with ii-vi and iv-vi inorganic semiconductor quantum dots. *Polymers*, 9(2):1–29, 2017.

[83] Bowen Fu, Chong Deng, and Lin Yang. Efficiency Enhancement of Solid-State CuInS2 Quantum Dot-Sensitized Solar Cells by Improving the Charge Recombination. 14(198), 2019.

[84] Linlin Zhang, Zhenxiao Pan, Wei Wang, Jun Du, Zhenwei Ren, Qing Shen, and Xinhua Zhong. Copper deficient Zn-Cu-In-Se quantum dot sensitized solar cells for high efficiency. *Journal of Materials Chemistry A*, 4(40):21442–21451, 2017.

[85] Zhengguo Zhang, Chengwu Shi, Kai Lv, Chengfeng Ma, Guannan Xiao, and Lingling Ni. PT US CR. *Journal of Energy Chemistry*, 27(4):1214–1218, 2017.

[86] Zhengguo Zhang, Chengwu Shi, Guannan Xiao, Kai Lv, Chengfeng Ma, and Jiangyu Yue. All-solid-state quantum-dot-sensitized solar cells with compact PbS quantum-dot thin fi lms and TiO 2 nanorod arrays. *Ceramics International*, 43(13):10052–10056, 2017.

[87] Erik S Skibinsky-Gitlin, Salvador Rodríguez, Marco Califano, and Francisco M. Gómez-Campos. Optical properties of nanocrystal films: blue shifted transitions as signature of strong coupling. *Nanoscale Advances*, 2:384–393, 2019.

[88] Ali Imran, Jianliang Jiang, Deborah Eric, M Noaman Zahid, M Yousaf, and Z H Shah. Optical properties of InAs / GaAs quantum dot superlattice structures. *Results in Physics*, 9:297–302, 2018.

[89] Shigeo Asahi, Toshiyuki Kaizu, and Takashi Kita. Adiabatic two-step photoexcitation effects in intermediate-band solar cells with quantum dot-in-well structure. 9:7859, 2019.

[90] A. Martí, L. Cuadra, and A. Luque. Quantum dot intermediate band solar cell. pages 940–943, 2000.

[91] A Martí, N. López, E. Antolín, E. Cánivas, C. Stanley, C. Farmer, L. Cuadra, and A. Luque. Novel semiconductor solar cell structures : The quantum dot intermediate band solar cell. *Thin solid films*, 512:638–644, 2006.

[92] Zhiming M. Wang, Andreas Waag, Greg Salamo, Naoki Kishimoto, Stefano Bellucci, and Young June Park, editors. *Quantum Dot Solar Cells*. Number 15. Springer, 2014.

[93] L.H.J. Lajunen. *Spectrochemical analysis by atomic absorption and emission*. Royal Society of Chemistry, 1992.

[94] R. Fitzpatrick. *Quantum Mechanics: A graduate level course*. 2006.

[95] Antonio Luque, Antonio Martí, and Colin Stanley. Understanding intermediate-band solar cells. *Nature Photonics*, 6(3):146–152, 2012.

[96] Akshay Krishna and Jacob J. Krich. Increasing efficiency in intermediate band solar cells with overlapping absorptions. *Journal of Optics*, 18:1–7, 2016.

[97] Stephen P. Bremner, Michael Y. Levy, and Christiana B. Honsberg. Limiting efficiency of an intermediate band solar cell under a terrestrial spectrum. *Applied Physics Letters*, 92(171110), 2008.

[98] Giulia Galli, Gergely T. Zimanyi, United States, Molecular Engineering, United States, United States, Márton Vörös, Giulia Galli, and Gergely T. Zimanyi. Colloidal Nanoparticles for Intermediate Band Solar Cells. *ACS Nano*, 9(7):6882–6890, 2015.

[99] Dong Kyun Ko, Patrick R. Brown, Moungi G. Bawendi, and Vladimir Bulovic. P-i-n heterojunction solar cells with a colloidal quantum-dot absorber layer. *Advanced Materials*, 26(28):4845–4850, 2014.

[100] Haiming Zhu, Ye Yang, Kim Hyeon-Deuk, Marco Califano, Nianhui Song, Youwei Wang, Wenqing Zhang, Oleg V. Prezhdo, and Tianquan Lian. Auger-assisted electron transfer from photoexcited semiconductor quantum dots. *Nano Letters*, 14:1263–1269, 2014.

[101] Richard D. Schaller, Jeffrey M. Pietryga, and Victor I. Klimov. Carrier multiplication in InAs nanocrystal quantum dots with an onset defined by the energy conservation limit. *Nano Letters*, 7(11):3469–3476, 2007.

[102] James W.M. Chon, Min Gu, Craig Bullen, and Paul Mulvaney. Three-photon excited band edge and trap emission of CdS semiconductor nanocrystals. *Applied Physics Letters*, 84(22):4472–4474, 2004.

[103] David R. Baker and Prashant V. Kamat. Tuning the emission of CdSe quantum dots by controlled trap enhancement. *Langmuir*, 26(13):11272–11276, 2010.

[104] Christy F. Landes, Markus Braun, and Mostafa A. El-Sayed. On the nanoparticle to molecular size transition: Fluorescence quenching studies. *Journal of Physical Chemistry B*, 105(43):10554–10558, 2001.

[105] Francisco M. Gómez-Campos, Salvador Rodríguez-Bolívar, and Marco Califano. High-Mobility Toolkit for Quantum Dot Films. *ACS Photonics*, 3(11):2059–2067, 2016.

[106] Deniz Bozyigit, Weyde M.M. Lin, Nuri Yazdani, Olesya Yarema, and Vanessa Wood. A quantitative model for charge carrier transport, trapping and recombination in nanocrystal-based solar cells. *Nature Communications*, 6(6180), 2015.

[107] Iwan Moreels, Karel Lambert, David De Muynck, Frank Vanhaecke, Dirk Poelman, José C. Martins, Guy Allan, and Zeger Hens. Composition and size-dependent extinction coefficient of colloidal PbSe quantum dots. *Chemistry of Materials*, 19(25):6101–6106, 2007.

[108] Ludovico Cademartiri, Erica Montanari, Gianluca Calestani, Andrea Migliori, Antonietta Guagliardi, and Geoffrey A. Ozin. Size-dependent extinction coefficients of PbS quantum dots. *Journal of the American Chemical Society*, 128(31):10337–10346, 2006.

[109] W. William Yu, Lianhua Qu, Wenzhuo Guo, and Xiaogang Peng. Experimental determination of the extinction coefficient of CdTe, CdSe, and CdS nanocrystals. *Chemistry of Materials*, 15(14):2854–2860, 2003.

[110] Pingrong Yu, Matthew C. Beard, Randy J. Ellingson, Suzanne Fernere, Calvin Curtis, John Drexler, Fred Luiszer, and Arthur J. Nozik. Absorption cross-section and related optical properties of colloidal InAs quantum dots. *Journal of Physical Chemistry B*, 109(15):7084–7087, 2005.

[111] T. Vossmeyer, L. Katsikas, M. Giersig, I. G. Popovic, K. Diesner, A. Chemseddine, A. Eychmüller, and H. Weller. CdS nanoclusters: Synthesis, characterization, size dependent oscillator strength, temperature shift of the excitonic transition energy, and reversible absorbance shift. *Journal of Physical Chemistry*, 98(31):7665–7673, 1994.

[112] Tijana Rajh, Olga I. Mićić, and Arthur J. Nozik. Synthesis and characterization of surface-modified colloidal CdTe quantum dots. *Journal of Physical Chemistry*, 97(46):11999–12003, 1993.

[113] Jacek Jasieniak, Lisa Smith, Joel Van Embden, Paul Mulvaney, and Marco Califano. Re-examination of the size-dependent absorption properties of CdSe quantum dots. *Journal of Physical Chemistry C*, 113(45):19468–19474, 2009.

[114] István Robel, Masaru Kuno, and Prashant V. Kamat. Size-dependent electron injection from excited CdSe quantum dots into TiO2 nanoparticles. *Journal of the American Chemical Society*, 129(14):4136–4137, 2007.

[115] Martin A. Green. Multiple band and impurity photovoltaic solar cells: General theory and comparison to tandem cells. *Progress in Photovoltaics: Research and Applications*, 9(2):137–144, 2001.

[116] Y. Okada, N. J. Ekins-Daukes, T. Kita, R. Tamaki, M. Yoshida, A. Pusch, O. Hess, C. C. Phillips, D. J. Farrell, K. Yoshida, N. Ahsan, Y. Shoji, T. Sogabe, and J. F. Guillemoles. Intermediate band solar cells: Recent progress and future directions. *Applied Physics Reviews*, 2(2):021302, 2015.

[117] Neil S. Beattie, Patrick See, Guillaume Zoppi, Palat M. Ushasree, Martial Duchamp, Ian Farrer, David A. Ritchie, and Stanko Tomić. Quantum Engineering of InAs/GaAs Quantum Dot Based Intermediate Band Solar Cells. *ACS Photonics*, 4(11):2745–2750, 2017.

[118] Cherie R. Kagan and Christopher B. Murray. Charge transport in strongly coupled quantum dot solids. *Nature Nanotechnology*, 10(12):1013–1026, 2015.

[119] Olga I. Mićić, S. P. Ahrenkiel, and Arthur J. Nozik. Synthesis of extremely small InP quantum dots and electronic coupling in their disordered solid films. *Applied Physics Letters*, 78(25):4022–4024, 2001.

[120] Peter Liljeroth, Karin Overgaag, Ana Urbieta, Bruno Grandider, Stephen G. Hickey, and Daniël Vanmaekelbergh. Variable orbital coupling in a two-dimensional quantum-dot solid probed on a local scale. *Physical Review Letters*, 97(96803):1–4, 2006.

[121] Dov Steiner, Assaf Aharoni, Uri Banin, and Oded Millo. Level structure of InAs quantum dots in two-dimensional assemblies. *Nano Letters*, 6(10):2201–2205, 2006.

[122] M. V. Artemyev, A. I. Bibik, L. I. Gurinovich, S. V. Gaponenko, and U. Woggon. Evolution from individual to collective electron states in a dense quantum dot ensemble. *Physical Review B - Condensed Matter and Materials Physics*, 60(3):1504–1506, 1999.

[123] Stanko Tomić. Theory of Quantum Dot Arrays for Solar Cell Devices. *Springer*, pages 113–134, 2014.